

Instytut Fizyki Plazmy i Laserowej Mikrosyntezy
w Warszawie



Thesis is submitted for
the degree of Doctor of Philosophy in Physics

NUMERICAL STUDIES OF IMPURITY TRANSPORT IN JET ILW DISCHARGES

mgr inż. Irena Ivanova-Stanik

Supervisor: Prof. dr hab. Roman Zagórski
Supporting supervisor: Dr Agata Chomiczewska

Warsaw 2020

*Składam serdeczne podziękowania mojemu promotorowi
Prof. dr hab. Romanowi Zagórskiemu
za dzielenie się swoją wiedzą i nieustanną motywację,
bez której ta praca nigdy by nie powstała.
Dziękuję Agatce Chomiczewskiej za opiekę, dyskusje i porady.
Serdeczne podziękowania dla Włodka Stępniewskiego
za wszystkie pogaduszki przy kawie, za całą masę artykułów wysyłanych do mnie.
Szczególne podziękowania pragnę złożyć mojej rodzinie za ich wsparcie.*

LIST OF THE BACKGROUND PUBLICATIONS RELATED TO THE THESIS

The thesis is mainly based on the following publications (listed in chronological order):

1. G. Telesca, R. Zagórski, S. Brezinsek, M. Brix, J. Flanagan, I. Ivanova-Stanik et al., JET EFDA contributors, Simulation with the COREDIV code of JET discharges with the ITER-like wall, *Journal of Nuclear Materials* 438 (2013) S567-S571
2. D. Kalupin, I. Ivanova-Stanik, I. Voitsekhovitch et al., Numerical analysis of JET discharges with the European Transport Simulator, *Nucl. Fusion* 53 (2013) 123007 (8pp)
3. G.L. Falchetto, D. Coster, R. Coelho, B.D. Scott, L. Figini, D. Kalupin, E. Nardon, S. Nowak, L.L. Alves, J.F. Artaud, V. Basiuk, Joao P.S. Bizarro, C. Boulbe, A. Dinklage, D. Farina, B. Faugeras, J. Ferreira, A. Figueiredo, Ph. Huynh, F. Imbeaux, I. Ivanova-Stanik et al., The European Integrated Tokamak Modelling (ITM) effort: achievements and first physics results, *Nucl. Fusion* 54 (2014) 043018 (19pp)
4. I. Ivanova-Stanik, R. Zagórski, G. Telesca, A. Czarnecka, C. Challis, J. Hobirk, Integrated Modelling of Nitrogen Seeded JET ILW Discharges for H-mode and Hybrid Scenarios, *Contrib. Plasma Phys.* 54 (2014) No. 4-6, 442-447
5. G. Telesca, I. Ivanova-Stanik, R. Zagórski, S. Brezinsek, C. Giroud, G. Van Oost, Numerical Scaling with the COREDIV Code of JET Discharges with the ITER-Like Wall, *Contrib. Plasma Phys.* 54 (2014) No. 4-6, 347-352
6. R. Zagórski, I. Ivanova-Stanik, A. Czarnecka, G. Telesca, S. Brezinsek, Influence of seeding and SOL transport on plasma parameters in JET ITER-like wall H-mode discharges, *Journal of Nuclear Materials* 463 (2015) 649-653
7. G. Telesca, I. Ivanova-Stanik, R. Zagórski and et al., Numerical simulations of JET discharges with the ITER-like wall for different nitrogen seeding scenarios, *Journal of Nuclear Materials* 463 (2015) 577-581
8. I. Ivanova-Stanik, L. Aho-Mantila, M. Wischmeier, R. Zagórski, COREDIV and SOLPS numerical simulations of the nitrogen seeded JET ILWL-mode discharges, *Contrib. Plasma Phys.* 56 No.6-8 (2016) 760-765
9. I. Ivanova-Stanik, R. Zagórski, Corediv modeling of JET ILW discharges with different impurity seeding: nitrogen, neon, argon and krypton, *Nukleonika* 62(1) (2017) 3-7
10. G. Telesca, I. Ivanova-Stanik, R. Zagórski et al., High power neon seeded JET discharges: Experiments and simulations, *Nuclear Materials and Energy* 12 (2017) 882-886

11. G. Telesca, I. Ivanova-Stanik, S. Brezinsek et al., Simulation of JET ITER-Like Wall pulses at high neon seeding rate, *Nuclear Fusion* 57 (2017)126021
12. R. Zagórski, A. Czarnecka, I. Ivanova-Stanik, C. Challis, Modelling of JET DT experiments in ILW configurations, *Contrib. Plasma Phys.*58 (2018) 739-745
13. N. Krawczyk, A. Czarnecka, I. Ivanova-Stanik et al., Application of the VUV and the soft X-ray systems on JET for the study of intrinsic impurity behavior during neon seeded ILW hybrid discharges, *Review of Scientific Instruments* 89(10)(2018) 10D131
14. G. Telesca, I. Ivanova-Stanik, R. Zagórski et al., COREDIV numerical simulation of high neutron rate JET-ILW DD pulses in view of extension to JET-ILW DT experiments, *Nucl. Fusion* 59 (2019) 056026 (10pp)

The author of the thesis is the principal author of all above listed publications and has actively participated in the work reported in them.

Streszczenie

Rozwiązanie problemu transportu plazmy i zanieczyszczeń jest jednym z kilku kluczowych zagadnień warunkujących sukces kontrolowanej fuzji jądrowej. Związany jest on z koniecznością kontroli uwalnianych w trakcie wyładowania ze ścian i dywertora tokamaka jonów i atomów tzw. domieszek wewnętrznych oraz celowo wprowadzanych do plazmy gazów (azot, neon, argon, krypton), których zadaniem jest ograniczenie strumieni energii do ściany tokamaka. Domieszki mają ogromny wpływ na przebieg wyładowania i na parametry plazmy w tokamaku.

Przedmiotem tej pracy doktorskiej jest analiza transportu plazmy i zanieczyszczeń w tokamaku JET ILW (Culham, Wlk. Brytania), tzn. aktualnej konfiguracji tokamaka JET ze ścianą berylową i wolframowym dywertorem, odpowiadającej przewidywanym warunkom pracy w reaktorze ITER. Zrozumienie transportu domieszek w tokamaku JET ILW i w przyszłych reaktorach termojądrowych ITER, DEMO jest jednym z najważniejszych problemów wymagających znaczącego wysiłku badawczego. Uzyskanie wiarygodnego narzędzia symulacyjnego, które pozwala na przewidywanie i interpretację parametrów wyładowań jest jednym z głównych celów prac prowadzonych w ramach Konsorcjum Eurofusion w ciągu ostatnich lat.

W pracy przedstawiono procesy fizyczne prowadzące do generacji zanieczyszczeń w tokamakach, jak również mechanizmy fizyczne odpowiedzialne za transport jonów domieszek w sznurze plazmowym. Ponieważ wyżej wymienione procesy jak też związki między nimi są silnie nieliniowe, jedynym ze sposobów uzyskania informacji na temat ich wpływu na transport domieszek w tokamaku jest modelowanie komputerowe. Głównym celem pracy była analiza transportu zanieczyszczeń plazmy, wpływu jonów domieszek na główne parametry plazmy, takie jak czas utrzymania energii, temperatura plazmy, jej promieniotętność, czy też obciążenie termiczne płyt dywertora. Zarysowany powyżej kompleks problemów przedstawiony został na konkretnym przykładzie modelowania plazmy w tokamaku JET ILW za pomocą kodów COREDIV i ETS (European Transport Solver).

Do jednego z istotnych wyników prowadzonych badań opisanych w tej pracy należy zaliczyć zaimplementowanie metody opisującej transport domieszek z kodu COREDIV do kodu ETS. W osobnych rozdziałach, przedstawione zostały wyniki analiz wpływu na przebieg wyładowania takich czynników jak: intensywność domieszkowania, radialny transport cząstek w obszarze brzegowym, podstawowe parametry wyładowania (takie jak gęstość plazmy, moc grzania, prąd plazmy) oraz rodzaj napuszczanego gazu: N, Ne, Ar, Kr. Przedstawiono wyniki obliczeń przeprowadzone dla parametrów plazmy w różnych reżymach pracy tokamaka: z dobrym (H mode) i słabym utrzymaniem energii (L-mode) oraz dla tzw. wyładowań hybrydowych.

Porównanie wyników obliczeń z danymi eksperymentalnymi wykazało dużą zgodność pomiędzy teorią a eksperymentem. Stwierdzono między innymi, że w przypadku dywertora wolframowego istotne znaczenie ma pojawienie się mechanizmu samoregulującego produkcję wolframu, który jest głównym źródłem promieniowania w obszarze centralnym plazmy w tokamaku. W pracy sformułowano wnioski, które są istotne dla opty-

malizacji wyładowań w tokamaku JET ILW oraz dla pracy urządzeń wyposażonych w dywertory wykonane z wolframu takie jak reaktorze ITER.

Abstract

Solving the problem of plasma and impurity transport is one of the key issues for the success of controlled nuclear fusion. It is connected with the necessity of control of ions and atoms released during the discharge from the walls and the tokamak divertor, the so-called intrinsic impurities and gases deliberately introduced into the plasma (nitrogen, neon, argon, krypton) (external impurities), whose task is to limit the energy fluxes to the tokamak wall. Impurities have a huge impact on the discharge evolution and plasma parameters in the tokamak.

The subject of this dissertation is the analysis of the transport of plasma and impurities in the JET ILW tokamak (Culham, UK), i. e. the current configuration of the JET tokamak with a beryllium wall and tungsten divertor corresponding to the expected operating conditions in the ITER reactor. Understanding the transport of impurity in the JET ILW tokamak and in the future fusion reactors: ITER, DEMO, is one of the most important issues requiring a significant research effort. Obtaining a reliable simulation tool to predict and interpret discharge parameters is one of the main objectives of the work carried out by the Eurofusion Consortium in recent years.

The paper presents physical processes leading to generation of impurities in tokamaks, as well as physical mechanisms responsible for transport of impurity ions in plasma column. Since the above mentioned processes as well as the relations between them are strongly non-linear, one of the ways of obtaining information on their influence on the impurity transport in the tokamak is computer modelling. The main objective of the study was to analyze the transport of plasma impurities, the influence of impurity ions on the main plasma parameters, such as energy confinement time, plasma temperature, plasma radiation and thermal load of the divertor plates. The complexity of problems outlined above is presented on a specific example of plasma modeling in the JET ILW tokamak using COREDIV and ETS (European Transport Solver) codes.

One of the important results of the research described in this thesis is the implementation in the ETS code of the numerical algorithm taken from the the COREDIV code, which solves the impurity transport equations.

In separate chapters, the results of analyses of the impact of different factors such as impurity level, radial transport of particles in the scrape of layer (SOL), basic discharge parameters (such as plasma density, heating power, plasma current) and the different impurity seeding gases (N, Ne, Ar, Kr) are discussed. The results of calculations carried out for plasma parameters in various working conditions of the tokamak: with good (H -mode) and low energy confinement (L-mode) as well as for the so-called hybrid discharges are presented.

The comparison of the calculation results with the experimental data showed a high correlation between numerical simulations and the experiment. It was found, inter alia, that in the case of tungsten divertor the emergence of a self-regulatory mechanism for tungsten production, which is the main source of radiation in the core plasma of the tokamak, is essential. This thesis presents conclusions that are important for the optimization of discharges in the JET ILW tokamak and for the operation of devices

equipped with tungsten divertor such as the ITER reactor.

Contents

1	Introduction	7
1.1	Nuclear fusion	7
1.2	Tokamak devices	9
1.2.1	Limiter and divertor	10
1.2.2	Ohmic, Low confinement (L-mode), High confinement (H-mode) Mode	11
1.2.3	Power exhaust	13
1.2.4	Time confinement - scaling low	13
1.3	The Joint European Torus (JET)	14
1.4	Motivation and outline of the work	16
2	Impurities in tokamak	19
2.1	Sources of intrinsic impurities in the tokamak	19
2.1.1	Physical sputtering	20
2.1.2	Chemical sputtering	22
2.1.3	ELMs and disruptions	24
2.1.4	Prompt redeposition	25
2.1.5	Impurity seeding	27
2.2	Atomic processes in the plasma	27
2.3	Radiative processes in the plasma	30
3	Basic of plasma transport	32
3.1	Kinetic and fluid description of plasma in tokamak	32
3.1.1	Equations for the core in COREDIV code	34
3.1.2	Equations for the scrape-off layer plasma in COREDIV code	35
3.2	Transport process	38
3.2.1	Classical impurity transport	39
3.2.2	Neoclassical impurity transport	40
3.2.3	Anomalous transport	41
3.2.4	Transport in COREDIV code	43
4	Diagnosctics in JET ILW	45
5	Numerical codes used in JET ILW simulation	51
5.1	Edge/SOL codes group	51
5.2	Core codes	53

5.3	Integrated codes	56
6	Numerical studies of impurity transport in JET ILW discharges without impurity seeding	61
6.1	Simulation for L-mode discharges	61
6.2	Simulations for H-mode discharges	65
6.3	Summary	65
7	Analysis of the influence of the source of the external (seeded) impurity	67
7.1	Influence of the nitrogen impurity puff	67
7.2	Influence of the neon seeding	72
7.3	Influence of the sputtering coefficient	74
7.4	Comparison of the different impurity seedings in JET ILW	77
7.5	Summary	82
8	Analysis of the influence of the auxiliary heating on the impurity transport in JET ILW	84
8.1	Influence of the different auxiliary heating schemas: analysis with ETS code	84
8.2	Influence of the auxiliary heating power level	88
8.2.1	Influence of auxiliary power on the impurity in ramp-down phase	89
8.2.2	Influence of auxiliary power level on the impurity seeding in H-mode discharges	94
8.2.3	Influence of auxiliary power level for DT plasma	96
8.3	Summary	98
9	Influence of the electron separatrix density on the impurity	99
9.1	Influence of the electron separatrix density on the ramp-down phase . .	100
9.2	Influence of the electron separatrix density on the impurity in steady state plasmas	103
9.3	Summary	103
10	Influence of the impurity radial transport in SOL	104
10.1	Summary	108
11	Modelling of JET DT experiments in ILW configurations	110
11.1	Summary and discussion	113
12	Summary and Outlook	115

Chapter 1

Introduction

1.1 Nuclear fusion

Nuclear fusion is a nuclear reaction in which two or more atomic nuclei come close enough to form one or more different atomic nuclei and subatomic particles (neutrons and/or protons). The difference in mass between the products and reactants is manifested as the release of large amounts of energy. For fusion to occur the light nuclei need to overcome the repellent Coulomb force of the positively charged protons inside the nuclei.

Studies of the nuclear properties of light element fusion indicate that three such reactions:

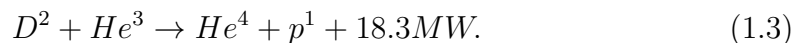
1. the fusion reaction Deuterium-Tritium (D-T) reaction, which is considered to be the most viable for the production of useful power



2. reaction DD, which actually has two branches, each occurring with an approximately equal likelihood.



3. D reaction with He



may be advantageous for the production of nuclear energy.

The Fig. 1.1 shows the reaction rate, which is defined as a convolution of the velocity-weighted cross-section with a Maxwellian distribution for the D-T reaction in comparison to other high energy fusion reactions, D-D and D-He.

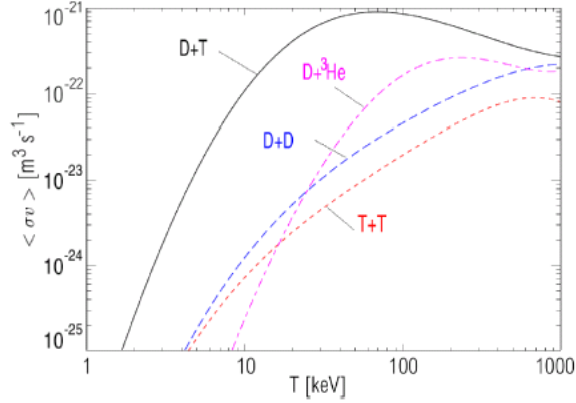


Figure 1.1: Reaction rates of potential fusion reactions for reactors [1].

The reason the D-T reaction is considered to provide the most viable route to a fusion power is that this reaction has:

- the highest and most accessible cross section
- releasing the most energy per reaction.

Unfortunately, there are several serious disadvantages to this reaction:

- tritium is both radioactive and expensive
- the neutrons released can harm living things and damage any other materials surrounding them.
- the neutrons can activated some materials making them radioactive.

For net energy production the power released by fusion reactions, P_{fus} , has to be larger than the applied external auxiliary power, P_{aux} , to generate these reactions such that $Q = P_{fus}/P_{aux} > 1$, where Q is called as fusion energy gain factor. The condition of $Q = 1$ is referred to as breakeven. To obtain an overall positive energetic balance it is necessary to heat the ionized gases, called plasma, up to fusion temperature keeping them confined in a limited space for a time sufficient to obtain more energy power than the one necessary to compensate for the losses and the energy necessary to reach this condition. The Lawson criterion [2] is derived from power balance considerations for a pure DT plasma and defines plasma properties that are necessary to achieve a self-heated plasma with $Q > 1$ and can be written as:

$$nT\tau_E \geq 3 \times 10^{21} [m^{-3} keVs], \quad (1.4)$$

where n is the plasma density, T is the plasma temperature and τ_E is the energy confinement time, which is defined as the time over which all the energy stored in the plasma is lost through loss mechanisms. Example for the range of τ_E , for a plasma with a temperature of 10 keV and density of $10^{20} m^{-3}$ it would be necessary to produce a plasma with a confinement time greater than 3 seconds to reach ignition.

The presence of impurities in hydrogenic plasma, either intrinsic or deliberately puffed for radiative purposes, lowers fusion output through both: by impurity radiation

and by through dilution of hydrogenic species. This necessitates a modification of the Lawson criterion. An example of a modified Lawson criterion for the case $T = T_e = T_i$ (the same temperature for electrons and ions) is given in Ref. [3]:

$$n\tau_E \geq \frac{\frac{3}{2}f_{tot}T}{\frac{1}{4}\langle\sigma_{DTv}\rangle \cdot f_H^2 \cdot E_\alpha - L_Z(T)}, \quad (1.5)$$

where $f_{tot} = \frac{\sum_i n_i}{n_e} \leq 1$ is the ion-electron density fraction (dilution), n_e is the electron density, $\langle\sigma_{DTv}\rangle$ is the fusion reaction rate of the D-T reaction, $f_H = n_H/n_e$ is fractional abundance of the hydrogenic species, E_α is the kinetic energy of the alpha particles and L_Z the loss function due to line and recombination radiation of impurities. Without radiation losses $L_Z = 0$ and dilution ($f_{tot} = f_H = 1$) the formula is the standard Lawson criterion. Determination of the tolerable impurity concentrations in a fusion reactor is for different impurities reported in Ref. [4]. It is essential to have low impurity concentrations in the plasma to fulfil the condition of a steady burning fusion plasma.

The major approaches to achieving the necessary plasma conditions for fusion power are:

- Magnetic Confinement Fusion (MCF),
- Inertial Confinement Fusion (ICF).

Both concepts plan to use a hot plasma to fuse the nuclei of D and T. In inertial confinement fusion, small DT ice pellets are isotropically and homogeneously heated by laser or ion beams [5]. The compression and a fast ignition laser pulse provides confinement and heating at the same time and initiate the fusion reactions.

In magnetic confinement fusion, charged particles are confined by magnetic fields using the Lorentz force to restrict their motion perpendicular to field lines. The particles travel on helical trajectories along magnetic field lines, the so called gyro-motion [6]. A large number of different magnetic confinement geometries have been explored, including Z-pinchs [7], Mirror Machines, Reverse-Field Pinches, Spheromaks [8], Stellarators and Tokamaks [9]. There are two competing approaches of how to generate the poloidal magnetic field. In a tokamak it is produced by a toroidal plasma current. In stellarators the poloidal field relies on a more complicated set of sophisticated, external field coils only, e.g. helical coils or optimized modular field coils. In that work, focus is given to the tokamak only, because this thesis is concerned on analysing the discharges in the JET tokamak ILW (ITER Like Wall) configuration.

1.2 Tokamak devices

The tokamak has been so far the most successful machine to realize thermonuclear fusion power plants as a source of energy. It has been developed in the early 1960s in the Soviet Union and the name "tokamak" is the acronym of the Russian words "TOroidallnaya KAMERA s MAGnitnymi KATUSHkami" which means toroidal chamber with poloidal coils. The Fig. 1.2, shows the basic structure of a tokamak. In the

tokamak, the poloidal field is produced by a toroidal plasma current I_p , which is induced by a transformer, where the primary winding is formed by a central solenoid and the plasma is the secondary winding. The toroidal magnetic field is created by the toroidal field coils. The poloidal field at the plasma edge is of the order of 0.1T and the toroidal field has a few T. A tokamak is characterized by two geometric quantities: the major radius, R , is the distance from the toroidal axis of symmetry and minor radius, a , is the distance from the geometric/magnetic axis in the poloidal plane. The aspect ratio is an important machine parameter that is defined as $\varepsilon = R/a$ (ratio of the two radii).

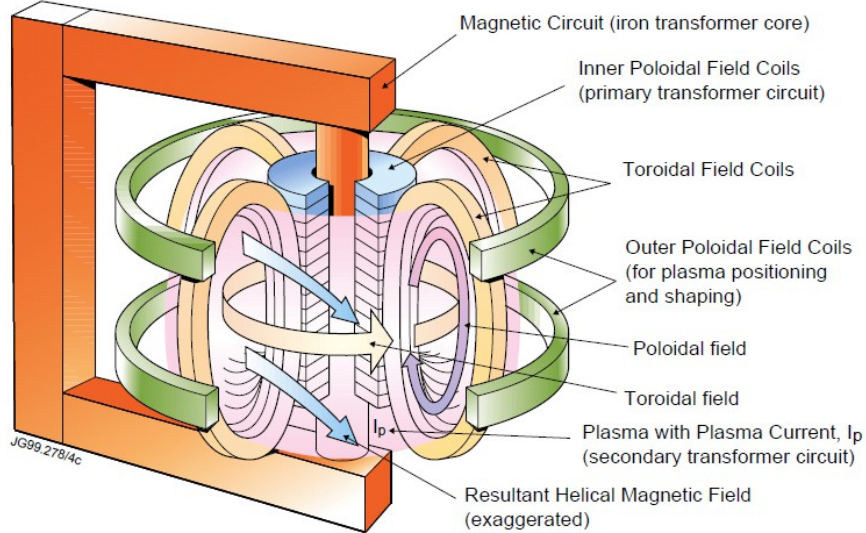


Figure 1.2: Basic structure of a tokamak [10].

The shape and position of the magnetic surfaces is controlled by additional external poloidal coils. The configuration of the composite magnetic field lines is described by safety factor q . The safety factor q indicates how many toroidal trips around the torus are required for a magnetic field line to return to the initial location on the poloidal cross section. The safety factor for a large aspect-ratio ($\varepsilon \gg 1$) tokamak of circular cross-section is calculated with r the distance from the magnetic axis (R), as [2]:

$$q(r) = \frac{r B_T}{R B_\Theta} \quad (1.6)$$

where B_T is the toroidal and B_Θ is the poloidal magnetic field.

1.2.1 Limiter and divertor

In a tokamak two major magnetic field geometries can be distinguished: limiter and the divertor configuration. In limiter geometry the LCFS (Last Closed Flux Surface) is determined by the tangential intersection of a particular magnetic flux surface with a material surface, which is called limiter. The limiter is in direct contact with the confined, hot plasma. The two configurations are illustrated in Fig. 1.3. The last closed flux surface (LCFS) is given by the magnetic separatrix in the divertor configuration. The plasma region outside the LCFS is termed the scrape of layer (SOL) and is called the region of 'open' field lines, i.e. field lines which intersect with some part of the

vessel wall. The separatrix in the divertor configuration has the shape of an X in the lower part and the poloidal field is zero at the so called X-point. In the divertor configuration, the plasma wall interaction mainly takes place in a specially designed part of the plasma vessel, which is somewhat removed from the confined plasma and is termed the divertor. The separatrix legs in the divertor connect to the divertor target surface at the strike points. These target materials must have high heat load capacity. Present day designs of a fusion reactor (JET ILW, ITER) are based on the divertor concept.

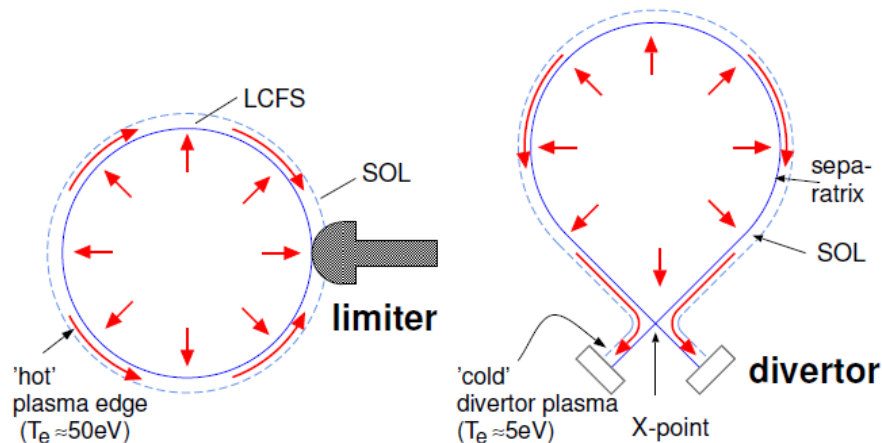


Figure 1.3: Limiter and divertor configuration shown in the poloidal cross-section of a tokamak with indicated flow pattern [3].

The midplane is the horizontal plane in the poloidal cross section, that is at the height of either the geometric or the magnetic axis.

1.2.2 Ohmic, Low confinement (L-mode), High confinement (H-mode) Mode

A magnetically confined plasma in a tokamak exists in different modes, which result in different levels of confinement. Known as confinement modes, these regimes often offer unique confinement properties and scalings. The first operational mode utilised in early tokamaks was one that provided plasma heating purely via ohmic heating with no auxiliary heating systems. As such, it became known as the *Ohmic confinement mode*. The Ohmic mode was therefore quickly ruled out as a viable route to a fusion power plant. It was determined that additional heating systems would be required to help raise the plasma temperature to reactor conditions. Plasmas with a low level of confinement are called L modes. The first high confinement mode, H-mode, was discovered at ASDEX tokamak [11]. A typical pressure profile for the L and H mode plasma is shown (in comparison to more advanced confinement modes) in Fig. 1.4.

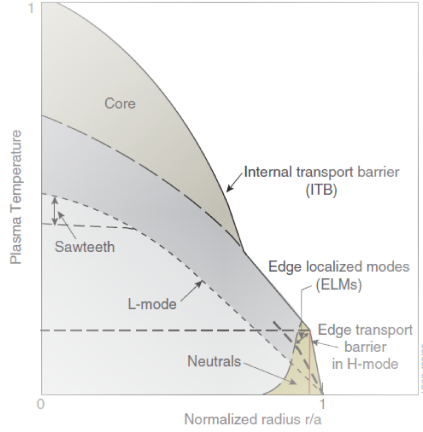


Figure 1.4: L- and H- mode pressure profile [12].

Global confinement times measured in the H-mode are in the order of 2-3 times the values obtained in the L-mode [13]. Steep gradients in the density and temperature profiles of the plasma are observed (see Fig. 1.4). This *jump* in the profile is commonly referred to as the H-mode pedestal. The low transport region at the edge of the H-mode plasma is known as an Edge Transport Barrier (ETB). A sudden transition from the operation in L-mode to H-mode occurs above a threshold for the heating power. Although known to depend on many parameters, it is widely accepted that the L-H transition threshold power strongly depends on the plasma density, toroidal magnetic field and plasma size. A power law scaling, including the line average plasma density, the magnetic toroidal field and the plasma surface area, is then used for fitting the experimental threshold power and leads to the following expression, given by Martin [14]:

$$P_{L-H} = 0.0488e^{\pm 0.057} n_e^{0.717 \pm 0.035} B_T^{0.803 \pm 0.032} S_0^{0.941 \pm 0.019}, \quad (1.7)$$

where P_{L-H} is the threshold power expressed in MW, n_e is the line average electron density in 10^{20}m^{-3} , B_T is the magnetic field in T and S_0 is the plasma surface area in m^2 . This expression is called *Martin Law*. The above scaling expressions are obtained from the data of deuterium discharges and of deuterium plasmas heated by hydrogen beam. The latter plasmas are considered to consist mainly of deuterium at the L-H transition. The dependence of the threshold power on the ion mass number M was roughly given by $P_{L-H} \propto 1/M$ [15]. When this mass dependence is applied to the deuterium-tritium discharges for *International Thermonuclear Experimental Reactor* (ITER) or DEMO, the above predicted values of P_{L-H} can be reduced by $\sim 20\%$.

A further distinguishing characteristic of the H-mode is the presence of events known as Edge Localised Modes (ELMs) [16], [17]. ELMs are a rapid (milliseconds) relaxations of the H-mode pedestal that are triggered at regular periods by an MHD instability. During an ELM event the local particle confinement at the plasma edge is reduced which causes an increased outflow of particles from the edge of the plasma. For this reason the global energy and global particle confinement times are observed to be lower during an ELMs period. H-mode is the foreseen confinement scheme for future fusion devices like the international tokamak ITER [18]. The extrapolation of the ELM induced heat loads to larger devices such as ITER, which are foreseen to be operated in type-I ELMy H-Mode plasmas, is a crucial activity since it defines the

operational range of future devices. The usually cited material limit for ELM peak divertor thermal impact is quoted to be 0.5 MJ/m^2 is found by material testing for a typical energy deposition time of $750 \mu\text{s}$ [19].

1.2.3 Power exhaust

In many fusion energy roadmaps, such a step, often called DEMO, is a machine, that should bridge the gap between ITER and the first commercial fusion power plant. In future fusion devices like ITER [18] and the demonstration reactor DEMO [20] power exhaust will be a challenge. Economic and technical considerations lead to a power plant size with a fusion power of 3 GW. The fusion power is distributed inversely proportional to the mass ratio of the fusion products: 80% in neutrons and 20% in alpha particles. The neutrons are not confined by the magnetic field and their energy is distributed over the whole first wall. The alpha particles are confined and transfer their energy to the plasma via collisions leading to the so-called alpha particle heating.

In the case of a DEMO-like reactor more than 85% of the heating power has to be radiated to meet the material limits. The reduction of divertor target power loads to an acceptable level is a critical issue for future fusion reactors. The radiative exhaust of energy by sputtered and by externally seeded impurities is considered, as a possible way of spreading energy over a large wall area. Plasma radiation can be increased by seeding extrinsic impurities and experiments with high radiative scenarios have been performed with different types of the seeding gases: nitrogen (N), neon (Ne), argon (Ar) and krypton (Kr) at the ASDEX Upgrade tokamak (AUG) [21], [22], and N and Ne at JET ILW [23].

1.2.4 Time confinement - scaling low

Energy confinement is a key issue in fusion research. Since it describes how well the energy remains in the extremely high temperature plasmas, that are required to reach fusion. The parameter used to characterise the confinement is the energy confinement time, defined as the ratio between the plasma energy and the heating power required to maintain it stationary (see Eq. 1.8).

$$\tau_{E,th} = \frac{\int \frac{3}{2}n(T_e + T_i)dx^3}{P_{aux}} \quad (1.8)$$

Inter-machine analyses show, that the energy confinement strongly increases with the plasma size and with the plasma current and to a less extent with the plasma density and the toroidal magnetic field. Conversely, it strongly decreases with the injected power.

One major aim in fusion research is to quantitatively understand the physics of particle and energy transport in confined plasma. This goal, which would allow to predict the thermal insulation and fusion performance of a device, has not yet been reached. Therefore it is necessary to derive empiric scaling for thermal insulation, based on the results achieved in existing devices. Thus, empirical multi-machine scalings have been developed in order to describe quantitatively the variation of τ_E with the change

of plasma parameters across a wide range of plasma conditions. Scaling laws are best-fits of data from thousands of experiments across many tokamaks, used to estimate performance of tokamaks with various operating parameters. In 2001, after analysis of the enlarged ITERH.DB3v10 (*final*) dataset with ELMy H mode contributions from 14 tokamaks, the practical reliability of the ITERH-98P(y,2) scaling was confirmed by International Workshop of the confinement database and modelling expert group in collaboration with edge and pedestal physics expert group. The scaling law used in the design of ITER(ITERH-98(y,2)) predicts that the most significant factor in improving the performance of a tokamak is the major radius of the plasma. The Fig. 1.5 shows the observed $\tau_{E,th}^{exp}$ for the extended dataset against the prediction by ITERH-98P(y,2) [24].

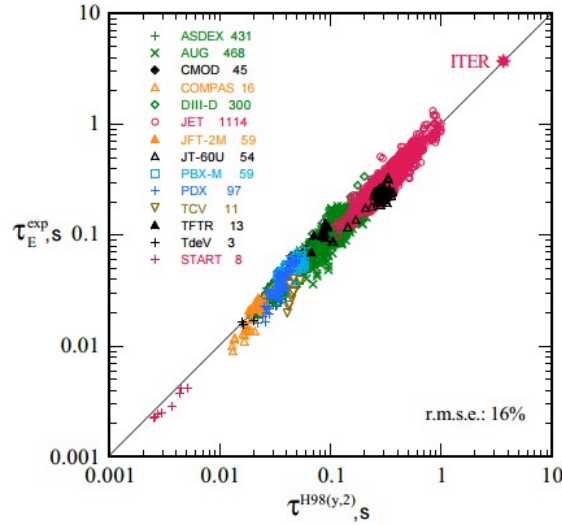


Figure 1.5: Thermal energy confinement: observed vs. predicted [24].

The ITER-98y2 ELM-y H-mode scaling is given by formula:

$$\tau_E^{H98(y,2)} = 0.05621 \times I_p^{0.93} \times B^{0.15} \times n_e^{line 0.41} \times P_{core}^{-0.69} \times R_T^{1.97} \times \left(\frac{a}{R_T}\right)^{0.58} \times \bar{A}_i^{0.19} \times \kappa^{0.78} \quad (1.9)$$

where I_p is the total plasma current in MA, B_T is the toroidal magnetic field in T, n_e^{line} is the line average electron line density given in 10^{19}m^{-3} , P_{core} is power in core plasma in MW, R_T is the toroidal radius in m, \bar{A}_i is the mean ion mass number and κ is the elongation of the plasma cross-section.

1.3 The Joint European Torus (JET)

The Joint European Torus, known simply as JET is located near the village of Culham in the United Kingdom and has been operating since 1983. Originally designed and built as limiter tokamak, JET was subsequently converted to a divertor tokamak in 1992. The JET toroidal vacuum vessel has a major radius of 2.96m. It is the only tokamak presently capable of operating with tritium, though to prevent the radioactivation of the vessel the majority of experiments are run using pure deuterium plasmas. For an example, JET has the world record of the highest fusion power 16.1MW of

fusion power, equivalent to $Q = 0.62$, was generated by D-T experiments in JET in 1997 [25]. It is currently operated by behalf of EUROfusion Consortium.

The carbon wall has not caused serious problems for the experiments using deuterium (or hydrogen) gas only, but nuclear safety regulations prohibit its use in a reactor due to the large retention of tritium within carbon [26]. In ITER, the use of a carbon first wall would lead the in-vessel inventory of tritium to exceed the maximum allowable, limited by regulations on the allowable radioactive material inventory. This requires ITER to be designed using non carbon material for the first wall. Beryllium has been selected in ITER due to the low retention of hydrogen isotope and low radiation level of Be in the plasma [27]. It is selected first, because has the advantages of being a low-Z material with a good thermal conductivity. Second, the ability to getter oxygen from the plasma, which is in particular important for the start-up phase. However, its high sputtering yields and the low melting point limit its power handling capabilities. Low erosion, i.e. low effective sputtering yields, high sputtering threshold and no chemical erosion, are required for divertor. Tungsten has been selected due to the high melting temperature and low sputtering yield. The tritium retention in tungsten is small and compatible with the design of future fusion reactors [28]. However, in contrast to carbon, tungsten melts, when its material limits are exceeded. JET underwent a transformation from a full carbon-dominated tokamak to a fully metallic device with beryllium in the main chamber and a tungsten divertor. This material combination is foreseen for the activated phase of ITER, for this reason JET with Be wall and W divertor is called JET ILW (ITER Like Wall). The ITER Like Wall installation was successfully completed in 2011. The ITER Like Wall experiment at JET shall demonstrate the plasma compatibility with metallic walls and the reduction in fuel retention. Fig. 1.6 shows the picture of the completed JET ILW configuration.

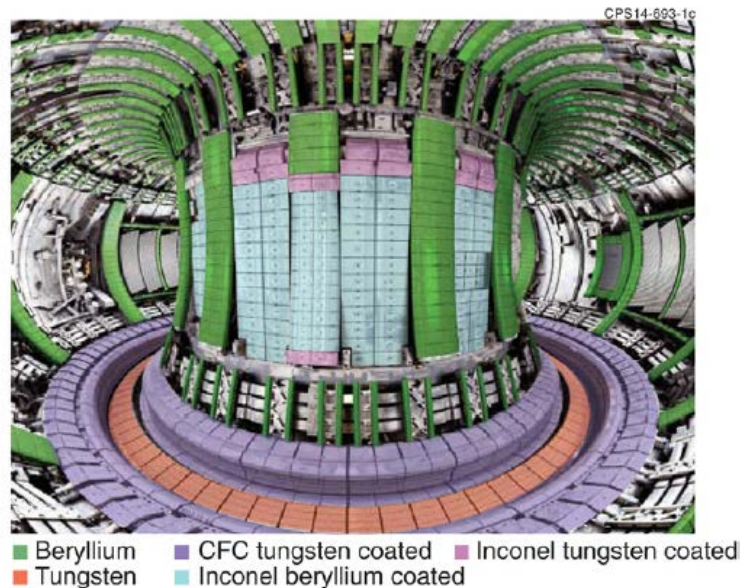


Figure 1.6: JET ILW [29].

A large number of diagnostics are available to assess the state of the plasma. These include Thomson scattering systems, far-infrared interferometers, neutron cameras,

bolometers and various spectroscopic systems. Among the variables measured are the electron and ion temperatures and densities, impurity levels in the plasma, plasma rotation rates and the neutron flux. JET experiments with the ILW have produced invaluable information on the wall material's behaviour and a technical basis for the scenario development in ITER.

1.4 Motivation and outline of the work

Experimental areas where significant progress has taken place in last years are energy transport, in particular of the anomalous transport scaling, particle transport in the core and SOL. Particle transport plays a major role in the interaction of diverted plasmas with the main-chamber material elements. This experimental progress has been accompanied by the development of modelling tools for the physical processes in the plasma and plasma-materials interaction and the further validation of these models by comparing their predictions with the new experimental results. Progress in the modelling development and validation has been mostly concentrated to predictions for ITER with plasma modelling codes, including models for the transport of impurities at the plasma to describe the core contamination by impurities and the migration of eroded materials at the edge plasma. The acceptable erosion rates are determined by the required life time of the plasma facing components, as well as by the low limits for the allowed central impurity concentrations, which are very low for the high-Z elements and in the percent range for beryllium and carbon. Here, impurity transport between the wall components and the plasma centre is the key element, which has to be considered.

For a burning plasma device like ITER and DEMO, main chamber radiation and divertor radiation by impurity seeding will be mandatory to reduce power loads in the divertor region. The spatial distribution of the radiated power is crucial for working at plasma operation in H-mode. It has to be such, that the confinement is not degraded.

This knowledge is strongly needed to predict impurity transport in next step fusion devices, and will influence the material choice or indicate advantageous plasma operation scenarios with low central impurity concentrations. Transport investigations have to be performed for the whole range of elements from He up to W. Since the construction of large fusion plasma experiments is expensive and time consuming, it is not possible to test many elements as plasma wall components on a large scale.

The work presented in this thesis aims to understand the physics of the impurity transport, their production and their role in tokamaks. The relevant questions addressed in this thesis are:

- What is the effect of radiation by seeding impurity?
- What is the effect of high radiation and fuel dilution by impurities on the energy confinement?
- How does the plasma respond to different impurities?

- What is the effect by seeding impurity on the W sputtering?
- Is it possible to reproduce the experimental observations by modelling, predict and control detrimental events such as W production?

To answer these questions transport analysis have been carried out taking the spatial radiation distribution into account.

The thesis of this work is, **that physical models applied in COREDIV and ETS codes allow to obtain results in accordance with experimental results and explain a number of phenomena related to the transport of impurities in the JET ILW tokamak.**

In order to achieve the goal of the doctoral dissertation, which is to demonstrate the truthfulness of the above thesis, detailed research has been undertaken , which consisted in the following stages:

- participation in the JET ILW experiments and analysis of experimental results
- numerical studies of the influence of:
 - the impurity sources on discharge parameters
 - different seeding gases on plasma performance
 - the auxiliary heating on the impurity transport in JET ILW
 - the electron separatrix density on impurity transport
 - the impurity radial transport in the SOL on the divertor operation
- a summary of the results of the work and an evaluation of the achievement of the objective of the work, and thus confirmation of the validity of the thesis of work

In order to check the truthfulness of the thesis it was necessary to perform simulation with COREDIV code for different plasma scenarios in order to test the code ability to reproduce the experimental observations with implemented theoretical models and to gain a better understanding of the complex physical mechanisms that govern plasma dynamics and contribute to the reduction of the power loads to the target plates. It has been possible to qualitatively reproduce the experimental observations in the numerical modeling.

For the study of plasma and impurity transport in tokamaks many elements from quite different physics fields have to be combine. The necessary ingredients are presented in Fig. 1.7.

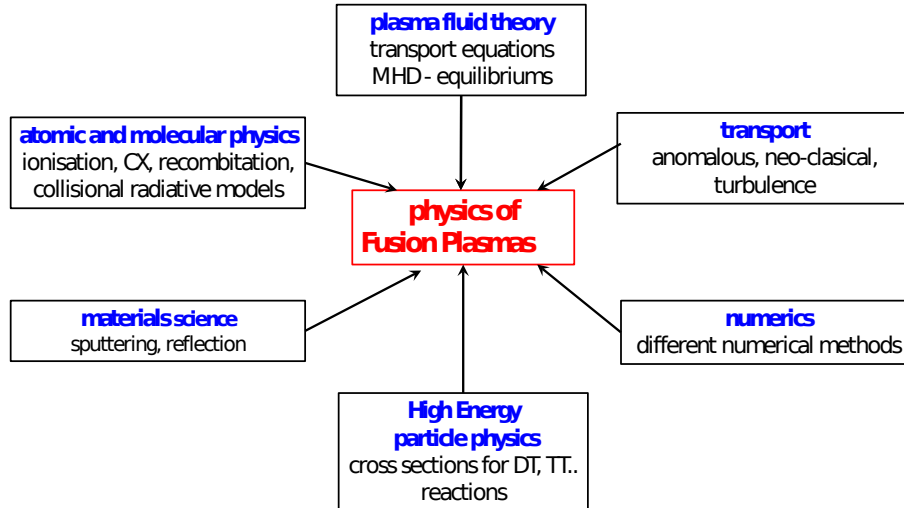


Figure 1.7: The ingredients in plasma physics.

The interaction of plasma with wall and divertor (material science) calls for the need for detailed understanding of processes creating neutrals (impurity) or ions at material surfaces. Atomic and molecular processes affects strongly the plasma through ionization and recombination. The basic physics of impurities, their production, main erosion processes and associated atomic physics are presented in Chapter 2. The plasma fluid theory is needed to obtain transport equations governing the plasma dynamics. The different transport processes in plasma are presented in Chapter 3. Chapter 5 describes the pros and cons of individual numerical codes and their application to calculations of physical problems in discharges for the JET ILW tokamak.

The results from simulations need verification by comparison with experimental results, for this reason short description of the diagnostic systems in JET tokamak is presented in Chapter 4. Numerical studies of impurity transport in JET ILW discharges are shown in Chapter 6. Analysis of the influence of the impurity sources, of the auxiliary heating on the impurity transport, of the impurity radial transport in SOL and comparison of the different impurity seedings are presented in Chapter 7, Chapter 8, Chapter 9 and Chapter 10, respectively. In Chapter 11 modelling of JET DT experiments in ILW configurations is presented. Finally, a discussion about the results and concluding remarks are given in Chapter 12.

Chapter 2

Impurities in tokamak

Impurities in tokamaks can be grouped into two different categories by their origin: intrinsic and extrinsic. The latter one are impurities injected to the plasma by gas puffing, for example impurity seeding uses nitrogen(N) and noble gasses: neon (Ne), argon (Ar) and krypton (Kr) or produced due to Laser Blow-Off (LBO). The impurities can be also divided in subcategories depending on their mass (atomic number(Z)): low- Z , mid- Z and high- Z . Low- Z impurities are those with $Z < 10$ and in case of JET ILW they are: beryllium (Be), nitrogen(N), oxygen (O). The mid- Z impurities in JET are nickel (Ni), iron (Fe) and copper (Cu). The high- Z impurities ($Z > 40$) are tungsten (W) and molybdenum (Mo).

The intrinsic category includes:

- impurities, that have migrated into the plasma following erosion of the plasma facing components (PFCs)
- impurities, source of helium from thermalised alpha particles (product of the D-T reaction) created in the plasma core.

2.1 Sources of intrinsic impurities in the tokamak

The intrinsic impurities in tokamak arise from plasma wall interaction. Impurity fluxes from wall elements entering the plasma can be generated by a combination of different erosion mechanisms. The main erosion processes in tokamak are physical and chemical sputtering, erosion by arcs, and blistering. In the present paper, focus is given to physical and chemical sputtering, which is the dominant mechanism in JET ILW discharges.

For the impurities, which are eroded from the plasma facing components, the production rate strongly depends on the choice of the material. Energetic plasma particles strike the solid surface, dislodging atoms from the lattice in a process called sputtering. In time, sputtering can result in substantial erosion of the surface. Light ions such as, carbon and oxygen get into discharges by low-energy detachment processes of molecules adsorbed on the machine walls; metallic atoms are released mostly due to sputtering.

Impurity generation by erosion of materials from plasma facing components is an important issue for a fusion device with respect to:

- the life time of wall components
- detrimental effects on the plasma performance due to fuel dilution and/or radiation losses in the plasma core.

2.1.1 Physical sputtering

When the energy of the impinging particles exceeds the threshold energy to displace surface atoms, the surface atoms are sputtered to leave the surface, which is referred to as physical sputtering. The threshold energy is larger for heavier surface atoms. Energetic plasma particles strike the solid surface, dislodging atoms from the lattice. Atoms (impurities), which have been injected into the plasma from the walls are ionized but eventually return to strike a solid surface, giving rise to self-sputtering. All sputtering processes are characterized by the sputtering yield, Y , which is the number of atoms or molecules ejected per impinging particle.

Physical sputtering results from elastic energy transfer from incident particles to target atoms. The minimum transferred energy required to sputter an atom is equal to the surface binding energy, E_s , material options ranges between 3.38 eV (Be) and 8.8 eV (W) [30]. At low ion energies, where the transferred energy to surface atoms is comparable with the surface binding energy, the sputtering yield decreases strongly and becomes zero below a threshold energy. For light ions incident on heavy materials, the threshold energy, E_{th} , is determined by the energy which can be transferred to target atoms and can be analytically approximated by expression[31],[32]:

$$E_{th} = \frac{(M_1 + M_2)^4}{4M_1M_2(M_1 - M_2)^2} E_s \quad (2.1)$$

where M_1 and M_2 are the incident particle mass and target mass respectively, and E_s is the surface binding energy. The energy dependence of the sputtering yields, Y , at normal incidence can empirically be described by the following expression:

$$Y = QS_n(E) \left(1 - \frac{E_{th}}{E}\right)^2 \left(1 - \left(\frac{E_{th}}{E}\right)^{2/3}\right), \quad (2.2)$$

where $S_n(E)$ is the function for the energy dependence on the energy deposited in elastic collisions. Values for the fitting parameters Q and E_{th} are tabulated for many ion-target combinations and given by Eckstein in Ref. [33].

Since plasma always contains impurities such as carbon (C), oxygen (O), and/or helium (He) produced by D-T reactions, the physical sputtering by intrinsic impurities might be significantly larger than that by fuel ions for high- Z target materials. The physical sputtering yield increases with the incidence angle of the projectile, since more energy can be transferred to the near surface layer for grazing incidence compared with normal incidence. For Be and W targets, experimental data and the fit for the

sputtering yield at normal incidence are shown in Fig. 2.1, as a function of incident particle energy.

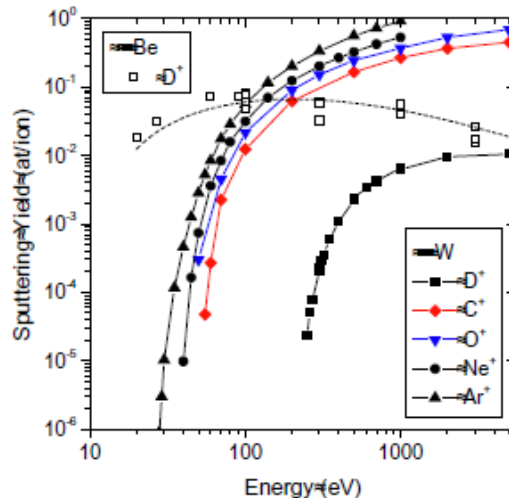


Figure 2.1: Energy dependence of the sputtering yields of Be and W bombarded by D, C, O, Ne and Ar ions. Experimental data are fitted using an empirical equation for the sputtering yields [33].

Physical sputtering data are available for both materials from energies close to the threshold energy (20 eV for D on Be and 200 eV for D on W) up to the high keV range and have been collected in data summaries. However, the situation is different for heavier ions, such as C, O, Ne or Ar. Heavier ions can transfer almost all their energy onto target atoms. In this case, the threshold energy is determined by the energy loss in inelastic stopping of atoms in the process of the reversal of momentum that requires several collisions inside the target. The resulting threshold energy is of the order of 4 to 8 times the surface binding energy E_s , i.e., about 30 eV for W (see Fig. 2.1). Therefore, the sputtering by the impurities is the main cause of both erosion of the plasma facing surface and plasma contamination by sputtered atoms. The dependence on angle of incidence is well described theoretically for light ions in Ref. [34], and parameter fits exist for light and heavy ions [33]. The self-sputtering yield of W versus angle of incidence at fixed energy of incidence is presented in Fig. 2.2.

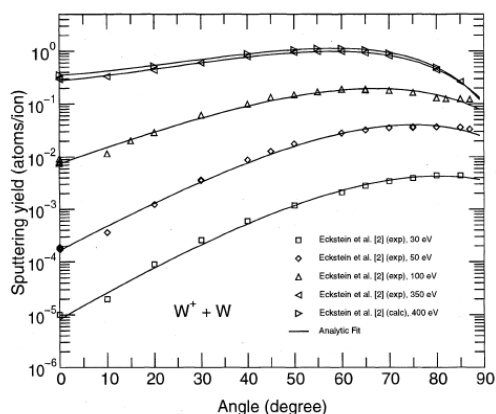


Figure 2.2: Self-sputtering yield of W versus angle of incidence (α) at fixed energy of incidence [35].

Non-normal incidence increases the deposited nuclear energy near the surface. The decrease at very grazing angles is due to surface reflection.

Furthermore, the high Z impurities can become multiply charged and accelerated to high impact energies by the sheath potential, which can lead to significant sputtering yields [36]. For equal temperatures of ions and electrons, the mean ion energy at the target is approximately $\langle E \rangle \approx 2k_B T + 3Zk_B T$ (k_B is the Boltzman constant), where the second term proportional to the ion charge Z is due to the acceleration in the sheath potential. This term is especially important for the physical sputtering of high- Z materials, where a low fraction of higher charged impurity ions leads to a substantial increase of Y_{phys} due to the increased energy of the projectile, since impurity ions also have a reduced threshold energy due to the higher mass.

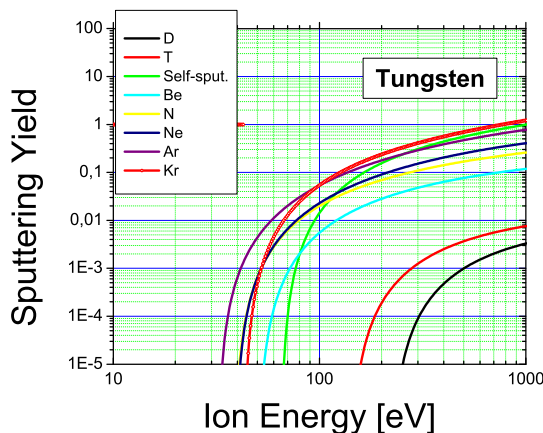


Figure 2.3: Sputtering yield of W by different impurities implemented in the COREDIV code.

In the COREDIV code, sputtering by every ion (main plasma and impurities) is considered and the yields are calculated based on the data given in Ref. [34]. The sputtering of W by different ions calculated in COREDIV code is presented in Fig. 2.3.

2.1.2 Chemical sputtering

Chemical erosion results from the formation and release of volatile molecules in the interaction of incident plasma particles and target atoms. It is characterized by the formation of volatile molecules during chemical reactions of the incident particles with the target atoms. Typical example: the formation of hydrocarbons in the interaction of hydrogen atoms with carbon surfaces. Chemical erosion (or sputtering) is important in case of carbon-based materials under the bombardment with hydrogen and oxygen leading to an emission of a wide spectrum of hydrocarbon molecules and carbon oxides. Physical and chemical erosion introduce different types of impurity sources into the plasma. Physically sputtered particles leave the surface as neutral atoms, but chemical erosion of carbon can produce various thermal neutral molecular sources, including hydrocarbon radicals, methane molecules and higher hydrocarbons. In each case, particles are ionized or dissociated by the plasma. In comparison with physical sputtering, chemical erosion is a much more complicated process, and its anal-

ysis relies heavily on measurements made in accelerators, linear devices and tokamak edge plasmas [37, 38].

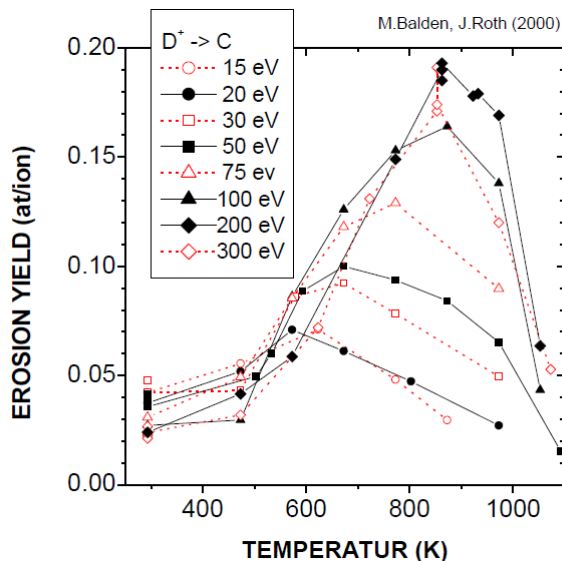


Figure 2.4: Chemical erosion for carbon by incident deuterium ion with different energy at elevated temperature.

As chemical reactions are involved, chemical erosion shows a strong dependence on the surface temperature in contrast to physical sputtering [see Fig. 2.4]. During the bombardment with hydrogen isotopes, the carbon atoms in the implantation zone are hydrogenated and form a complex $C-H$ bond structure there. With increasing surface temperature, radicals such as CH_3 are released, while at temperatures above 600K the recombination of hydrogen to H_2 prevails leading to a reduction of the erosion yield. These temperature controlled processes are supported by radiation damage owing to the energy transfer from the incident ions to the atoms in the lattice.

At low temperatures, no thermal release of hydrocarbons occurs. However, because of the much smaller binding energy of hydrocarbons ($E_s \sim 1$ eV) compared with carbon ($E_s = 7.4$ eV), incident ions can easily erode the hydrocarbons from the surface. This process is called ion-induced desorption of hydrocarbon radicals [38]. Because of the low E_s of hydrocarbons, chemical erosion has a significantly lower energy threshold, than physical sputtering. Impact energies above 50eV are required to obtain 0.5% physical sputtering yield of carbon by deuterium [39]; the same yield of chemical erosion, Y_{chem} , is obtained already at sub-eV impact energies [40]. The chemical erosion yield for carbon has a maximum at an elevated temperature, $T_{max} = 700 - 900$ K, and decreases at temperatures higher than T_{max} due to the release of hydrogen molecules [41].

Large erosion by chemical sputtering and large tritium retention in the redeposited layers are one of the main reasons to exclude carbon materials as plasma facing components in ITER.

2.1.3 ELMs and disruptions

Rapid plasma termination events called disruptions are usually the result of reaching one of the operational limits in tokamaks. The plasma disruptions can abruptly increase the heat loads on the solid surfaces, leading to melting of metallic PFCs. Disruptions can cause significant damage such as deformation of in-vessel structures, short circuits in external supplies due to induced eddy currents, as well as melting and vaporization of wall materials [42].

Operation in H-mode is generally assumed as the most likely scenario for next step tokamak fusion devices. H-mode plasmas develop a pronounced edge transport barrier and, hence, rather steep edge gradients, which can drive a variety of instabilities, especially quasi-periodic barrier relaxations, well known in the literature as edge localized modes (ELMs), which are characterized by a periodic expulsion of particles and thermal energy from the inner region at the separatrix into the edge plasma and finally parallel along the magnetic field lines onto the divertor and/or wall surfaces. The first classification of the different ELM phenomena was given for the DIII-D tokamak [43]. Three distinct types of ELM were found and numbered (the numbering indicating the historical sequence in which the ELM types were found). The original classification is based on three criteria: the dependence of the ELM repetition frequency ν_{ELM} on the heating power P , the occurrence of magnetic precursors and the MHD stability with respect to the ideal ballooning criterion.

- *Type I ELMs*, the ELM repetition frequency ν_{ELM} increases with heating power. There is no detectable magnetic precursor oscillation. However, the level of broadband magnetic and density turbulent fluctuations increases prior to a type I ELM. Ideal ballooning analysis shows that the plasma edge is always close to the stability limit $\alpha \approx \alpha_{crit}$ [44]. Type I ELMs appear as isolated sharp bursts on the D_α -signal.
- *Type II ELMs*, when the shape of the plasma cross section is changed towards higher elongation and triangularity, the appearance of the ELMs may change. They become more frequent and the magnitude of the D_α -burst decreases. In this case, the plasma edge is found to be in the connection regime between the first and the second stable region of the ballooning diagram [45]. For type II ELMs, no information on the power dependence of ν_{ELM} or the MHD precursor activity exists.
- *Type III ELMs*, the ELM repetition frequency decreases with heating power. A coherent magnetic precursor oscillation of frequency $\nu_{prec} \approx 50 \div 70$ kHz is observed on magnetic probes located close to the plasma in the outboard midplane. A toroidal mode number of $n \approx 5 \div 10$ was inferred. The plasma edge pressure gradient is significantly below the ideal ballooning limit, i.e. $0.3 \leq \alpha/\alpha_{crit} \leq 0.5$ [46].

Typical values of the ELM energies deposited at the divertor plates are for ASDEX-Upgrade, $0.1 \div 0.5$ MJ/m². A newly established scaling of the ELM energy fluency

using dedicated data sets from JET operation with CFC(Carbon Facing Component) and ILW plasma facing components, ASDEX Upgrade operation with both CFC and full-W PFCs and MAST with CFC walls has been prepared by T. Eich [47]. The result of this scaling gives a range in parallel peak ELM energy fluency of $10 \div 30$ MJ/m² for ITER $Q = 10$ operation and $2.5 \div 7.5$ MJ/m² for intermediate ITER operation at 7.5 MA and 2.65 T.

ELMs can abruptly increase the heat loads on the solid surfaces, leading to melting of metal PFCs and sublimation of carbon PFCs [48]. Macroscopic melting of metallic surfaces can inject large quantities of impurities into the confined plasma and radically deform the topology of the melted component [49]. In addition, microscopic surface deformities or regions of poor electrical conductivity can trigger electrical arcs - high currents of short duration, arising from the sheath potential between the plasma and the PFC. Arcs can cause fast evaporation and erosion of the PFC material even in the absence of transient events [50]. These discontinuous plasma wall interaction (PWI) processes are, however, outside the scope of this thesis.

2.1.4 Prompt redeposition

A favorable effect with respect to net erosion is the effect of prompt re-deposition. After leaving the material surface, the eroded impurities can re-deposit locally or be transported in the plasma into more distant regions. The migration of impurities depends on the PFC material properties, the edge plasma conditions, fundamental transport processes, and the magnetic field and machine geometry. Physical and chemical erosion introduce different types of impurity sources into the plasma. Physically sputtered particles leave the surface as neutral atoms but chemical erosion produces various neutral molecular sources, including hydrocarbon radicals, methane molecules and higher hydrocarbons [36], [38]. In each case, particles are ionized or dissociated by the plasma.

The ionization depth is a key parameter determining the fraction of impurities which are locally re-deposited. Ionization within a distance from the surface comparable with the impurity ion Larmor radius can lead to prompt re-deposition within the first gyration orbit [51]. Schematic depiction of prompt redeposition during the first cycle of gyration around the magnetic field line is shown in Fig. 2.5.

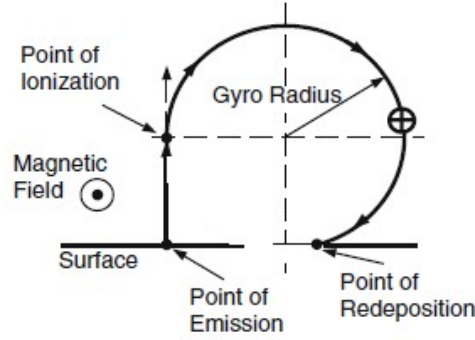


Figure 2.5: Schematic depiction of prompt redeposition during the first cycle of gyration around the magnetic field line. The magnetic field is directed toward the viewer as indicated [30].

The underlying mechanism is simple and the analytical derivation was found first by Fussmann [52], [53]. The fraction of the re-deposited atoms f_{prompt} is given by expression:

$$f_{prompt} = \frac{1}{\left(1 + \left(\frac{\lambda_{ion}}{\rho}\right)^2\right)} \quad (2.3)$$

where λ_{ion} is the ionization length calculated from ionization frequency and averaged thermal velocity and ρ is the gyro-radius of singly ionized atom in magnetic field. The resulting f_{prompt} is incorporated into (e.g. W) sputtering yield Y as follows: $Y_r = Y(1 - f_{prompt})$. Prompt re-deposition is expected to be more important for the heavy, high-Z elements which ionize rapidly and have a larger Larmor radius compared to low-Z elements like carbon. Using this simple model, the fraction of not promptly redeposited W ions escaping from divertor plate as a function of temperature at two magnetic fields (2T and 6.5T) for different electron densities is shown in Fig. 2.6.

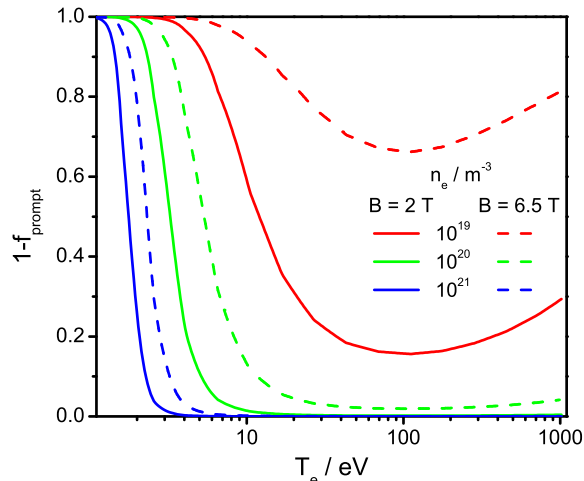


Figure 2.6: The fraction of not promptly redeposited W ions [54].

The prompt re-deposition process has almost not influence on the erosion when the magnetic field and the density increases and the plasma temperature is low $< 10\text{eV}$. The effect of the reduced sputtering yield due the prompt-re-deposition process is only important for relatively small levels of seeding, where temperature on the plate is high

$> 10\text{eV}$. The prompt re-deposition process in case of W plate was recently modeled with PIC (Particle In Cell) and Monte Carlo methods [55, 56].

2.1.5 Impurity seeding

Impurity seeding has been used for a long time in tokamak research [57]. The reduction of limiter and divertor power loads was also an early experimental goal in view of future devices. The presence of seed impurities not only reduces the plasma temperature in front of material surfaces. It also adds a new plasma species which leads to surface material sputtering. Depending on the seeded species and surface material, modifications of the surface structure have been observed. Only noble gases and nitrogen are considered as seed impurities recently, since non-recycling impurities such as carbon would lead to tritium co-deposition.

There are other various reasons to introduce impurities artificially. Impurities can be used as a diagnostic tool (Li-beam [58]), to study the impurity transport with a well-defined source (laser blow-off injection [59]), to mitigate ELMs [60] and disruptions.

2.2 Atomic processes in the plasma

The interaction of the plasma constituents are described by atomic physics. Various processes of electron collisions with atomic particles are classified in two group:

- bound - bound transitions
- bound - free transition,

which schematic is presented in Fig. 2.7.

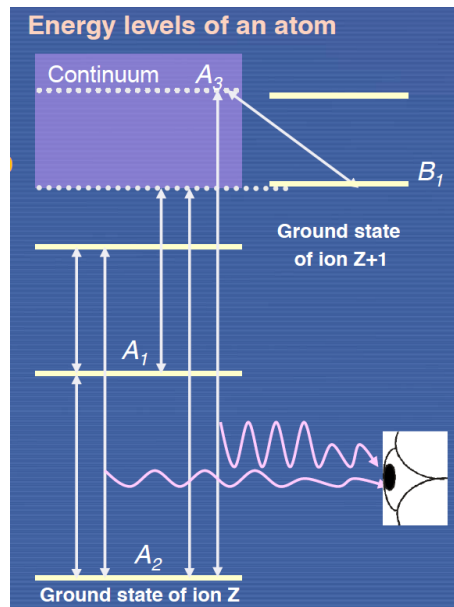


Figure 2.7: Energy levels and processes on the atoms[61].

The important reactions in impure plasmas are:

For bound - bound transitions

Spontaneous emission This is emission of the photon transitions from an highest energy state to lower energy state state. The schematic write as:

$$A_1 \rightarrow A_2 + h\nu_{12}, \quad (2.4)$$

where A_2 is first state and A_1 higher state of the atom, ν_{12} is the photon frequency and h is Plank constant. The radiation is called line emission and can only be generated by particles, that are not fully stripped of its electrons.

Photo-absorption or emission Photo-absorption is a linear absorption process whereby one photon excites an atom, ion or molecule from a lower energy level to a higher energy level, for example, from the ground state to the first excited state. The schematic write as:

$$A_2 + h\nu_1 \rightleftharpoons A_1 + h\nu_1 + h\nu_2 \quad (2.5)$$

The difference between absorption and emission spectra are that absorption lines are where light has been absorbed by the atom thus you see a dip in the spectrum whereas emission spectra have spikes in the spectra due to atoms releasing photons at those wavelengths.

Collisional excitation or de-excitation Excitation is process, when thermal kinetic energy of the free electrons in the plasma is transferred by collisions to the internal energy of the atom. Schematic presented as:

$$A_1 + e_1 \rightleftharpoons A_2 + e_2, \quad (2.6)$$

where $e_{1,2}$ is electrons.

For bound - free transition

Radiative recombination

$$B_1 + e \rightarrow A_2 + h\nu \quad (2.7)$$

A photon energy of $h\nu$ is realised, which is larger than the ionization energy of the atom or molecule.

Photoionization/stimulated recombination

$$B_1 + e \rightleftharpoons A_2 + h\nu \quad (2.8)$$

Collision ionization/three-body recombination Collision ionization is inelastic collision of ions or neutrals with an electron which can either ionize the particle. Schematic are:

$$B_1 + e_1 \rightleftharpoons A_2 + e_2, \quad (2.9)$$

where B_1 is ground state on ion $Z + 1$. This process determines the source rate for the ions in a fluid plasma description. Recombination is opposite process to ionization. Recombination is a sink term for ions, plasma energy and momentum and a source term for the electron energy.

Dielectronic recombination (autoionization +electron capture)

$$B_1 + e \rightleftharpoons A_3 \rightleftharpoons A_2 + h\nu \quad (2.10)$$

where the efficiency of dielectronic recombination in high-temperature plasmas is considerably larger than that of radiative recombination. In high-density plasmas, however, the effect of three-body recombination dominates.

Next important reaction is:

Associative ionization and dissociative recombination



Charge exchange



Charge exchange is the transfer of an electron from an atom to an ion when they collide. The cross-section of charge exchange can be large, and the process becomes important especially in the SOL region.

The emission of electromagnetic radiation and the interaction with neutrals is of particular importance for power dispersal and losses in the tokamak. The other transforms particles of one species into another one and can be included as source and sink terms in the fluid equations for different species, e.g. electron-impact ionization.

This ionisation and recombination determines the source rate for the ions in a fluid plasma description. In the analysis an atomic system in the plasma can be assumed:

- without transport: the plasma is assumed to be infinite in extent and of uniform electron density n_e and temperature T_e .
- excitation and ionization is due to electron impact only,
- charge exchange re-combination is included, requiring that the neutral density and temperature be specified,
- the plasma is optically thin, i.e. no radiation trapping

For this condition, the equilibrium distribution of plasma ions with their different charge states is given by balancing the processes of impact ionization and radiative recombination for each ionization state. This state is called coronal equilibrium. In the coronal equilibrium, the distribution of the impurity particles amongst the different charge states is purely a function of the electron temperature, with no dependence on the electron density [62]. Figure 2.8 shows the example for carbon and argon, based on the atomic data from COREDIV code.

The electron temperature at the separatrix in JET ILW and ASDEX Upgrade is about $100 \div 120eV$, but temperature in the pedestal region is about $1 \div 1.5keV$ (depending on discharge parameters, as plasma density, auxiliary heating...). For this condition, between pedestal and plasma center only C^{6+} and Ar^{17+}, Ar^{18+} can be observed. The ionization - recombination equilibrium in plasmas with high electron density-although this equilibrium may still be local and not influenced by transport - is not necessarily given by the coronal picture, since at higher n_e , electron- collisional de-excitation competes with spontaneous emission. Three-body recombination, with an electron acting as the third body to take away the recombination energy, ultimately exceeds two-body recombination at high n_e . In that case, the effective excitation, de-excitation, ionization and recombination rates are functions of both T_e and n_e .

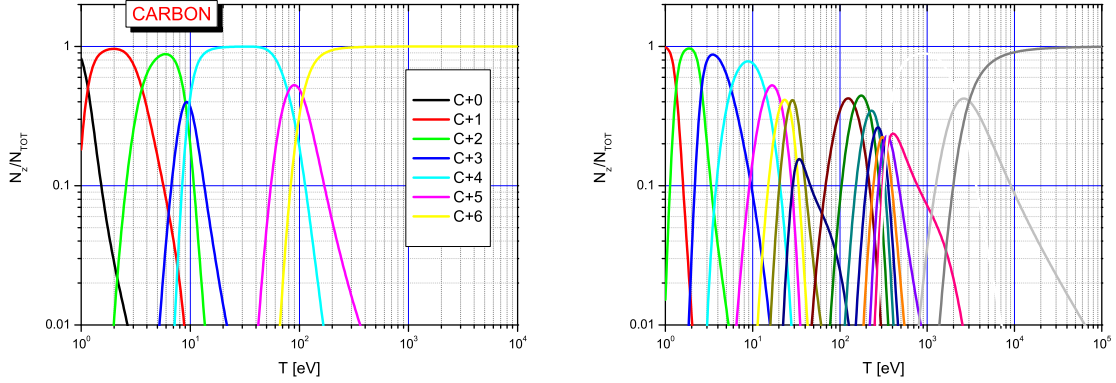


Figure 2.8: The carbon(left) and argon (right) equilibrium ionization state distribution.

2.3 Radiative processes in the plasma

Radiation distribution is an essential component of the power balance in tokamaks. The impurities relevant for fusion experiments can be classified into groups based on the emitted radiation, which in turn depends on the number of bound electrons and the plasma temperature: Low- Z impurities such as carbon, oxygen, boron and nitrogen have only few bound electrons and can be fast fully ionized. Their contribution to the total radiation is mainly at the plasma edge since in the core they are fully ionised. The mid- Z impurities as iron and nickel can radiate in whole plasma, whereas high- Z impurities such as tungsten radiate mostly in the plasma core.

All plasmas emit and absorb electromagnetic radiation. We identify the following contributions:

- *Line* radiation (bound-bound transition) corresponds to transitions of electrons between levels in atoms and ions, and at low temperatures also in molecules. Lines may become optically thick especially at long wavelengths and then they also reach the black-body limit. Since the bound electrons in the ion shells can only exist in discrete energy levels, the spectrum has a lines structure. It represents a major source of energy loss from the plasma especially in presence of heavy impurities which are not fully-stripped. This poses a severe restriction on the maximum level of impurity concentration that can be tolerated.
- *Bremsstrahlung* (free-free), a continuum radiation, is emitted when the electrons experience deflection in the electric field of the ions. At long wavelengths the optical depth becomes large and the bremsstrahlung approaches the black-body limit (Planck function). The power density is given by:

$$P_{brem} = 5.35 \times 10^{-27} n_e^2 Z_{EFF} \sqrt{T_e} [W/m^3], \quad (2.13)$$

where Z_{EFF} is effective charge is defined as:

$$Z_{EFF} = \frac{\sum n_i Z_i^2}{n_e}. \quad (2.14)$$

The energy loss by bremsstrahlung is proportional to Z^2 . Since Z_{EFF} increases with the impurity content, bremsstrahlung radiation also poses a limit for the

maximum impurity content in the plasma. For JET ILW for discharges without impurity seeding, the impurity which have strong influence on the Z_{EFF} is beryllium.

- *Recombination*(bound-free transition) consists of the emission of a photon after the capture of an electron by an ion. Its spectrum is continuous above a threshold energy corresponding to the binding energy of the captured electron.

Total power of continuous radiation, which is sum of the radiation of bremsstrahlung and recombination. Recombination radiation is neglected for the visible spectrum area. This gives the molarity of the determination the effective charge of the plasma Z_{EFF} .

Braking radiation emission occurs for cadmium photon energy, whereas recombination radiation emission occurs for photon energy sufficient for recombination with a specific ion ($h\nu \geq Z^2 R_y/n_e^2$, where R_y is Rydberg constant).

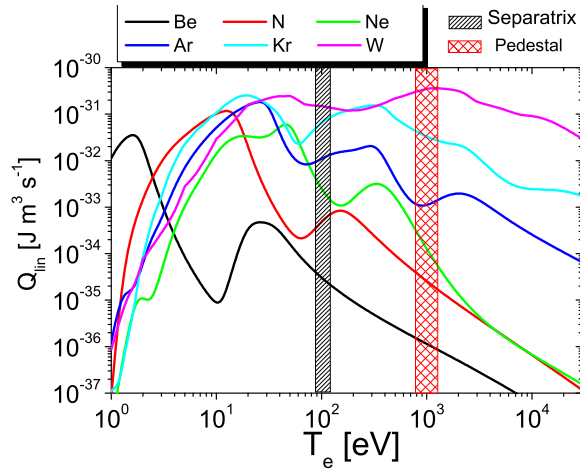


Figure 2.9: Cooling rate for Be, N, Ne, Ar, Kr, W in coronal equilibrium.

In the Fig.2.9 are shown cooling rates based on the atomic data implemented in COREDIV for Be, N, Ne, Ar, Kr, W in coronal equilibrium. Black and red marked area corresponds to temperatures in JET ILW for separatrix and pedestal. We see, that low Z-impurity like to Be, N radiate mostly in the SOL, but Ar (dark blue line) have maximum of the radiation between separatrix and pedestal. For high Z-impurity (W) main radiation is in the core region.

Chapter 3

Basic of plasma transport

A plasma is an ensemble of charged particles: electrons e , ions i and neutrals n with different positions \mathbf{r} and velocities \mathbf{V} which move under the influence of external forces (electromagnetic fields) and internal collision processes (Coulomb collisions, ionization, charge exchange etc.). The motion of each particle in electric and magnetic field is described by Lorenz force law. To describe the plasma dynamics different approaches are used:

- singles particles - equation of motion is solved for every single particle
- kinetic, where particles are treated as assemble of particles with distribution function
- fluid, where different types of particles are treated as different fluids
- hybrid: kinetic/fluid.

3.1 Kinetic and fluid description of plasma in tokamak

In kinetic description, the plasma state is given by one particle distribution function $f_a(\mathbf{r}, \mathbf{V}, t)$. The kinetic equation describes the evolution of the distribution function in time. The distribution function is interpreted as the probability density in the six-dimensional phase space combining three-dimensional geometrical (real) space and three-dimensional velocity space, normalized to the number of particles. The external electric \mathbf{E} and magnetic \mathbf{B} fields impose forces on charged particles a with the nuclear charge number Z_a and mass m_a . A kinetic description with the absence of collisions is given by solution of the Vlasov equation Eq. 3.1:

$$\frac{\partial f_a}{\partial t} + \mathbf{V} \cdot \frac{\partial f}{\partial \mathbf{r}} + \frac{Z_a}{m_a} (\mathbf{E} + \mathbf{V} \times \mathbf{B}) \cdot \frac{\partial f}{\partial \mathbf{V}} = 0 \quad (3.1)$$

in the standard form. The proper collision kinetic equation for plasma for small angle collisions is the Fokker-Planck equation Eq. 3.2

$$\frac{\partial f_a}{\partial t} + \mathbf{V} \cdot \frac{\partial f_a}{\partial \mathbf{x}} + \frac{Z_a}{m_a} (\mathbf{E} + \mathbf{V} \times \mathbf{B}) \cdot \frac{\partial f}{\partial \mathbf{V}} = C_a + S_a \quad (3.2)$$

where in right side of the equation C_a is Coulomb collision operator and S_a is external particle source term. Using the complete distribution function is usually neither practical nor feasible. Often the moments of the distribution function are used to describe the plasma evolution in a fluid approach. The basic idea of the fluid model is to take the medium of interest, in this case a plasma, and subdivide it into a large number of small, moving fluid elements and each element is assumed to contain a large number of particles. The fluid model describes the plasma based on macroscopic quantities (velocity moments of the distribution function such as density, mean velocity, and mean energy). A fluid approach is only valid if the plasma constituents are sufficiently coupled via collisions, such that the distribution function is close to a Maxwellian. By averaging the kinetic equation for each species of particles over velocities, we can construct the formal system of moment equations:

the particle conservation equation or continuity equation

$$\frac{\partial n_a}{\partial t} + \nabla \cdot (n_a \mathbf{V}_a) = S_a^m \quad (3.3)$$

where n_a is the particle density, \mathbf{V}_a is the fluid velocity and S_a^m is the particle source/sink.

the momentum conservation equation

$$m_a n_a \left[\frac{\partial \mathbf{V}_a}{\partial t} + (\mathbf{V}_a \cdot \nabla) \mathbf{V}_a \right] - Z_a n_a (\mathbf{E} + \mathbf{V} \times \mathbf{B}) + \nabla p_a + \nabla \cdot \Pi_a = \mathbf{R}_{ab} + S_a^m \quad (3.4)$$

where p_a is the pressure, Π_a is the viscosity tensor, \mathbf{R}_{ab} is the friction force exerted on particles of type a by particles of type b and S_a^m is the momentum source/sink.

the energy conservation equation

$$\frac{\partial}{\partial t} \left[\frac{3}{2} p_a + \frac{m_a n_a}{2} V_a^2 \right] + \nabla \cdot \left[\left(\frac{5}{2} p_a + \frac{m_a n_a}{2} V_a^2 \right) \mathbf{V}_a + \mathbf{q}_a + \mathbf{V}_a \otimes \cdot \Pi_a \right] = Q_{ab} + Q_{ohm} + S_a^e \quad (3.5)$$

where \mathbf{q}_a is conductive heat flux of species a , S_a^e is energy sources (due to ionization, recombination, auxiliary heating), Q_{ohm} is ohmic heating and Q_{ab} is the collisional energy transfer between particles of different species. Such calculations have been carried out by a number of workers, but Braginskii [63] has given a clear and comprehensive presentation and results equation have his name. The electric and magnetic fields can be obtained from Maxwells equations with the charge density $\rho = \sum_a e Z_a n_a$ and current density $\mathbf{j} = \sum_a e Z_a n_a \mathbf{V}_a$ [41].

Another property concerning the validity of fluid models is the size of a fluid element. For a fluid model to be valid it must be possible to define a range of sizes for each element, that satisfies two conflicting requirements.

3.1.1 Equations for the core in COREDIV code

In tokamak due to the very fast transport of particles along magnetic field lines, the plasma transport inside separatrix can be treated as 1D radial transport with all variables averaged over magnetic surfaces.

In the COREDIV code, the 1D radial transport equations for bulk ions, for each ionization state of impurity ions and for electron and ion temperature are solved. Equations for plasma rotation and plasma current has been neglected, the current is given as input function. The exact transport equations used in COREDIV code have the same structure as the presented above equations. Their actual form for core plasma is given in Ref. [64]. The continuity equation Eq. 3.3 for main plasma ions:

$$\frac{\partial n_i}{\partial t} + \frac{1}{rg_1} \frac{\partial}{\partial r} \left[rg_2 \left(-D_i \frac{\partial n_i}{\partial r} + n_i V_i^{pinch} \right) \right] = S_i(r), \quad (3.6)$$

and for impurity ions:

$$\frac{\partial n_j^k}{\partial t} + \frac{1}{rg_1} \frac{\partial}{\partial r} (rg_2 \Gamma_j^k) = n_e [n_{j-1}^k \alpha_{ion,k}^{j-1} - n_j^k (\alpha_{ion,k}^j + \beta_{rec,k}^j) + n_{j+1}^k \beta_{rec,k}^{j+1}]; j = 1, \dots, Z_k, \quad (3.7)$$

where r is radial coordinate, $g_1 = V'$ and $g_2 = |\nabla \rho|^2$ are metric coefficients, $j = 1, \dots, Z_k$ corresponds to ionization stages of impurity type k , with Z_k being the atomic number, the α^j and β^j are ionization and recombination rate coefficient, respectively. The metric coefficients are calculated under the assumption that the magnetic configuration is defined only by the elongation parameter $k(r) = (k(a) - 1)(r/a)^{0.25} + 1$, where a is minor radius of the tokamak. The impurity fluxes are:

$$\Gamma_j^k = -D_j^k \frac{\partial n_j^k}{\partial r} + n_j^k V_j^{pinch,k} \quad (3.8)$$

The electron density (n_e) is calculated from the quasi-neutrality condition:

$$n_e = n_i + \sum_{k,j} n_j^k \quad (3.9)$$

The equations for electron and ion temperatures are:

$$\frac{3}{2} \frac{\partial n_i T_i}{\partial t} + \frac{1}{rg_1} \frac{\partial}{\partial r} [rg_2 (-k_i \frac{\partial T_i}{\partial r} + \frac{5}{2} \Gamma_i T_i)] = P_{aux}^i + Q_{ei} \quad (3.10)$$

$$\frac{3}{2} \frac{\partial n_e T_e}{\partial t} + \frac{1}{rg_1} \frac{\partial}{\partial r} [rg_2 (-k_e \frac{\partial T_e}{\partial r} + \frac{5}{2} \Gamma_e T_e)] = P^{OH} + P_{aux}^e + P_\alpha - P_B - P_{cyc} - P_{line} - P_{ion} - Q_{ei}, \quad (3.11)$$

where P_{aux} is the auxiliary heating power, P_{OH} is Ohmic heating, P_B , P_{line} , are energy losses due to bremsstrahlung and line radiation, respectively. P_α is alpha power and Q_{ei} is collisional energy exchange between electrons and ions. Ionization losses are sum over all ionization states for all ions and are given by the expression:

$$P_{ion} = \sum_{j,k} n_e n_j^k \alpha_{ion,k}^j I_j^k \quad (3.12)$$

where I_j^k is ionization potential for k - ion in j ionization state. Similarly, P_{line} is given by:

$$P_{lin} = \sum_{j,k} n_e n_j^k \varepsilon_j^k(T_e) \quad (3.13)$$

where $\varepsilon_j^k(T_e)$ is the cooling rate.

It should be noted that in the COREDIV code equations for the plasma rotation and current are neglected for simplicity. They are important for the studies of the equilibrium evolution which is outside the scope of this thesis. Instead the magnetic field and current are assumed to be given (from other models or experiment).

The electron and ion energy fluxes are defined by the local transport model.

3.1.2 Equations for the scrape-off layer plasma in COREDIV code

The fluid equations: In tokamaks, the plasma dynamics in the edge region (outside separatrix) is at least two dimensional, it depends on the fast transport along field lines and on the slow, diffusive transport in the direction perpendicular to the magnetic surfaces. Therefore, in majority of the edge codes radial and poloidal (projection of the parallel direction on poloidal plane) are considered. The fluid equations used for SOL in the COREDIV code are the following:

particle balance:

$$\frac{\partial n_a}{\partial t} + \frac{1}{\sqrt{g}} \left(\frac{\partial}{\partial x} \frac{\sqrt{g}}{h_x} n_a v_x^a + \frac{\partial}{\partial y} \frac{\sqrt{g}}{h_y} \Gamma_y^a \right) = S_n^a \quad (3.14)$$

parallel momentum balance:

$$\begin{aligned} & \frac{\partial}{\partial t} (m_a n_a v_{||}^a) + \frac{1}{\sqrt{g}} \frac{\partial}{\partial x} \left(\frac{\sqrt{g}}{h_x} m_a n_a v_x^a v_{||}^a - \eta_x^a \frac{\sqrt{g}}{h_x^2} \frac{\partial v_{||}^a}{\partial x} \right) + \\ & \frac{1}{\sqrt{g}} \frac{\partial}{\partial y} \left(\frac{\sqrt{g}}{h_y} m_a n_a v_y^a v_{||}^a - \eta_y^a \frac{\sqrt{g}}{h_y^2} \frac{\partial v_{||}^a}{\partial y} \right) = -\frac{h_\Theta}{h_x} \frac{\partial p_a}{\partial x} + e Z_a n_a E_{||} + R_{||}^a + m_a S_{v_{||}}^a \end{aligned} \quad (3.15)$$

diffusion equation:

$$\Gamma_y^a \equiv n_a v_y^a = -D_{perp}^{SOL,a} \frac{1}{h_y} \frac{\partial n_a}{\partial y} \quad (3.16)$$

ion energy balance:

$$\begin{aligned} & \frac{3}{2} \frac{\partial}{\partial t} \left(\sum_a n_a T_i \right) + \frac{1}{\sqrt{g}} \sum_a \left[\frac{\partial}{\partial x} \frac{\sqrt{g}}{h_x} \left(\frac{5}{2} n_a v_x^a T_i + q_x^a \right) + \frac{\partial}{\partial y} \frac{\sqrt{g}}{h_y} \left(\frac{5}{2} n_a v_y^a T_i + q_y^a \right) \right] \\ & + \frac{1}{\sqrt{g}} \sum_a v_x^a \left[\frac{\partial}{\partial x} \left(\eta_x^a \frac{\sqrt{g}}{h_x^2} \frac{\partial v_{||}^a}{\partial x} \right) + \frac{\partial}{\partial y} \left(\eta_y^a \frac{\sqrt{g}}{h_y^2} \frac{\partial v_{||}^a}{\partial y} \right) \right] = \sum_a v_x^a \frac{1}{h_x} \frac{\partial p_a}{\partial x} + \sum_a Q_{ea} + \sum_a S_E^a \end{aligned} \quad (3.17)$$

electron energy balance:

$$\frac{3}{2} \frac{\partial n_e T_e}{\partial t} + \frac{1}{\sqrt{g}} \frac{\partial \sqrt{g}}{\partial x} \frac{1}{h_x} \left(\frac{5}{2} n_e v_x^e T_e + q_x^e \right) + \frac{1}{\sqrt{g}} \frac{\partial \sqrt{g}}{\partial y} \frac{1}{h_y} \left(\frac{5}{2} n_e v_y^e T_e + q_y^e \right) = \quad (3.18)$$

$$v_x^e \frac{1}{h_x} \frac{\partial p_e}{\partial x} - \sum_a Q_{ea} + S_E^e$$

where coordinates x and y correspond to the poloidal and radial directions, respectively; $a = i$ for deuterium ions and $a = k, j$ for the different charge states of impurity ions of type k ($j = 1, \dots, Z_{max}^k$). \sqrt{g} , h_x and h_y are metric coefficients; the coordinate system can be curvilinear, although it has to be orthogonal. $h_\Theta = B_\Theta/B$ is the ratio between poloidal and total magnetic field. n_a , m_a , Z_a are the density, mass and charge of species a . The terms S_n^a , \vec{S}_v^a represent volume sources of particles and momentum while S_E^e , S_E^a are volume sources of electron and ion energy, respectively. R_T^a , R_U^a are thermal and friction forces ($R_{\parallel}^a = R_T^a + R_U^a$). Diffusion coefficients $D_{perp}^{a, SOL}$ are anomalous in the model and $q_x^{e,a}$, $q_y^{e,a}$ are the poloidal and radial heat fluxes. Q_{ea} is the energy equilibration term, η_x^a and η_y^a are poloidal and radial viscosity coefficients, v_{\parallel}^a , v_x^a and v_y^a are parallel, poloidal and radial components of the flow velocity, respectively, and v_x^e , v_y^e are the poloidal and radial components of the electron flow velocity. E_{\parallel} is the parallel electric field and $\alpha_T \simeq 0.71$.

Equations of different fluids are coupled by electrostatic, friction and thermal forces as well as by atomic processes such as collisional ionization, recombination excitation and charge exchange. The friction and thermal force, given by Igithanov [65] are:

for electrons:

$$R_e^U = -m_e n_e k_u (Z_{EFF}) (\nu_{e,i} U_{e,i} + \sum_j \nu_{e,z_j} U_{e,z_j}) \quad (3.19)$$

$$R_e^T = -n_e k_T^1 (Z_{EFF}) \nabla_{\parallel} T_e \quad (3.20)$$

for main plasma ions :

$$R_i^U = -m_i n_i \left[k_u (Z_{EFF}) (\nu_{e,i} U_{e,i} + k_u^1 \sum_j \nu_{e,z_j} U_{e,z_j}) \right] \quad (3.21)$$

$$R_i^T = -n_i k_T^1 (Z_0) \nabla_{\parallel} T_i + n_i k_T^2 (Z_{EFF}) \left(\frac{m_i \nu_{ie}}{m_e \nu_e} \right) \nabla_{\parallel} T_e \quad (3.22)$$

for impurity ions:

$$R_{Z_j}^U = -m_z n_{Z_j} \left\{ k_u (Z_{EFF}) \nu_{e,Z_j} U_{e,Z_j} + k_u^1 (Z_{EFF}) \nu_{e,Z_j} U_{i,Z_j} + 0.84 \sum_{k \neq j} \nu_{z_k, z_j} U_{z_j, z_k} \right\} \quad (3.23)$$

$$R_{Z_j}^T = -m_z n_{Z_j} k_T^2 Z_{EFF} \frac{\nu_{Z_j, e}}{\nu_e} \frac{\nabla_{\parallel} T_e}{m_e} + n_i k_T^2 (Z_0) \frac{\nu_{Z_j, i}}{\nu_i} \frac{\nabla_{\parallel} T_i}{m_i} + 0.6 \left(\frac{Z_j^2 \sum n_{Z_j}}{\sum_k Z_k^2 n_{Z_k}} - 1 \right) \frac{\nabla_{\parallel} T_e}{m_{Z_j}}, \quad (3.24)$$

, where Z_0 is:

$$Z_0 = Z_{EFF} \frac{n_e}{n_i} - 1 \quad (3.25)$$

and coefficients $k(x)$ are expressed as:

$$k_u(x) = \frac{(1 + 0.24x)(1 + 0.93x)}{(1 + 2.65x)(1 + 0.285x)} \quad (3.26)$$

$$k_u(x)^1 = k_u(Z_0) + \frac{0.04(1 + 0.3Z_{EFF})}{(1 + 2.65x)(1 + 0.285x)} \sqrt{\frac{m_i + m_e}{m_z}} \quad (3.27)$$

$$k_T(x)^1 = \frac{2.2x(1 + 0.52x)}{(1 + 2.65x)(1 + 0.285x)} \quad (3.28)$$

$$k_T(x)^2 = \frac{0.7(1 + \sqrt{2}x)k_T(x)^1}{x} \quad (3.29)$$

The set of equations 3.14-3.18 describes multi-fluid plasma transport in the edge region of a tokamak, when volume sources, boundary conditions and an appropriate model for neutrals are specified. It takes into account the plasma (deuterium and seeded impurities) recycling in the divertor as well as the sputtering processes at the target plates including deuterium/tritium sputtering, self-sputtering and sputtering due to seeded impurities. The recycling coefficient is an external parameter and the energy losses due to interactions with hydrogenic atoms (line radiation, ionization and charge exchange) are accounted for in the model.

Sources in fluid equations

In COREDIV code, the deuterium and impurity neutrals in the neighborhood of the target plates are described by an analytical model, which accounts for recycling and sputtering processes Ref.[66].

Deuterium neutrals: In the case of deuterium two groups of neutrals are considered: fast and slow neutrals ($N_D = N_D^f + N_D^s$). The profile of deuterium atoms is prescribed by a product of exponential functions:

$$N_D^{f,s}(x, y) = N_{f,s}^{plate} \exp\left(-\frac{|x_{plate} - x|}{\lambda_x^{f,s}}\right) \exp\left(-\frac{(y_M - y)^2}{\lambda_y^{f,s}}\right), \quad (3.30)$$

where $\lambda_{x,y}^f = v_{Dx,y}^f / (n_e \sqrt{\alpha_i^D \alpha_{cx}^D})$, $\lambda_{x,y}^s = v_{Dx,y}^s / (n_e \alpha_i^D)$, α_i^D , α_{cx}^D are the rate coefficients for ionization and charge exchange processes, respectively, x_{plate} is the position of the target plate, while y_M is the position of the maximum neutral particle reflux from the target plate. The deuterium neutral densities $N_f^{plate} = \frac{3}{4}N^{plate}$ and $N_s^{plate} = \frac{1}{4}N^{plate}$ at the target plate depend on the recycling coefficient, R , and may be found from the integral relation:

$$\int_{VOL} N_D(x, y) \alpha_i^D(x, y) n_e(x, y) dV = R \int_{plate} |n_i v_x^i(x_{plate}, y)| dS, \quad (3.31)$$

where VOL is the volume of the boundary layer and R for deuterium is defined by following relation:

$$0 \leq R = \frac{\Psi_D - \Psi_{sep}}{\Psi_D} < 1, \quad (3.32)$$

where Ψ_D is particle flux to the plate and Psi_{sep} is the particle flux to the SOL.

It is assumed that the velocity of the neutrals equals to the ion velocity for fast neutrals and it is equal to the thermal velocity in the case of slow neutrals. For fast neutrals the deuterium temperature T_D^f is determined as an average of two equilibrium temperatures: $T_D^f = 0.5(T_D^{cx} + T_D^{eq})$. The temperature T_D^{cx} follows from the assumption of charge exchange equilibrium, whereas the temperature T_D^{eq} is determined from the condition that plasma ions and neutrals have the same energy. For slow Franck-Condon neutrals it is assumed that they have constant temperature $T_D^s = 2 \text{ eV}$.

Sputtered impurity: The density profile of impurity atoms is determined by transport processes in the SOL and by the sputtering phenomena at the plates. It is similar to the deuterium profile (eq.3.30), but now $\lambda_{Zx,y} = \lambda_{ion}^Z = v_Z^{th} / (n_e \alpha_i^Z)$ is the ionization length for impurity atoms, with N_Z^{plate} can be found from the following condition

$$\int_{VOL} N_Z(x, y) \alpha_i^Z(x, y) n_e(x, y) dV = \int_{plate} \left| Y_D \Gamma_x^D + \sum_{j=1}^{Z_{max}} Y_j \Gamma_x^j \right| (x_{plate}, y) dS \quad (3.33)$$

where N_Z is the density of impurity atoms and α_i^Z is their ionization rate coefficient. Sputtering yields Y_D, Y_j are functions of the ion energy and angle of incidence [67].

Gas-puff impurity: In order to model divertor cooling by localized fuelling of noble gasses we have assumed a source of impurity neutrals at the wall. The density profile of impurity neutrals is prescribed in that case by the following product of exponential functions:

$$N_z^{puff}(x, y) = N_{wall}^{puff} \exp \left(- \left| \frac{x_{puff} - x}{0.5 w_{puff}} \right|^3 \right) \exp \left(- \left| \frac{y_{wall} - y}{\lambda_z^{inj}} \right| \right) \quad (3.34)$$

where w_{puff} is the poloidal extension of the gas-puff source, λ_z^{inj} is the ionization mean free path of the injected neutrals, x_{puff} is the poloidal position of the middle of the gas-puff source, while y_{wall} is the radial position of the wall. The impurity neutral density at the wall N_{wall}^{puff} is determined by the influx from the gas-puff source:

$$\int_{VOL} N_z^{puff}(x, y) \alpha_i^z(x, y) n_e(x, y) dV = \Gamma_{puff}^z \quad (3.35)$$

3.2 Transport process

A given charged particle is subjected to fluctuating forces due to the movement of the other charged particles in the plasma, which cause fluctuations of the electric and magnetic field. For fluctuation with typical length scales below or equal to the Debye shielding length, we speak of Coulomb collisions and collisional transport. For plasma fluctuations with typical length scales much larger than Debye shielding length, we speak of turbulence and anomalous transport. The turbulent transport in the tokamak plasma has little influence on the transport parallel to the field lines.

The transport along the magnetic field is much larger than perpendicular to the field. Thus, the impurity density and temperature are to lowest order constant on a flux surface. We are mainly interested in the transport between flux surfaces, the

so-called radial transport. When averaging the transport equation over a flux surface, one obtains the radial impurity transport equation. For a flux surface label r , which has a simple relation to the volume enclosed by the flux surface $V = \pi r^2 2\pi R_{axis}$, the radial transport equation has a simple analytical form:

$$\frac{\partial n_{Z,j}}{\partial t} + \frac{1}{r} \frac{d}{dr} \left(\underbrace{D \frac{\partial n_{Z,j}}{\partial r}}_{\text{diffusion}} - \underbrace{V_d n_{Z,j}}_{\text{convection}} \right) = S_{Z,j}^n, \quad (3.36)$$

where $n_{Z,j}$ is particle density of the impurity in ion stage j , D here represents the flux surface averaged radial diffusion coefficient and V_d the flux averaged drift velocity. $D_{Z,j}$ is always positive and therefore acts in the opposite direction to the impurity density gradient, whereas $V_d n_{Z,j}$ can be positive or negative depending on the physical driving mechanism for the transport. The flux density of the impurity Γ is:

$$\Gamma = \left(\partial \frac{dn_{Z,j}}{\partial r} - V_d n_{Z,j} \right) \quad (3.37)$$

Both neoclassical and anomalous transport contributes to D and V_d and will be described in the following sections. The source/sink term S_Z^n coupling the transport equation of each ionisation stage with the neighbouring stages is:

$$S_{Z,j}^n = n_e n_{Z,j-1} \alpha_{Z,j-1} + n_e n_{Z,j+1} \beta_{Z,j+1} - n_e n_{Z,j} (\alpha_{Z,j} + \beta_{Z,j}), \quad (3.38)$$

where $\alpha_{Z,j-1}$ is rate coefficient for conization of the impurity species in ionization state j and $\beta_{Z,j}$ is the recombination coefficient form ionisation stage j .

The radial impurity flows can either be driven by the radial impurity gradients being caused by diffusion, but may also have a convective component, which is inwardly or outwardly directed independent of the impurity gradient. The radial transport requirements for helium and the other impurities are somewhat different. For the case of the fusion produced helium, there is a central source of helium ions, which maintains the radial gradient to the outside, and in equilibrium, diffusion leads to a steady outwardly directed net flow of helium. For edge produced impurities, also the role of the convective flows are very important, since they can provoke strong radial impurity gradients for cases, where the directed convective component is the dominant.

3.2.1 Classical impurity transport

In the particle picture, classical transport can be understood as a random walk process where every collision time τ_{col} the gyrating ions are radially displaced by a Larmor radius r_L . This leads to a diffusion coefficient $D_{CL} \approx r_L^2 / \tau_{col}$. The collision time is given by $\tau_{col} = 1/\nu$, where ν is the collision frequency. The ion thermal diffusivity is given by $\chi_{CL} \approx r_L^2 \nu$. The collision frequency for momentum transfer from species b onto species a for equal temperatures is:

$$\nu_{ab} = \frac{4\sqrt{2\pi}}{3(4\pi\epsilon_0)^2} \frac{\sqrt{m_{ab}}}{m_a} \frac{Z_a^2 Z_b^2 \ln \Lambda_{ab}}{(k_B T)^{3/2}} n_b, \quad (3.39)$$

where $m_{ab} = m_a m_b / (m_a + m_b)$ is the reduced mass for particles a and b , and $\ln \Lambda_{ab}$ is Coulomb logarithm. The classical diffusive term is :

$$D_a^{cl} = \frac{4\sqrt{2\pi}}{3(4\pi\epsilon_0)^2 B_T^2} \frac{1}{\sqrt{k_B T}} \sqrt{m_{ab}} Z_b^2 \ln \Lambda_{ab} n_b \quad (3.40)$$

The diffusion coefficient is independent of the charge Z_a . The main contributions come from collisions with ions, while friction with electrons can be neglected due to the small electron mass. Classical transport is very small and typical values in tokamaks are $D_Z^{cl} \approx \chi_Z^{cl} 10^{-5} \div 10^{-4} m^2 s^{-1}$, but there are additional contributions to the particle transport described by neoclassical theory.

3.2.2 Neoclassical impurity transport

Classical transport describes the collisional transport in a cylindrical plasma, in the presence of a homogeneous magnetic field. Tokamaks operate with a toroidal plasma geometry, which causes a geometrical enhancement of the transport coefficients. However, in tokamaks the magnetic field has a curvature, which introduces additional effects such as the trapping of particles due to the magnetic field curvature and the $\nabla \mathbf{B}$ drift, that are not taken into account in the classical transport theory. The corrections to the classical transport theory for a plasma with toroidal geometry are given by the neoclassical transport theory. The full derivation of the neoclassical terms is given in the overview by Hirshman and Sigmar [68]. The neoclassical part of the fluxes depends on the plasma collisionality ν^* defined as the ratio of the collision frequency ν and the particle bounce frequency $\nu_b = \epsilon^{3/2} v_{th} / qR$ of a trapped particle, where q is the safety factor, r is the minor radius of the flux surface, R is the major radius of the tokamak and $\epsilon = r/R$ is the inverse aspect ratio of the flux surface. We have two regime dependence on collisionality:

- high collisionality regime: $\nu^* > \epsilon^{3/2}$ is called the Pfirsch-Schluter (PS) regime.

Pfirsch-Schluter impurity transport

The Pfirsch-Schluter (PS) flux results from the *poloidal variation of the parallel friction forces* due to pressure and temperature variations within a magnetic surface. It is the dominant flux term in the short mean free path regime and it is given by [69]

$$D_Z^{PS} = 2q^2 K D_Z^{cl} \quad (3.41)$$

$$V_Z^{PS} = D_Z^{PS} \frac{Z}{Z_D} \left[\frac{\nabla n_D}{n_D} + \frac{H}{K} \frac{\nabla T_i}{T_i} \right], \quad (3.42)$$

where coefficient K and H are:

$$K = 1 - \frac{0.52\alpha}{0.59 + \alpha + 1.34g^{-2}} \quad (3.43)$$

$$H = 0.5 + \frac{0.29 + 0.68\alpha}{0.59 + \alpha + 1.34g^{-2}} \quad (3.44)$$

where α is the impurity strength parameter $\alpha = n_Z Z_Z^2 / n_D Z_D^2$ and g is the the working ion collisionality parameter, $g = \epsilon^{3/2} \nu_D^*$ is: $g = \epsilon^{3/2} \nu_D^* = (\nu_{DD} + \nu_{DZ}) R_0 q / (v_{th} \epsilon^{3/2})$.

- low collisionality regime: $\nu^* < 1$ is called the banana-plateau (BP) regime

Banana-plateau impurity transport

The banana-plateau flux is driven by the surface averaged pressure tensor anisotropies and is dominant in the long mean free path regime. The banana-plateau diffusive term is:

$$D_Z^{BP} = \frac{3}{2} \frac{k_B T_i A_Z^{BP}}{Z^2 e^2 B_\psi^2 R^2 n_Z} \quad (3.45)$$

and banana-plateau convective term is:

$$V_Z^{BP} = D_Z^{BP} \left(\frac{Z}{Z_D} \frac{\nabla n_D}{n_D} + \alpha_{TD}^{BP} \frac{\nabla T_i}{T_i} \right) \quad (3.46)$$

with

$$\alpha_{TD}^{BP} = \frac{3}{2} \left(1 - \frac{Z}{Z_D} \right) + \left(\frac{Z}{Z_D} \frac{K_{12}^D}{K_{11}^D} \right) \quad (3.47)$$

Illustration of the dependence of the diffusion coefficients on collisionality and the identification of the different regimes contributing to neoclassical transport are shown in Fig. 3.1. The edge of the plasma is mostly in the Pfirsch-Schluter regime. The

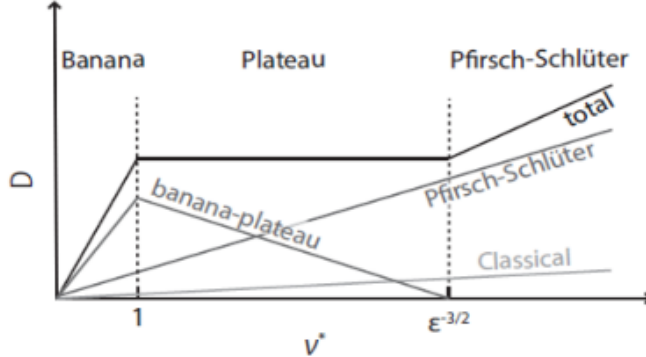


Figure 3.1: Illustration of the dependence of the diffusion coefficients on collisionality and the identification of the different regimes contributing to neoclassical transport [2].

transport in the region in between is characterised by both banana-plateau and Pfirsch-Schluter contributions. The classical contribution is small in all plasma regions. The total neoclassical drift velocity is the sum of the drift coefficients in each of the regimes. The drift velocity in each regime is driven by the gradients in deuterium density and ion temperature.

3.2.3 Anomalous transport

Plasma turbulence is the result of non-linear interaction between small scale parameter fluctuations of the order of the ion Larmor radius, which are driven unstable mainly by the plasma currents and the spatial gradients in temperature and density.

These types of instability are called micro-instabilities and the study of plasma behaviour on spatial scales comparable to the gyro-radius is the subject of gyro-kinetic theory.

The term *anomalous transport* reflects the surprise, which was aroused by the finding, that experimentally determined heat conductivities exceeded the neoclassical predictions for the ions by one and for the electrons by two orders of magnitude [70] and are supposed to be of turbulent nature. Also the diffusion coefficient of impurities can be several m²/s in the experiment, which is about an order of magnitude above the neoclassical value. Local fluctuations in density, temperature and the electrostatic potential lead to fluctuating $\mathbf{E} \times \mathbf{B}$ -drifts, so-called drift waves. The precursors of the corresponding, dominant instabilities are Ion Temperature Gradient (ITG) mode, the Electron Temperature Gradient (ETG) mode and the Trapped Electron Mode (TEM). The instabilities occur in different regimes in the form of single or mixed instabilities. Turbulent transport in a tokamak plasma is mainly produced by micro-scale drift-type turbulence, which is driven by the gradients of temperature or density. Characteristic quantities, which determine the regimes are the normalized (logarithmic) gradients:

$$\frac{R}{L_n} = -R \frac{d}{dr} \log[n] = -R \frac{\nabla n}{n} \quad (3.48)$$

$$\frac{R}{L_T} = -R \frac{d}{dr} \log[T] = -R \frac{\nabla T}{T}, \quad (3.49)$$

where R is major radius. Fig.3.2 shows the regimes and the parameter space of their validity for case $T_e = T_i$.

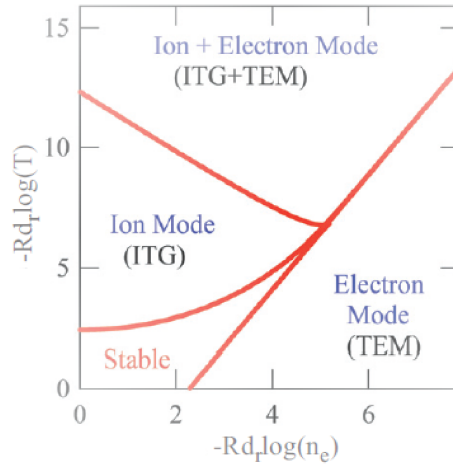


Figure 3.2: Stability diagram of ITG/TEM modes. Electron and ion temperatures are equal [71].

There are a number of transport models, which predict anomalous transport parameters based on ITG/TEM physics, e. g., Weiland [72], the gyro-Landau-fluid (GLF23) [73, 74] and trapped gyro-Landau-fluid (TGFLF) transport [75] models. These models have been tested against experiments and found to predict anomalous heat transport, the temperature, density profiles for main plasma inside of the H-mode pedestal for hybrid scenario [76, 77] for JET with C divertor. The NEO code is solving directly

drift-kinetic equation, including the self-consistent coupling of electrons and multiple ion species and the calculation of the first-order electrostatic potential via coupling with the Poisson equation [78].

Transport scaling is determined by the characteristic correlation length and time. When turbulent fluctuations are caused by low frequency drift waves with time scale $\tau_C \sim \omega_{i,e}$, and spatial scale $L_C \sim \varrho_{i,e}$ (ion or electron gyro-radius), the transport coefficient is described by the so-called gyro-Bohm scaling, $D \simeq (\varrho_{i,e}/L_T)T/eB$, where L_T is the temperature gradient scale length.

3.2.4 Transport in COREDIV code

Core transport in the COREDIV code is anomalous and the electron and ion energy fluxes are defined by the local transport model proposed in [79] which reproduces a prescribed energy confinement law. In particular, the anomalous transport heat conductivity is given by the expression:

$$\chi_e^{an} = C_E \frac{a^2}{\tau_E} F(r), \quad (3.50)$$

where $F(r)$ is the profile factor, a is minor plasma radius, C_E is adjusted iteratively to keep prescribed confinement. τ_E is the energy confinement time defined by the ELM-y H-mode scaling, which is assumed to be given by the IPB98(y,2) scaling law (see 1.9) for the divertor configuration.

For the profile factor $F(r)$, a simple dependence on the minor radius has been assumed.

$$F(r) = \left[0.25 + 0.75 \left(\frac{r}{a} \right)^4 \right] FSB(r), \quad (3.51)$$

where $FSB(r)$ is barrier function. In the COREDIV code, the transport coefficients in the pedestal region are modified to account for barrier formation: $FSB(r) = (1 - A) \exp\left[\left(\frac{r}{r_{ped}}\right)^{2EX}\right] + A$, with the parameter r_{ped} being the location of the pedestal top, A is the barrier depth reduction factor and the parameter EX defines the slope of the pedestal. In simulations, the pedestal is located at the 90-95% of the plasma radius a . In the Fig.3.3, the shape of the barrier is presented for different input parameters: barrier depth reduction factor and slope of the pedestal. It should be noted that for H-mode and hybrid scenario simulations, barrier depth reduction factor $A = 0.15$ is usually used which gives reasonable reproduction of the density and temperature profiles for majority of simulated pulses.

The ion density is given by the solution of the radial diffusion equation with diffusion coefficients $D_i^{an} = 0.1\chi_i^{an} = 0.1\chi_e^{an}$. Note however, that the solution of the diffusion equation is largely independent of the exact value of D_i^{an}/χ_i^{an} . Indeed, a change in D_i/χ_i causes a consistent change in the source term, since the average electron density is a COREDIV input.

In the code an anomalous pinch term is considered $V_i^{pinch} = C_p D_i^{an} \frac{r}{a^2}$, where C_p is the density peaking coefficient and $C_p = 0.1$ for main plasma ions has been chosen

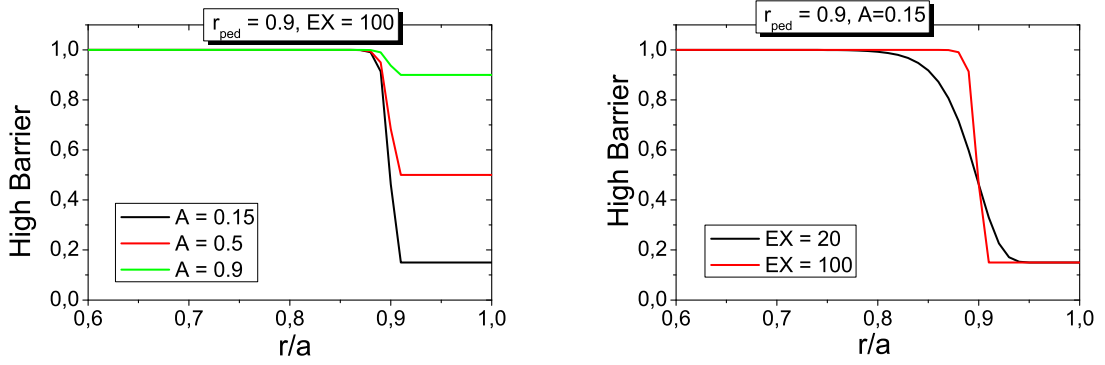


Figure 3.3: Shape on the barrier in the COREDIV code depend of the barrier depth(A) and parameter EX .

as a reference for H-mode scenario. The anomalous pinch for the impurity ions in the simulation is proportional to the pinch of the main plasma ion.

The transport model in COREDIV allows for two types of simulations. In one scenario, the parameter C_E is adjusted to keep the calculated confinement time obtained from the solution equal to the value defined by the scaling law. Second option is to fix C_E (and thus $\chi_{e,i}^{an}$) and therefore the confinement will be changed accordingly to the changes of input parameters, e.g. with changes to the seeding level. By increasing the radiation with impurity seeding, the net heating power decreases, thus when using the first option, the transport is reduced in order to keep the total plasma energy constant. In the case when the total plasma energy is set to remain constant with increasing the impurity seeding rate the net energy confinement time ($W_{th}/(P^{TOTAL} - R^{CORE})$, where W_{th} is thermal energy, P^{TOTAL} is total input power and R^{CORE} is total radiation power in the core) and the effective τ_p (effective particle residence time) increases during the impurity seeding scan since the power lost into radiation in the plasma core generally increases too.

In the practice ion transport depends of magnetic field, current, electron density, geometry of the tokamak and net power. Influence of these parameters on the impurity transport for JET ILW pulses will be presented in next Chapter.

SOL transport in the COREDIV code is classical along magnetic line and anomalous radially. The radial transport coefficient in the SOL region is set to be $D_{perp}^{SOL} = \chi_i^{an} = 0.5\chi_e^{an}$, where D_{perp}^{SOL} ranges typically $0.4 \div 1 \text{ m}^2\text{s}^{-1}$. Influence of the SOL transport on the impurity behaviour will be analysed and presented in Chapter 10.

Chapter 4

Diagnosctics in JET ILW

The model in COREDIV provides main plasma parameters (profiles of the density, temperatures, effective ion charge, impurity concentrations, impurity and total radiation, power and temperature at the plate), from a number of inputs like the auxiliary heating power, plasma current, toroidal magnetic field, elongation, major and minor radius, the average volume or line electron density, the confinement enhancement factor H_{98} and the separatrix density. The results from simulations need verification and comparison with the experimental results. The JET ILW tokamak is equipped with a large number of plasma diagnostics. For this reason, in this chapter, diagnostics in JET ILW that have particular relevance for my work are introduced. The most important diagnostic which provide the plasma parameters used in simulations of JET ILW discharges are as follow:

- *plasma electron density and temperature*

The High Resolution Thomson Scattering (HRTX) provides average values and profiles of the electron density and temperature in the plasma. This diagnostic is based on the radiation of particles in the plasma after interaction with an injected laser beam. The HRTS system on JET fires 20 light pulses per second into the JET plasma from a Q-switched Nd:YAG LASER, housed in the 'roof lab' above the JET machine. The laser light interacts with the electrons in a plasma via a process called Thomson scattering. As results of which, the electrons oscillate in the light's electric field and emit a photon of the same wavelength, as the incident light. In a hot plasma, the thermal motion of the electrons broadens the laser spectrum via the Doppler effect. If the electrons are in thermal equilibrium, the spectrum of the scattered light has a gaussian shape. The width of the gaussian provides information on the electron temperature. The HRTS diagnostic measures electron temperature and density in JET along a chord across the low-field side of the plasma, close to the horizontal mid-plane. When mapped to the magnetic mid-plane, the HRTS data typically runs from $R_{mid} = 3.0$ to 3.9 m. Currently HRTS provides 63 spatial data points per profile, with a 20 Hz repetition rate for the duration of a JET pulse. The system has a spatial resolution of ~ 1.6 cm in the core region and ~ 1 cm in the pedestal region. The experimental profiles taken from HRTX are compared with simulated electron density and temperature profiles.

- *plasma electron density and temperature on the divertor plate*

The temperature and density on the divertor plate is a very important parameter, which governs e.g the sputtering processes. In the JET ILW, Langmuir probes are used to measure the plasma electron density and temperature in front of divertor surfaces. They consist of up to three electrodes inserted into the plasma. A variable voltage can be applied to the electrodes, and the current measured. JET has over thirty fixed Langmuir probes on the inner and outer vertical target tiles, and on divertor. This diagnostic is called KY4D. The scheme of position onf the Langmuir probe in the divertor region is presented in Fig.4.1.

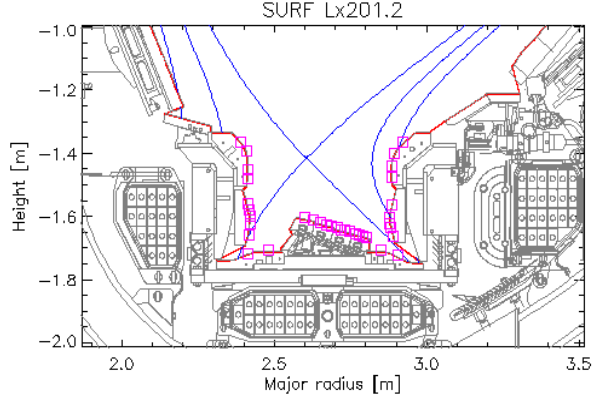


Figure 4.1: Positions of the KY4D Langmuir probes in the JET divertor.

The electron temperature and density on the divertor plate, which are calculated self-consistently in the code are compared with experimental data.

- *plasma radiation*

The total radiated power, as well, as the radiation emission profile of JET ILW discharges is determined from the bolometer diagnostic. Radiation represents a significant fraction of the power balance in tokamak. A bolometer measures the plasma radiation over a wide spectral range (from soft-X to the infrared). The JET bolometry system consist of two main-vessel bolometric cameras, called as KB5 with horizontal and vertical views of the plasma cross-section (24 chords for each camera) and three divertor bolometer cameras called KB3 with 12 lines-of-sight(LOS). The system of the lines-of-sight of the bolometer system, including main chamber and divertor viewing systems are presented in Fig. 4.2. The combination of KB3 and KB5 systems provides measurements with significantly improved spatial resolution, allowing the divertor and main chamber radiation fractions to be clearly resolved.

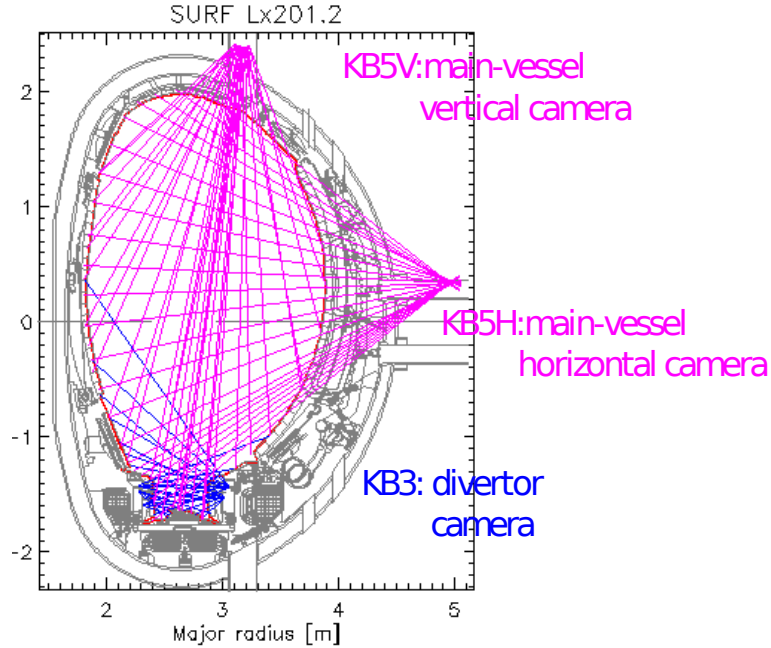


Figure 4.2: Lines-of-sight of the bolometer system, including main chamber and divertor viewing systems.

Obtained bolometric data are used for comparison of experimental and simulated profiles of the radiation as well as total, core and SOL radiations.

- *effective charge*

The effective charge Z_{EFF} is used to assess the impurity content of a fusion plasma. The study of the contamination of tokamak plasmas by impurities remains an important aspect of fusion research. It can be derived from measurements of bremsstrahlung intensity [80]. For visible radiation, the electron temperature is much higher than the energy of photons, which means that the intensity of bremsstrahlung radiation is in the first place proportional to the effective charge. As a result, the measurement of the emission of bremsstrahlung radiation in the visible wavelength range, line of sight, is a commonly used method to determine the Z_{EFF} . At JET ILW tokamak, the visible spectrum with one vertical and one horizontal line of sight are used to determine a line averaged value of the Z_{EFF} [81]. This diagnostic is locally called KS3. In order to avoid interference of the measured signal by visible light from other sources (e.g. reflection inside the plasma chamber), a narrow area of continuous spectrum around 5230 \AA [82] is usually selected. In this work, for comparison with experimental data, horizontal Z_{EFF} data is used.

- *impurity content and concentrations*

Spectroscopy diagnostics are used for identification of intrinsic and extrinsic plasma impurities, also for determination of its concentration in the plasma. Impurity concentrations can be obtained using various active or passive spectroscopic techniques, spectroscopy diagnostics with XUV, VUV, SXR and visible wavelength range, bremsstrahlung spectroscopy and Charge Exchange Recombination Spectroscopy (CERS). In practice, the

study of Z dependence impurity density are associated with the use of different diagnostics for different impurities.

A Princeton Instruments SPRED [83] survey spectrometer, known at JET as KT2 diagnostics registers VUV spectra in wavelength range of $110 \div 1100\text{\AA}$ with a spectral resolution of 5\AA . The LOS presented in Fig. 4.3, as a horizontal pink line is along vessel midplane, allowing it to view emission from the core and scrape-off layer of the plasma.

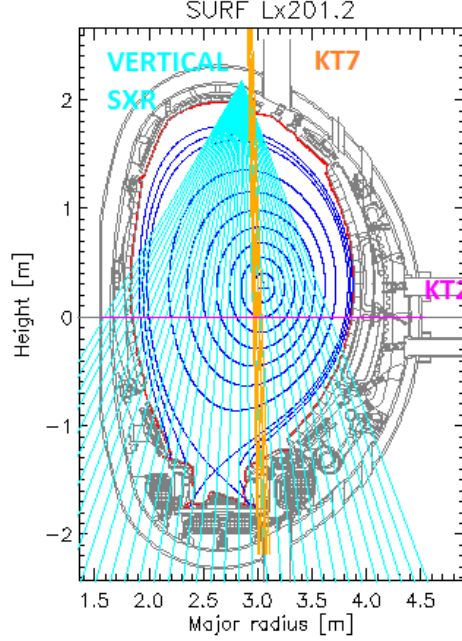


Figure 4.3: LOS of the SXR, XUV and VUV diagnostics at JET used for determining mid- and high-Z impurities concentration. The lines of sight of vertical SXR cameras (blue) as well as KT2 (pink) and KT7 (orange) VUV spectrometers with the magnetic equilibrium of JET pulse # 92398 at 7.5s.

- *Impurity density (concentration)*

Within the range of wavelengths observed by KT2 diagnostics there are intensive spectral lines of spectral origin in the spectrum by low-Z impurities like carbon(C) and oxygen (O), while the short-wavelength range by different mid-Z impurities like nickel (Ni), iron (Fe), copper (Cu), chromium (Cr), molybdenum (Mo) make this range particularly valuable from the point of view of diagnosing high temperature plasmas. After installation of the ILW at JET, which consists of a full tungsten (W) divertor and beryllium (Be) main chamber PFCs, the spectrum also contains intense W features [84].

Low Z impurity: He, C, Ne, Ar

The density of low Z impurities ranging from He to Ne is determined by charge exchange recombination spectroscopy (CXRS)[85]. CXRS process is generated by the interaction of neutral particles with the plasma. Additionally, CXRS system can be used to determine ion temperature from Doppler broadening of emission lines, plasma rotation from Doppler shift of spectral lines, and impurity ion densities from absolute line intensities across the whole minor radius. Detailed description of the diagnostic, its

calibration are presented in Ref.[85]. The spectral analysis of the plasma light collected by the two periscopes can be performed with five spectrometers.

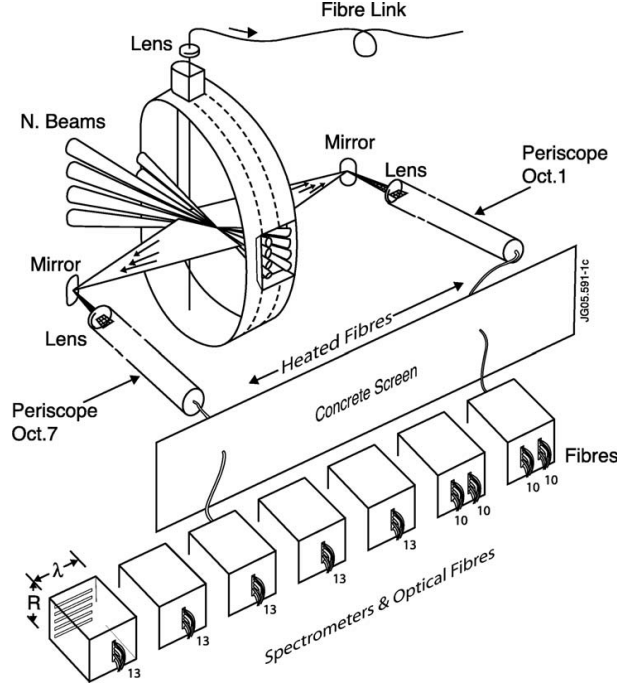


Figure 4.4: The new JET CXRS system [86].

The possible future DT operation of JET provides a unique opportunity to observe the direct production of helium ash and its transport. This diagnostic for possible future JET DT operation uses charge-exchange recombination spectroscopy(CXRS) in conjunction with the JET neutral heating beam to measure the helium density during DT operation at 20 radial locations (< 4 cm resolution) across the JET plasma via the 4686\AA , $n = 4 \div 3$ He^+ line, and an array of heated 1 mm quartz fibers (to prevent browning from neutrons). Utilizing the helium density profiles the He ash transport and removal can be evaluated [87]. This diagnostic is designed to complement the existing CXRS diagnostic system on JET, which has high resolution, but poor light collection efficiency. The geometrical arrangement of the heating neutral beams is shown in Fig.4.4, together with the CXRS lines of sight.

Middle Z impurity: Ni, Cu, Fe

A method was presented for determining the metal impurity density, Z_{EFF} and dilution in steady-state JET plasmas using passive VUV emission by KT2 in Ref. [88]. The method is based on the absolutely calibrated VUV transition intensity measurements, as well as Universal Transport Code (UTC) simulations. In order to reproduce the intensity of mid-Z lines, UTC uses a wide class of transport coefficients. For a specific set of the diffusion and convection velocity, the simulated line intensity is matched to the line intensity measured in the experiment. Then it is possible to establish a linear fit using the dependence of the ratio between the obtained impurity densities and the line density on local electron temperature. Such an approximately linear fit allows us to calculate the local mid-Z impurity density in the mid-radius plasma region. It should be noted, that the impurity concentrations of Ni are output parameters in

COREDIV simulations.

High Z impurity: W

In this work, the tungsten density is used for comparison with simulation results. Determining the W concentration is not an easy task because the W spectrum spans over a wide wavelength range (from visible to Soft X-ray(SXR)) with hundreds of spectral lines at similar wavelengths due to the high recombination rate. Study of W behavior in JET plasmas are realised with a diagnostics combining the soft X-ray (SXR) cameras and a vacuum-ultra-violet (VUV) Schwob-Fraenkel SOXMOS [89] spectrometer, called KT7 diagnostic at JET. The W concentration (density) is taken by two different diagnostics: KT7 and SXR cameras.

First is KT7, which looks down on to the JET divertor (see Fig. 4.3) and register spectra in wavelength range of $140 \div 440\text{\AA}$. A strong spectral feature of 5nm, where radiation of W-ions (W^{27+} to W^{35+}) is emitted is also called quasi - continuum. This particular kind of quasi-continuum, which occurs when the electron temperature lay in the range between 0.8 to 1.8 keV, is used for a quantitative determination of W concentration. This method is described in detail in Ref. [90]. The spectrometer provides W-concentrations that are valid only in a limited radial range, where the local T_e allows the emission. Poloidal asymmetries, especially in-out asymmetries, might lead to an underestimation of the W-concentration. However, spectroscopy provides a direct method to determine the W concentration independently of other radiators in the plasma.

The second approach is using the SXR cameras to determine the W concentrations. Since 2005 the SXR system consists of 3 cameras, two with vertical orientation (V, T) and one with horizontal (H). The vertical cameras, due to their favourable viewing geometry, were often used for characterisation of poloidal asymmetries. Due to a technical problem with camera T, the presented results only make use of camera V with 35 lines-of-sight, sa shown in in Fig. 4.2(blue color). By using camera V it was possible to determine the profiles of impurity concentration and the 2D tomographic reconstruction of W radiation in SXR range. The SXR camera measurements were de-convolved using the assumption that all Bremsstrahlung was emitted due to low-Z impurities which does not exhibit poloidal asymmetries, while the additional radiation was attributed to high-Z and mid-Z impurities showing poloidal asymmetries mostly attributed to mass-dependent centrifugal effects. By using camera V it was possible to determine the profiles of impurity concentration and the 2D tomographic reconstruction of W radiation in SXR range. The large number of lines of sight allows determining a 2D radiation profile and poloidal asymmetries. However, it is not unambiguous what species in the plasma are responsible for the radiation in the soft X-ray range. As a result we needed to apply correction factors to come to a consistent picture with total radiated power and spectrometer measurements. The heavy impurity proportions cannot be disentangled quantitatively at the moment. This would require a quantitative, spectroscopic evaluation of all contributors with their radial distribution.

Chapter 5

Numerical codes used in JET ILW simulation

The aim of the predictive transport modelling is qualitative predictions and extrapolations for various effect by running codes equipped with appropriately chosen models for transport and other relevantly phenomena. Presently, different numerical codes are used for simulations of the plasma performance in tokamaks. Traditionally, the plasma core and SOL have been treated separately in modelling with the justification, that the physics governing transport in these regions is different. The core transport is usually dominant by turbulent and anomalous transport. The reduced transport generated strong pressure gradient in the pedestal, which give rise to MHD instabilities thought to generate ELM. Transport in the SOL is dominated by very fast losses along the magnetic field lines and by atomic process, included iteration between plasma and neutral, plasma and wall(sputtering). It is possibility to segregate numerical code in the different group, depend which part on the plasma described:

- edge/SOL codes: EDGE2D, SOLPS, SOLEDGE-EIRENE, TECXY
- core: JETTO, ASTRA, ETS, TRANSP
- integrated modeling codes (core+edge/SOL): JINTRAC, COREDIV

This codes solved the Braginskij fluid equations, but are based on different numerical implementations, use different divertor geometries and neutrals models. This chapter describes the pros and cons of individual codes and their application to calculations of physical problems in discharges for the JET ILW tokamak. I will also show, what the COREDIV code looks like against them.

5.1 Edge/SOL codes group

The Edge/SOL codes are used to model only edge plasmas (until pedestal top) in the real vessel and magnetic geometry.

The **EDGE2D** code [91] is a 2D edge-plasma fluid model, relaxing self-consistently in time the continuity and parallel ion momentum equations for all ionic species, as

well as electron and ion internal energy equations. The code is coupled with Monte Carlo code EIRENE [92]. One of the first simulations [93] analysed the impact of beryllium/tungsten as plasma-facing components on plasma radiation, divertor power and particle fluxes, plasma and neutral conditions in the divertors has been assessed in JET for plasmas in L mode.

For JET ILW, a careful comparison between different sets of atomic physics processes used in EIRENE shows, that the detachment modelled by EDGE2D-EIRENE relies only on an increase of the particle sinks and not on a decrease of the ionization source [94]. The impact of the spatial neutral distribution on detachment has been analysed in greater detail for JET ILW unseeded L-mode discharges for (semi-) horizontal (HT) and vertical target (VT) configurations [95]. In this paper, the transport in EDGE2D was purely diffusive and fixed for all densities but cross-field drift were included. For H-mode plasmas in JET ILW, comparison with and without nitrogen seeding are prepared in Ref.[96, 97]. The simulations have already shown, that the divertor heat fluxes can be reduced with nitrogen injection, qualitatively consistent with experimental observations. The EDGE2D-EIRENE simulations of the impact of poloidal flux expansion on the radiative divertor performance in H-mode JET ILW shot for nitrogen seeding are prepared in Ref. [98], where non included effect on the drift. The influence of divertor geometry on H-mode power threshold and their explanation via target T_e profiles and the $\mathbf{E} \times \mathbf{B}$ shear in the near SOL triggered modeling with EDGE2D-EIRENE code but only for pure deuterium (D), or its isotopes: hydrogen (H) or tritium (T)[99].

The SOLEDGE-EIRINE is other edge code, which is used for simulation of the JET-ILW H-mode discharges [100]. The results are preliminary and the code was run without impurities in order to focus on primary differences in neutral recycling [101].

The SOLPS (Scrape-Off Layer Plasma Simulation) code package [102] is used for numerical simulations of the SOL and divertor plasma. The SOLPS package mainly consists of two coupled codes: B2.5 (fluid code that solves Braginskii-like equations for the ions and electrons) and EIRINE Monte-Carlo code for neutrals. Both codes are coupled via source terms of particle, momentum and energy. The SOLPS package also supplies a number of additional programs for the generation of a numerical grid from magnetic equilibria, and for post-processing and visualization. Self-consistent simulations including drift effects can shed light on the impact of drifts on the plasma evolution and on power exhaust by facilitating or inhibiting detachment. However, the analysis of the effect of drifts is very challenging, as the interaction with the plasma is complex and non-linear. Analyses of the JET ILW L mode discharges with SOLPS are presented in Ref.[103]. The SOLPS5.0 simulations corresponding to these experiments are performed with currents and cross-field drifts ($\mathbf{E} \times \mathbf{B}$, diamagnetic) activated [104]. The present studies consider only nitrogen impurity in the plasma solutions. In the absence of ELMs, W core contributions are low and the edge heating power is reduced by W radiation by less than 10%, which is within the uncertainty range of the measurements and, therefore, neglected in the modelling.

5.2 Core codes

The code **JETTO** [105] is first example for core codes for transport simulation in JET ILW, which has been developed by JET team. This is a one-and-a-half-dimensional transport code calculating the evolution of plasma parameters in a time dependent axis-symmetric MHD equilibrium configuration. A splitting technique gives a consistent solution of coupled equilibrium and transport equations. The plasma boundary is free and defined either by its contact with a limiter (wall) or by a separatrix or by the toroidal magnetic flux. The 1D transport equations (averaged over the magnetic surfaces) for the electron and ion densities and energies and for the rotational transform are written in terms of a coordinate related to the toroidal flux.

Transport codes as JETTO are used to predict temporal evolution of the density and temperature profiles. Usually a semi-empirical so-called Bohm/gyro-Bohm transport model for anomalous transport is used in simulations[106]. The neo-classical contributions to the transport coefficients are calculated by NCLASS [107]. Several external modules have been coupled to JETTO, for the power deposition due to NBI, ICHR and ECRH heating. For transport of the neutral particles there is a package called FRANTIC (Monte Carlo code)[108].

For the impurity transport simulation in JETTO, the SANCO code [109] is used. SANCO is a complete impurity transport code, which includes all the atomic physics processes (ionization, recombination, dominated by radiative recombination, and excitation) from the ADAS atomic database [110]. The continuity equations for the impurities are solved by SANCO which is started within JETTO at each time step before the JETTO matrix inversion to update the impurity radiation terms in the equations and to provide impurity densities and gradients for the transport models to be used in the next time step. SANCO uses the metric coefficients from JETTO, but solves its equations on a nonuniform grid in order to account for the fact that higher resolution is required towards the plasma boundary, where atomic processes are important. The evolution of each ionization state of the impurity species is calculated by taking into account ionization, recombination, charge exchange and other atomic processes. The JETTO/SANCO transport code can be used in both: predictive and interpretive mode. The analysis of the tungsten transport in JET H-mode plasmas in hybrid scenario with JETTO/Sanco are reported in Ref. [111].

The **ASTRA (Automated System of TRansport Analysis) code** [112] is characterised by a modular organisation allowing the use of numerous existing routines for analyses of transport processes. The transport model is then completed by adding neoclassical transport from NCLASS [107], GLF23 [73, 74] and the current conductivity from CQLP code[113]. Schematic diagram of integration of modules in ASTRA is shown in Fig. 5.1.

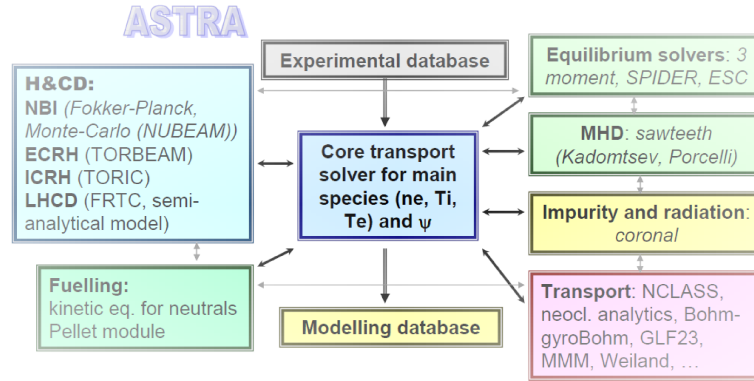


Figure 5.1: Schematic diagram of integration of modules in ASTRA.

Possible physics applications for ASTRA are: interpretative analysis, validation of transport models, scenario development, plasma control. The code has been used for testing of different transport models for heat and particles, but more for JET with C divertor. In the recent years a new version of the code has been developed: ASTRA-TGLF [114], where the ASTRA code is coupled with the free - boundary evolution code SPIDER and a quasi-linear turbulent transport model. This gives new possibilities to run the code. In particular, with the ASTRA-TGLF studies of the impact of high neon radiation on pedestal and divertor in JET ILW experiments [115] have been performed, but without tungsten, which is main radiator in core plasma. However, the different impurities are included in the analysis in a step-wise approach gradually increasing the analysis complexity in the search for the best match to all the available diagnostic measurements [116]. For the cases reported in [116] four elements (Be, Ne, Ni, W) were necessary to match simultaneously the observed soft x-ray emission, the W concentration measured by passive vacuum-ultra-violet spectroscopy, the line-of-sight integrated measurement of the effective charge Z_{EFF} , the observed poloidal asymmetry of the SXR emission and the line-of-sight integrals of the total radiation as measured by bolometry. Beryllium is taken as a constant background originating from the main chamber walls. Neon is left free to evolve in time to match the measured effective charge. Tungsten is calculated directly from the observed SXR emission subtracting the contributions from all other radiating elements. The inclusion of nickel is necessary to obtain a satisfactory match with the total radiated power as measured by the bolometer and is modelled from the initial estimate of the W density using theory-driven assumptions.

The TRANSP code[117] is time dependent transport codes for the analysis and the modelling of transport of magnetically confined plasmas. For JET ILW, it is used in predictive or interpretative simulations. In the predictive approach, the diffusivity terms are calculated self-consistently with kinetic profiles evolving in time and following a given transport model. Sources and sinks must be provided. This approach is used to validate transport models. In the interpretative way, the transport coefficients are computed using the experimental profiles as input. In TRANSP the impurity charge states are given only in coronal equilibrium. TRANSP contains modules to calculate profiles of heating and current drive sources. In Ref. [118] comparative analysis of

core heat transport of JET high density H-mode plasmas in carbon wall and ITER-like wall are presented. In this simulation, the impurity density profile is calculated to be proportional to the electron density assuming a uniform Z_{EFF} . In the TRANSP simulations only one impurity is used.

The European Transport Solver (ETS) [119] is a 1-D core transport code that is being developed by the members of Integrated Modelling Project (IMP3) (responsible for Transport Code and Discharge Evolution) of the EFDA Task Force on Integrated Tokamak Modelling (ITM). The approach taken by the ITM is to couple codes so that the only exchange is via well-specified data structures (Consistent Physical Objects (CPOs)), with the aim of having the workflow managed by Kepler [Online available: <https://kepler-project.org/>], a scientific workflow engine. The ITM has defined a number of standard objects which are used to describe a subset of the plasma state [120]. Each of these is supposed to be internally consistent and to be derived from a single source. A schematic design of the workflow is shown in Fig 5.2. Each box represents a set of modules that treat the same physics problem with various degrees of sophistication.

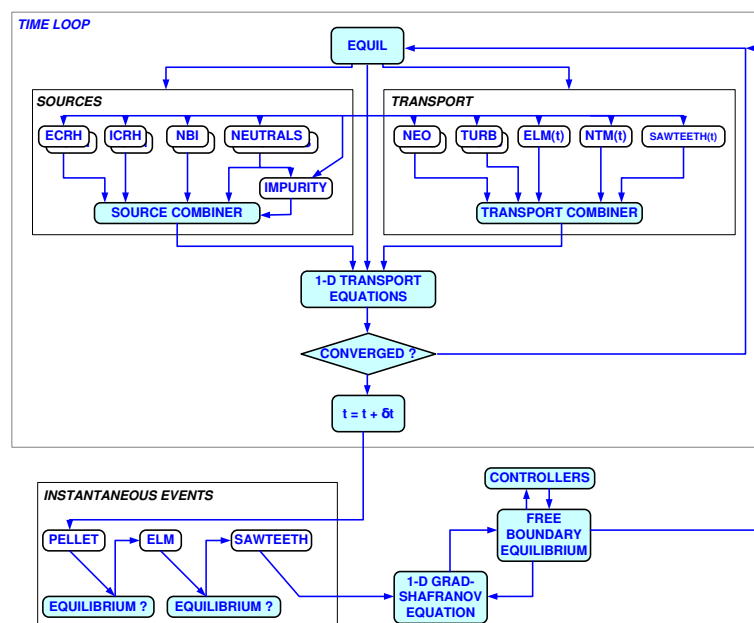


Figure 5.2: European Transport Solver: a schema of the workflow [121].

Note, that ETS modules for impurities (based on the impurity solver in the CORE-DIV code) and for cold and thermal neutrals have been developed by the author of this thesis. Density sources for each ionization state include ionization, recombination and charge-exchange, where rate coefficients of the relevant processes are obtained from the ADAS database using generic interfaces developed by the ITM-TF. The impurity solver used within the ETS was benchmarked against the SANCO impurity code, installed as a part of the JET analysis suite of codes, for conditions of a low confinement mode discharge #71827 in JET. Parabolic profiles for density and temperature of the main ions and the initial equilibrium provided by the EFIT equilibrium reconstruction code were introduced into both codes. Boundary conditions for individual impurity

ionization states were given by the total impurity concentration at the last closed magnetic surface, assuming a coronal distribution. Comparison between SANCO and ETS impurity solver has been done for Be, C, Ni and W.

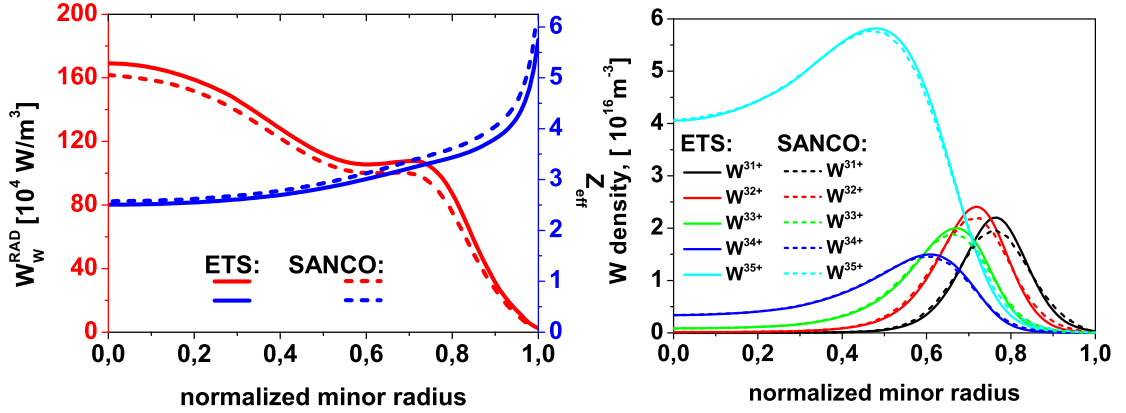


Figure 5.3: Benchmarking of ETS impurity solver with SANCO code for conditions of JET tokamak assuming parabolic plasma profiles.

Figure 5.3 compares steady state profiles of tungsten ionization states $W^{31+} \div W^{35+}$ dominating the radiative losses under considered conditions, radiative power density and ion effective ion charge, obtained with ETS and with SANCO after 1s of time evolution. The obtained total power radiated inside the separatrix is nearly the same in both simulations. The small discrepancy in profiles of impurity concentration and radiated power density can be explained by a 3% difference in the volume obtained from equilibrium solvers used in the compared codes.

First physics application with the European Transport Simulator for JET ILW discharges deal with analysis of the impurity transport in L-mode scenario and are presented in [121].

5.3 Integrated codes

The COCONUT [122] is a coupling between the 1.5D core transport code JETTO and the edge transport code EDGE2D. Typically, the boundary between the simulation domains of both codes is at the separatrix. EDGE2D passes the heat and particle fluxes across the separatrix as boundary condition for JETTO. The JETTO passes plasma parameters as boundary conditions for EDGE2D. In this way both codes are provided with self-consistent boundary conditions. The MHD stability calculation have been carried out using two codes called HELENA [123] and MISHKA-1 [124].

The JINTRAC integrated code [125] is employing the 2D EDGE2D-EIRENE plasma-edge code package which is coupled self-consistently to the 1.5D JETTO-SANCO core plasma code [105, 109]. In JINTRAC radial heat and particle fluxes (plasma and neutrals) are exchanged dynamically at a common boundary (i.e. the separatrix) and redistributed in poloidal direction [122]. The setup of the time-dependent JINTRAC integrated code model for a typical JET-ILW H-mode discharge including ELM dynamics is described in detail in Ref.[126]. The tungsten erosion flux in the

inter- and intra-ELM phase precluding self-sputtering was derived from the Eckstein formula for physical sputtering [35] taking into account the modelled time-dependent target electron temperature, bulk particle and impurity flux profiles towards the targets as well as the impact angle. In this paper, the tungsten transport into the confined region to estimate the core W concentration was not analysed with JINTRAC. However, in a post-processing way the JINTRAC data in terms of 2D plasma distributions and target fluxes were fed into DIVIMP Monte Carlo code to assess the W transport kinetically and to include the effect of prompt W- re-deposition.

Schematic diagram of integration of codes in JINTRAC is shown Fig. 5.4.

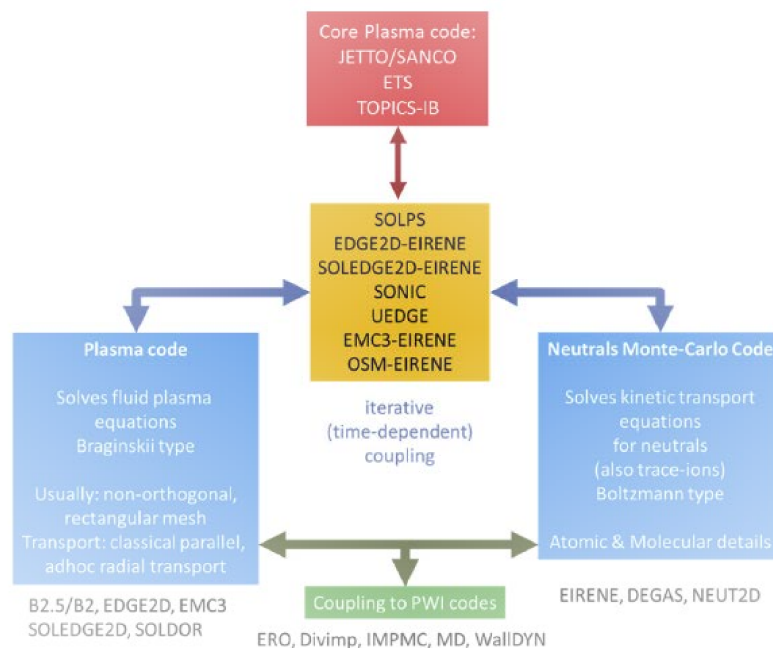


Figure 5.4: Schematic diagram of integration of codes in JINTRAC [127].

The JINTRAC core+edge+SOL simulations have been carried out for the late stationary H-mode phase $t = 11 \div 12$ s in JET ILW discharges #90223 and #90224 are presented in Ref. [128], whereas the simulation of first nitrogen seeding experiments in JET with the ITER-like Wall is presented in Ref. [129].

The COREDIV code solves self-consistently radial 1D energy and particle transport of plasma and impurities in the core region and 2D multi-fluid transport in the SOL (see Chapter 3.1.1). Since the model is relatively complex, and has been already presented elsewhere [130, 131] I will concentrate here only on the most important aspects of the model.

Core region In the core, the 1D radial transport equations for bulk ions, for each ionization state of impurity ions and for the electron and common ion temperature are solved. In the code, is no equilibrium model and the metric coefficients are calculated under the assumption that the magnetic configuration is defined only by the elongation parameter $k(r) = [k(a) - 1](r/a)^{0.25} + 1$, where a is the plasma radius. Densities of main plasma ions and impurity ions are given by the solution of the above radial diffusion equations with diffusion coefficients (see Chapter 3.2.4). It should be noted

that the assumptions related to the profile of the transport coefficients are of secondary importance as long as the transport is such to keep the defined H_{98} factor, which is an input parameter in our simulations. Electron density is calculated from the quasi-neutrality condition, whereas the ambipolarity condition defines the electron particle flux Γ_e .

The energy losses are determined by bremsstrahlung, synchrotron radiation, line radiation and ionization losses. With respect to the energy sources, alpha heating is calculated self-consistently with the plasma dynamics, whereas for auxiliary heating, a parabolic-like deposition profile centred at the magnetic axis is assumed. The equation for the poloidal magnetic field has been neglected and thus the current distribution is assumed to be given in our approach.

The source term takes into account the attenuation of the neutral density due to ionization processes: $S_i(r) = S_{i0} \exp(-\frac{a-r}{\lambda_{ion}})$, where λ_{ion} is the penetration length of the neutrals, calculated self-consistently. The source intensity S_{i0} is determined by the internal iteration procedure in such a way that the average electron density $\langle n_e \rangle$ obtained from the neutrality condition is fixed (input parameter).

SOL plasma In the SOL, the 2D boundary layer code EPIT is used, which is primarily based on Braginski-like equations for the main plasma and on rate equations for each ionization state of each impurity species. For the sake of simplicity, the classical cross-field drifts are not included in the model. Since the SOL model is fully described elsewhere, only the main points are briefly discussed in the following. For every ion species the continuity, the parallel momentum and two energy equations (for T_e and common ion temperature T_i) are solved. The transport along field lines is assumed to be classical and transport coefficients follow from the 21-moment Grad approximation [65, 132]. The radial transport is anomalous with prescribed radial transport coefficients of the order of Bohm diffusion. Equations of different fluids are coupled by electrostatic, friction and thermal forces as well as by atomic processes such as collisional ionization, recombination excitation and charge exchange. An analytical description of the neutrals is employed based on a simple diffusive model [133], in order to avoid time-consuming Monte Carlo calculations. Such a neutral model has been successfully used for a number of simulations of the boundary plasma in limiter tokamaks such as TEXTOR [133, 134], FTU [135] and Tore-Supra [136], proving to be able to describe in a reasonable way experimental situations.

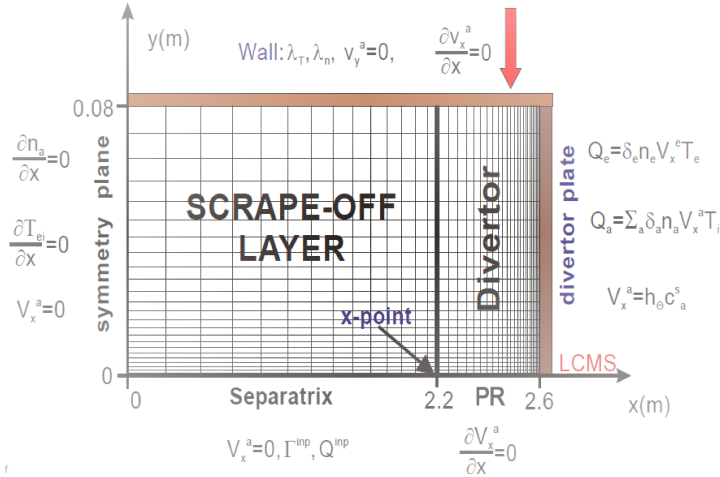


Figure 5.5: Scrape off layer in COREDIV code.

It takes into account the plasma (deuterium and seeded impurities) recycling in the divertor as well as the sputtering processes at the target plates including deuterium/tritium sputtering, self-sputtering and sputtering due to seeded impurities. The recycling coefficient is an external parameter and the energy losses due to interactions with hydrogenic atoms (line radiation, ionization and charge exchange) are accounted for in the model. A simple slab geometry (poloidal and radial directions) with classical parallel transport and anomalous radial transport ($D_i = \chi_i = 0.5\chi_e$) is used and the impurity fluxes and radiation losses caused by intrinsic and seeded impurity ions as well as by He ash are calculated self-consistently. Schematically the integration domain and the boundary conditions used in the EPIT code are shown in Fig 5.5. The standard sheath boundary conditions are imposed at the plates, whereas the boundary conditions are given by decay lengths at the wall. The parallel velocities and the gradients of densities and temperatures are assumed to be zero at the stagnation point.

The coupling between the core and the SOL is made by imposing continuity of energy and particle fluxes as well as of particle densities and temperatures at the separatrix. The computed fluxes from the core are used as boundary conditions for the SOL plasma. In turn, the values of temperatures and of densities calculated in the SOL are used as boundary conditions for the core module. In the core, the time-dependent transport equations are solved. For each time iteration in the core, several time steps ($10 \div 50$) are performed in the SOL to adjust the edge parameters.

In order to keep the prescribed plasma density at the separatrix (at stagnation point), the hydrogen recycling coefficient ($0 < R_H < 1$) was iterated accordingly. Note that the following definition of the recycling coefficient is used in our model: $R = 1 - \Gamma^{sep}/\Gamma^{PLATE}$, where Γ^{PLATE} is the total particle flux to the target and Γ^{sep} is the total flux crossing the separatrix. It should be underlined that the recycling coefficient in our approach includes effects related to the pumping efficiency (albedo) as well as the intensity of the puffing. For helium, the recycling was assumed to be two times smaller than for hydrogen ($R_{He} = 2R_H - 1$) in order to keep the helium recycling at a similar level with respect to hydrogen in all simulated cases (note that hydrogen recycling is not constant in our simulations).

In the case of seeded impurities (Ne, Ar, Kr) a constant value is assumed $R_{Ne,Ar,Kr} = 0.925$. Since argon and neon are recycling impurities, we expect that the recycling coefficient is high but unfortunately, the exact value of it is unknown. However, it is not so important in the calculations because the impurity concentration in the divertor region, and consequently in the core is determined by two factors: recycling coefficient and the rate of gas puff. Since the scan with the gas puff intensity is done in the simulations, the recycling coefficient is just a scaling factor. Different recycling would mean a different range of gas puff intensities. The only important point is that the recycling is large enough to keep impurities close to the target plates. The effect of the influence of the impurity recycling coefficient on plasma parameters was already investigated in our earlier works [137], showing that the exact value of the recycling coefficient is of secondary importance.

The following input parameters are given in COREDIV:

- plasma current I_p and toroidal magnetic field B_T
 - geometric quantities of vessel and plasma
 - power deposition of auxiliary heating (NBI, ICRH) to electrons and ions
 - experimental volume or line average electron density
 - H_{98} or CE
 - electron density of the separatrix or recycling coefficient
 - puff of the seeding impurity
-

Chapter 6

Numerical studies of impurity transport in JET ILW discharges without impurity seeding

Impurities released from interactions between plasma and material surfaces can lead to major effects on plasma behaviour in tokamaks. This is in particular true for JET experiments with the new ITER-like wall (ILW) configuration (ILW: Beryllium wall + W divertor), which shows that the plasma performance is strongly affected by tungsten impurity [138]. In view of possible realistic prediction for ITER plasma scenarios, it is necessary to develop validated numerical tools. For this aim, COREDIV code has been constructed, which self-consistently couples the plasma core with the plasma edge and the main plasma with impurities.

The first simulations with the COREDIV code for JET ILW configuration were done for low input power, L-mode discharges without impurity seeding. Numerical simulations of these discharges with COREDIV were quite challenging due to strong coupling edge-core in the relevant temperature range, the significant level of the Ohmic power (about one third of the total input power) and experimental uncertainties in the level of the radiation power.

6.1 Simulation for L-mode discharges

The basic aim of these simulations was the answer to the following question:

- *What is the influence of Be and W on plasma parameters?*

The results of investigations of the JET ILW L-mode discharges without impurity seeding were presented in [139]. Three well diagnosed discharges heated by ICRF at a power level of $P_{ICRH} = 3\text{MW}$ and with central line average density $n_e^{LINE} = 1.65$ (low), 2.3 (medium) and 2.8 (high) $\times 10^{19}\text{m}^{-3}$ were simulated, respectively. For ILW the main source of Be is located on the main chamber wall. A detailed description of the JET wall is therefore essential to derive quantitatively the Be fluxes, which, ultimately, are responsible for W fluxes from the divertor plates in the relevant temperature range of these pulses (electron temperature at the divertor plate, $T_e^{PLATE} < 50$

eV). Indeed, W sputtering due to deuterium impact is negligible below $60 \div 70$ eV. Here, the experimental divertor Be fluxes have been taken (derived from the absolutely calibrated Be II line intensity at $\lambda = 527$ nm, spatially integrated over the inner and outer divertor, and using the pertinent S/XB) as a COREDIV input, and then their values have been slightly adjusted to match with the total radiated power. Considering that for these pulses the Ohmic power ($P_{OHM} = 1.3 \div 1.4$ MW) is about one third of the total input power ($P_{aux}^{TOTAL} \sim 4.4$ MW) any change in the computed temperature and in Z_{EFF} leads to non-negligible changes in P_{aux}^{TOTAL} , which in turn leads to further changes in electron temperature profile (T_e), temperature on the plate (T_e^{PLATE}), W sputtering and so on.

In Fig. 6.1 the experimental and simulated density and temperature profiles in the plasma core are shown for the three discharges considered. The density profiles have

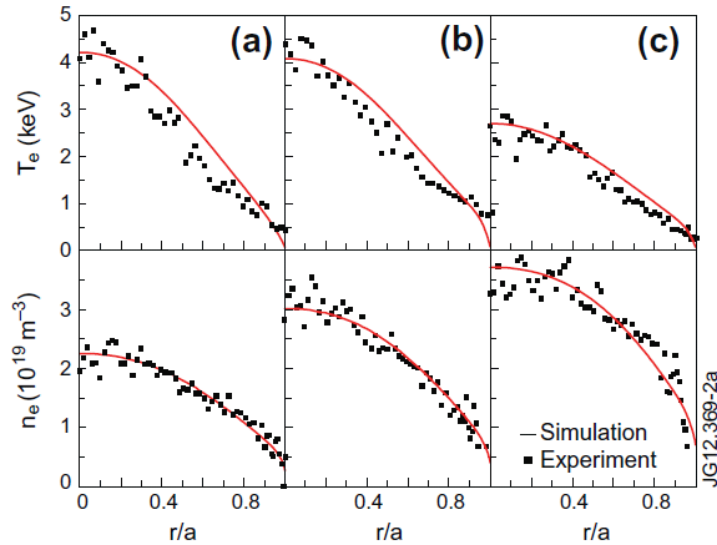


Figure 6.1: Electron temperature (top) and density (bottom) profiles from HRTS diagnostic and from COREDIV simulations as function of the normalized minor radius. From left to right: #80896, #80889 and #80893 at time $t = 19.5$ s [139].

been numerically derived by setting the electron density at the separatrix $n_e^{sep} = 7.2, 4.5$ and $2.9 \times 10^{18} \text{ m}^{-3}$ for the high, medium and low density discharges, respectively. These values are lower than the two values available from the Li-beam diagnostic: 8.5 and $4 \times 10^{18} \text{ m}^{-3}$ for the high and low density discharge, respectively. Independently of the level of uncertainty of the Li-beam measurements for these low density pulses and of the EFIT separatrix location, the choice of these input values for n_e^{sep} in COREDIV is the result of a compromise among different constrains. The input value of the separatrix density affects in COREDIV the density profile in the plasma core as well as the density at the target plate. Using the above mentioned input values for n_e^{sep} in COREDIV, the resulting simulated profiles in the core match relatively well with HRTS data (Fig. 6.1) and the resulting simulated density (and temperature) values at the plate are consistent with probe measurements at the outer strike point, see below. The discrepancy between simulation and measurement seen in the three core temperature profiles has a moderate impact on the radiation patterns since Be radiates mostly in the SOL and W mostly for T_e around about 2 keV. In fact, the core electron

density profiles are almost flat. In Fig. 6.2a the experimental Be fluxes and the input Be

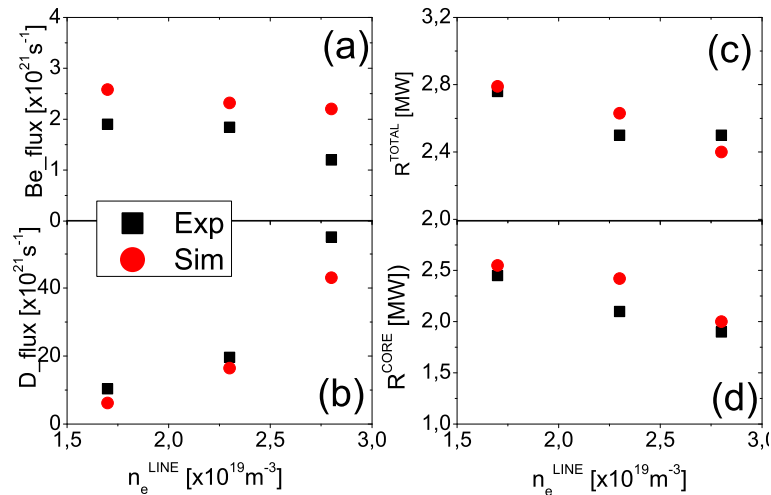


Figure 6.2: (a) Experimental and COREDIV input Be fluxes, (b) experimental and simulated D fluxes, (c) experimental and simulated total radiated power, and (d) power radiated inside the separatrix for the three discharges considered, labeled according to their line average density [139].

fluxes used in COREDIV are shown for the three discharges considered and in Fig. 6.2b the simulated and experimental D particle fluxes. While the simulated- experimental D particle fluxes match well, the COREDIV input Be fluxes, are systematically higher (up to about 80%) than the experimental ones, derived from the Be II line. Matching the COREDIV input Be fluxes with the experimental ones would lead to too low numerically simulated power radiated in the plasma core by W, see Fig. 6.2c and d. On the other hand, Be flux higher in COREDIV input than in experiment (while the simulated power radiated matches well with the experimental one) is consistent with the presence in the actual discharge of no negligible amount of other light impurities as C and O, which normally lead to further release of W from the divertor. In fact, in the present COREDIV simulations, only C is considered and the C flux is set to be at very low level: only about 10% of the Be flux.

The agreement of the measured and the simulated power radiated is correlated with the very good match between simulated and experimental W concentration in the core (C_W), see Fig. 6.3a. (It is worth noting that for these discharges the COREDIV calculated W self-sputtering is a significant fraction of the total W sputtering). Indeed, in the relevant range of temperature, only W ions are responsible for the power radiated in the plasma core. It has to be pointed out that the observed decrease of R_{TOTAL} with increasing density is not a general trend of the ILW plasmas, but apply only to these ICRF heated discharges and it is possibly correlated to specific radio-frequency effects, see below.

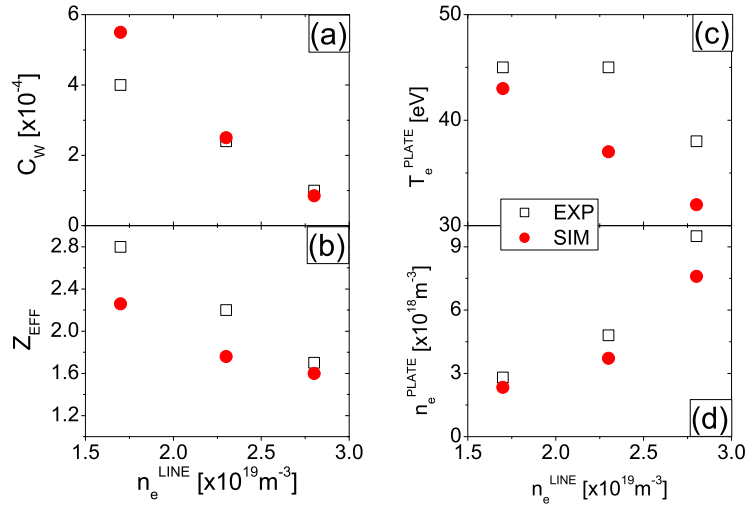


Figure 6.3: (a) Experimental and simulated W concentration (C_W), (b) experimental and simulated Z_{EFF} , (c) experimental electron temperature measured at the outer strike point and simulated with COREDIV, and (d) experimental electron density measured at the outer strike point and simulated with COREDIV for the three discharges considered, labeled according to their line average density.

Measurements of the absolute W fluxes are not available so far, but the ratios of the intensities (in a.u.) of the WI line at $\lambda = 400.9$ nm for the three pulses considered are quite compatible with the ratios of the COREDIV calculated W fluxes, which are in the range of a few 10^{19} particles/s. With respect to the absolute values, in Ref. [140] an estimate is given of the ratio C_W/C_{sat} for the considered pulses, which is compatible with the ratio (in the range 10^{-3}) of C_W/C_D in COREDIV simulations.

Indeed, the simulated Z_{EFF} is significantly lower (see 6.3,) than the experimental one for the two pulses at lower density. In the present contest only higher input fluxes of Be and/or of other light impurities would cause the increase of Z_{EFF} in COREDIV, but this would also lead to the increase in the W sputtering and, consequently, in the power radiated. At present, we do not have an explanation for this anomaly, which, however, on a speculative basis and partly in agreement with bolometric observations, would be consistent with radio-frequency specific effects. Indeed, the coupling of radio-frequency power with the plasma is generally rather weak at low electron density and this normally leads to interactions of the electric fields with the antennas limiters, causing release of Be. This Be flux enters directly the plasma core affecting significantly Z_{EFF} , but only marginally the power radiated. On the other hand it should be pointed out that Be transport might be different depending on the position where Be is released from (different screening, for example) while for these three pulses the same impurity transport is assumed in COREDIV.

The experimental electron temperature at the strike point, T_e^{PLATE} , measured with probes, is lower (up to about 40%) on the inner divertor than on the outer one, while the electron density, n_e^{PLATE} , is higher (up to a factor of 4) on the inner divertor. In Fig. 6.3c and d, the experimental T_e^{PLATE} and n_e^{PLATE} measured at the outer divertor are shown together with COREDIV results. It is difficult to compare COREDIV

results with experimental measurements on one of the two divertor legs, and this comparison has to be considered more from a qualitative point of view than quantitatively. However, the data in Fig. 6.3c and d shows that we are dealing with similar trends, thus contributing to the overall consistency among edge parameters.

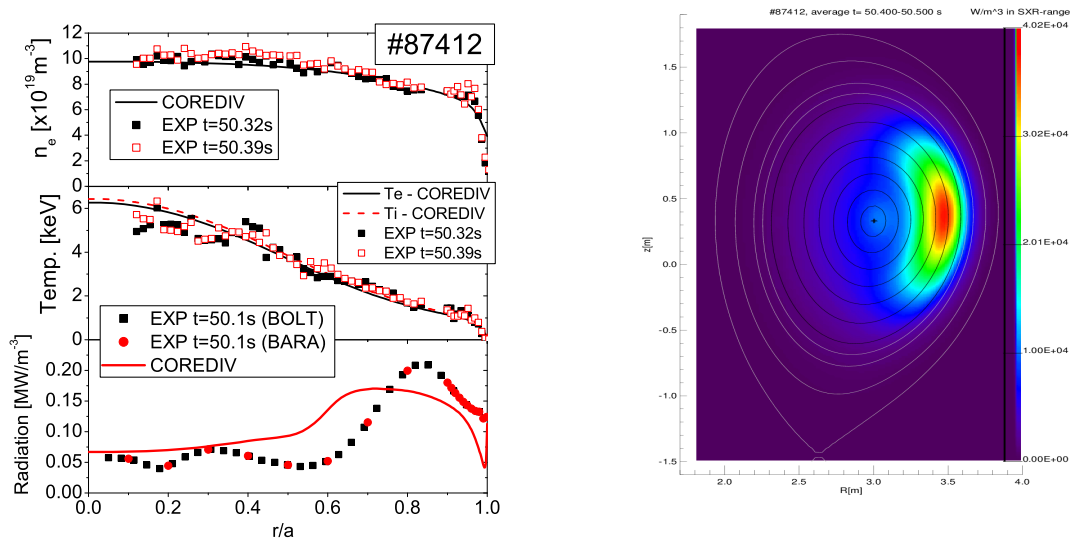


Figure 6.4: Calculated and experimental plasma profiles (left) for the JET ILW shot #87412 at $t = 10.3\text{s}$ [141]. Tomographic 2D reconstruction of the SXR radiated power density the JET ILW shot #87412 at $t = 10.3\text{ sec}$.(right).

6.2 Simulations for H-mode discharges

With COREDIV code many discharges in H-mode without impurity seeding were analysed. As example of the type I ELMy discharges, the reference shot # 87412 (3.5 MA/3.2T) with 31MW of additional heating power reported in Ref.[141] is discussed. This shot has been simulated with COREDIV assuming average plasma density $\langle n_e \rangle = 7.2 \times 10^{19} \text{ m}^{-3}$ and the experimental confinement factor $H_{98} = 0.8$. In the Fig. 6.4, experimental plasma profiles are compared to the code results. It can be seen that in addition to the density and temperature profiles, also the plasma radiation is well reproduced by COREDIV code. The agreement is satisfactory also for the global parameters like $Z_{EFF} = 1.14/1.12$, energy content $W_{DIA} = 8.35/8.7$ MJ or tungsten concentration $C_W = 7/5 \times 10^{-5}$ (the first number comes from simulations and the second one is from experiment).

6.3 Summary

The overall comparison of the simulations for not seeded L- and H- mode discharges with the experimental data is rather satisfactorily, both in the core and in the SOL. To this point it has to be stressed that the Be fluxes on the divertor target are not calculated self-consistently with the plasma parameters, but are given as

input in COREDIV, partly according to the experimental Be fluxes, determined by spectroscopic measurements, and partly to the level of the power radiated.

The results show that, in spite of the limitations related to the slab geometry of the SOL in COREDIV model and of those related to the self-consistent simulation of complex and strongly inter-dependent core-edge systems like JET plasmas with the ILW, the preliminary steps towards the integrated numerical modeling of JET plasmas with the ILW have been accomplished.

The main conclusion from simulations, which is in good agreement with experiment, is that main part of the radiation is coming from the core plasma and it is dominated by W radiation. Lower Z-impurity, as Be, C have influence on the Z_{EFF} for discharges without impurity seeding and do not contribute to radiation losses in the plasma core.

Chapter 7

Analysis of the influence of the source of the external (seeded) impurity

One of the main sources of the impurities in tokamak is the puff of the external impurity from the chamber wall or from the divertor region (impurity seeding). The main aim of adding extrinsic impurities to the species mix is to reduce power and energy loads on divertor targets. Within the context of divertor target material sputtering, this involves a balance between increasing the impurity concentration due to the seeding on the one hand and decreasing the divertor plasma temperature to reduce the impact energy of the incident particles at the other hand. Experiments with different impurity seeding: nitrogen, neon and argon have been performed in JET ILW configurations. Main questions addressed by the experiments are:

- *What is the effect of seeded impurity on total radiation losses?*
- *What is the effect of seeded impurity on the W production by sputtering?*

7.1 Influence of the nitrogen impurity puff

Historically, first experiment with seeding in the JET ILW were done with nitrogen puff. Analysis are presented for different experimental shots for two different plasma confinements: lower (L-mode discharges) and higher (H-mode and hybrid discharges).

L-mode discharges As a first step for analysing of the influence of the impurity seeding, simulations have been performed for a series of JET L-mode discharges (#82291, #82293-6, #82299) with different level of nitrogen puff. It is important, that these experimental discharges are characterised by the same electron average density $\langle n_e \rangle = 2.35 \times 10^{19} \text{m}^{-3}$, auxiliary NBI heating $P_{NBI} = 1.1 \text{MW}$, total heating (NBI and Ohmic heating) $P^{TOT} = 2.65 \text{MW}$, toroidal magnetic field $B_T = 2.5 \text{T}$ and plasma current $I = 2.5 \text{MA}$, but different impurity puff levels (nitrogen was seeded at different rates from 4×10^{21} to 1×10^{22} 1/s) in the divertor. For this reason, these shots are very nice for analyses of the influence of the impurity (nitrogen) puff on the global plasma parameters and especially on the W sputtering. The model in COREDIV provides, from

a number of inputs like the heating power, the average density and the confinement enhancement factor H_{98} , but the core temperature and density profiles, the effective ion charge Z_{EFF} , the radiated power, the W flux and concentration and the plasma parameters in the divertor are output data. In this simulations constant separatrix density has been assumed $n_e^{sep} = 1 \times 10^{19} \text{ m}^{-3}$ (controlled by iterative feedback on deuterium recycling coefficient). The present studies take the main plasma species and impurity recycling in the divertor as well as sputtering processes due to all ions (D, Be, N, W) at the target plate. It is assumed, that nitrogen is not a recycling impurity (with negligible value of the recycling coefficient: 0.25). The results of these analysis were published in Ref. [142].

In Fig. 7.1 experimental and simulated electron density and temperatures profiles are shown for two shots, with and without seeding.

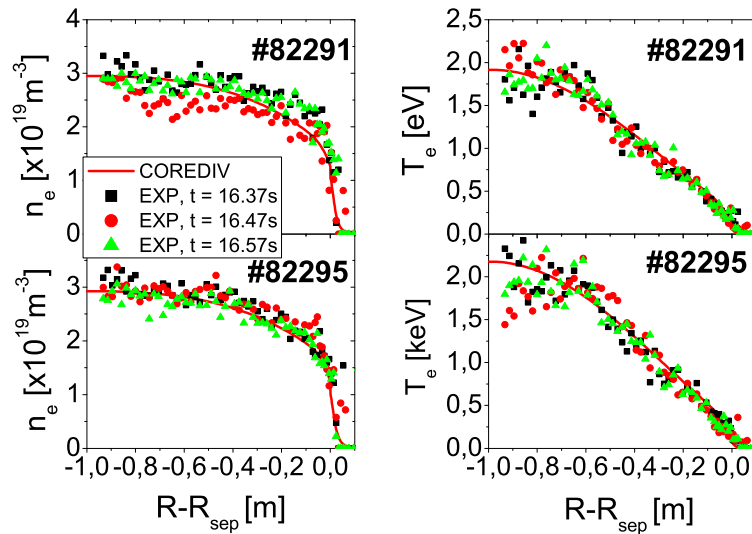


Figure 7.1: Electron density (left), electron (right) temperature profiles from HRTS diagnostic at different time for shot #82291 (top) and shot #82295 (bottom).

It can be seen, that radial profiles are nicely reproduced, when the transport coefficients are adapted, such as to provide a best possible fit of these profiles. The agreement between radiation levels versus nitrogen puff intensity is quite reasonable, as can be seen from Fig.7.2. The simulations show, that most of the radiation comes from the SOL region with much smaller contribution from the bulk plasma (factor 2) (note that the horizontal axis has been re-scaled to account for differences in nitrogen recycling models).

In Fig.7.3, the tungsten experimental concentrations (from SXR) are compared to the COREDIV predictions. It can be seen that in agreement with experiment, the tungsten production, after an initial increase (with puffing), is suppressed for sufficiently large nitrogen influx [140]. That illustrates a balance between increasing the impurity concentration due to the seeding on the one hand and decreasing the divertor plasma temperature to reduce the impact energy of the sputtering particles at the other hand.

The simulated W flux versus ion temperature at the divertor plate is shown in Fig.7.4, whereas Fig.7.5 presents W density flux versus electron divertor temperature

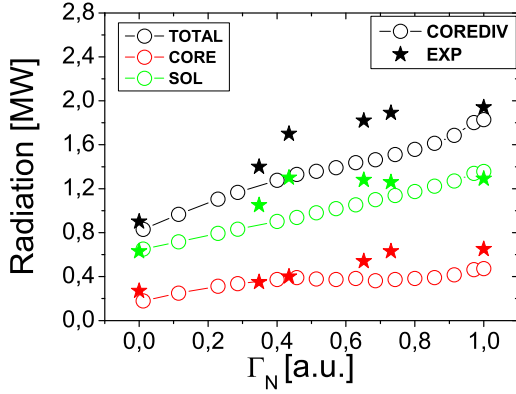


Figure 7.2: Total(black), core(red) and SOL(green) radiations versus nitrogen gas puff level.

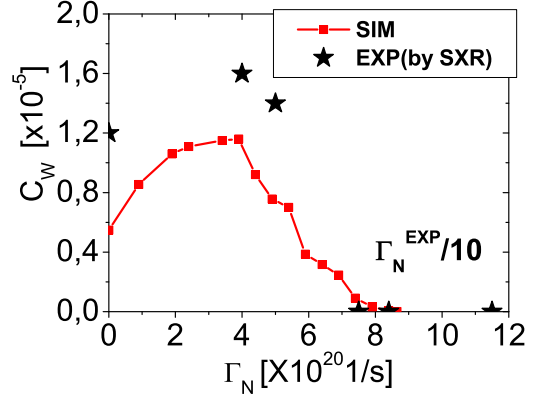


Figure 7.3: Simulated and experimental tungsten concentration versus nitrogen puff [140].

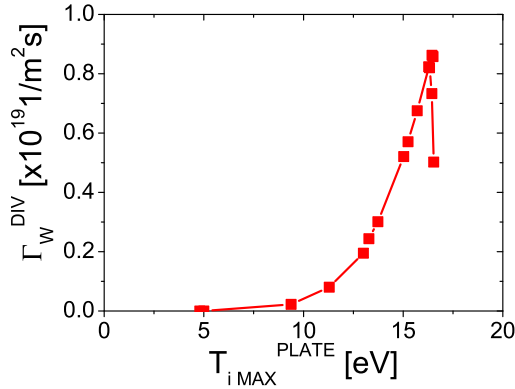


Figure 7.4: Simulated tungsten flux versus ion divertor temperature.

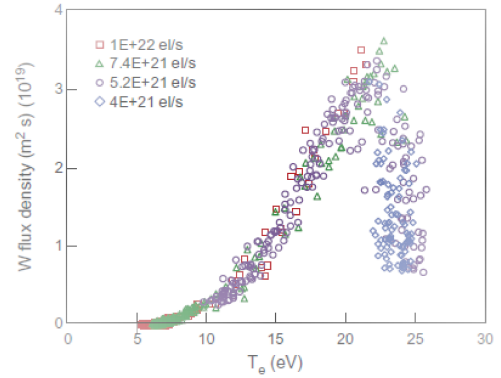


Figure 7.5: Experimental W density flux versus electron divertor temperature [140].

determined from the WI line intensity as a function of the plasma temperature in the nitrogen seeded experimental pulses (Ref. [140]). It should be noted, that the comparison between experimental and simulated results shows, that the behavior of the W flux versus divertor temperature is qualitatively the same.

H-mode and hybrid discharges. In this section, the JET H-mode and hybrid scenarios with nitrogen seeding are discussed. The all simulations have been performed with the same transport model and only the discharge input parameters like auxiliary heating P_{aux} , line average plasma density n_e^{LINE} , confinement factor H_{98} , nitrogen input flux Γ_N^{puff} were changed in the calculations. The separatrix density n_e^{sep} is an input parameter in our model and has been kept equal to $0.4 \div 0.5 n_e^{LINE}$ in the simulations, with the recycling coefficient adjusted accordingly. The input power has been split between electrons and ions, as 3/1. The results of the numerical simulations with COREDIV code are published in Ref. [143].

The code was run in a steady-state mode neglecting fast phenomena like e.g. ELM. This corresponds to the experimental results averaged over energy confinement time and seems to not impose strong limitations on the code-experiment comparison.

Main plasma parameters of simulations of two series of JET H-mode discharges with different level of auxiliary power are considered first and the comparison of global

7.1. INFLUENCE OF THE NITROGEN IMPURITY PUFF

parameters with experimental data is shown in the Table 7.1 for pulses #82031 and #82033 ($I=1.98$ MA, $B_T=2.18$ T) with $P_{aux} = 10.8$ MW whereas in the Table 7.2 we present pulses #83178-80 ($I=2.47$ MA, $B_T=2.7$ T) with $P_{aux} \sim 17$ MW. Here R^{CORE} is the core radiation (mostly by tungsten), R^{TOTAL} is the total radiation, n_e^{LINE} is line average plasma density (experimentally measurement by HRTS diagnostic) and c_W is the volume averaged tungsten concentration.

The beryllium flux (Γ_{Be}) from the wall has been assumed to be equal to $2 \times 10^{20} s^{-1}$ for the low power shots and to be proportional to the particle flux crossing the separatrix with the proportionality coefficient equal to 0.8 for all other shots in order to reproduce the low Z impurity level.

Table 7.1: The experimental and simulated global plasma parameters for shots #82031 and #82033.

JET Shot	P_{aux} [MW]	τ_E [sec]	Z_{EFF}	R^{CORE} [MW]	R^{TOTAL} [MW]	Γ_N^{puff} [$\times 10^{22}$ el/s]	n_e^{LINE} [$\times 10^{19}$ m $^{-3}$]	c_W $\times 10^{-5}$
#82031	10.8	0.31	1.36	3.10	5.4	1.1	6.34	1-2
SIM	11	0.30	1.26	2.3	5.51	1.05	6.8	1.36
#82033	10.8	0.34	1.26	2.1	5.0	1.6	7.1	1-2
SIM	11	0.30	1.26	2.46	5.88	1.05	7.34	1.19

Table 7.2: The experimental and simulated global plasma parameters for shots #83178-80.

JET Shot	P_{aux} [MW]	τ_E [sec]	Z_{EFF}	R^{CORE} [MW]	R^{TOTAL} [MW]	Γ_N^{puff} [$\times 10^{22}$ el/s]	n_e^{LINE} [$\times 10^{19}$ m $^{-3}$]	c_W $\times 10^{-5}$
#83178	16.7	0.32	1.46	3.54	6.31	3.03	7.23	~ 3.5
SIM	17	0.29	1.41	3.78	8.7	1.05	8.17	1.52
#83179	16.7	0.34	1.36	4.13	7.8	1.54	7.9	-
SIM	17	0.29	1.18	4.66	7.88	0.35	8.26	2.2
#83180	17	0.32	1.33	4.38	6.8	0.78	7.8	~ 2.1
SIM	17	0.32	1.12	3.14	6.71	0.35	8.26	1.38

For the low power shots (Table 7.1) the comparison with the experimental data is very good. For high power H-mode discharges (Table 7.2), there is some discrepancy when comparing all radiations and the Z_{EFF} values. Note also, that the experimental values of the nitrogen influx (Γ_N^{puff}) are usually larger than in simulations, since in latter case all the gas goes to the plasma which is not necessarily true for experimental situation (a significant part of the gas might be lost to the wall not reaching the plasma). The simulated Z_{EFF} is lower than the experimental value for two pulses #83179-83180, but simultaneously the total radiation is correct in contrast to the shot #83178, when Z_{EFF} is correct, but the total radiation is higher in the experiment, however the radiation in the core is similar to the experimental one.

Table 7.3: The experimental and simulated global plasma parameters for hybrid regime.

JET Shot	P_{aux} [MW]	τ_E [sec]	Z_{EFF}	R^{CORE} [MW]	R^{TOTAL} [MW]	$\Gamma_N^{pu\!ff}$ [$\times 10^{22}$ el/s]	n_e^{LINE} [$\times 10^{19}$ m $^{-3}$]	c_W $\times 10^{-5}$
#83568	25.7	0.16	2.51	~ 5	17	6.2	6.77	
SIM	24	0.17	2.5	11	17.25	2.8	6.79	9.01
#83570	20.5	0.17	3.07	5.1	15.7	4.9	6.46	
SIM	20.5	0.15	2.94	7.6	14.7	3.3	6.86	6.65

The situation is different for JET hybrid scenarios with high additional power and strong nitrogen seeding (shots #83568, #83570; $I=1.68$ MA, $B_T=1.975$ T). In this case, measured values of Z_{EFF} and total radiated power are very well reproduced by simulations, but there is some difference between simulations and experiment regarding power radiated in the core, as it can be seen from Table 7.3. We note, that W concentration for hybrid scenarios is much higher than for H-mode shots mostly due to the lower plasma density and stronger heating. That means that in spite of very strong seeding, the tungsten radiation remains important energy loss channel.

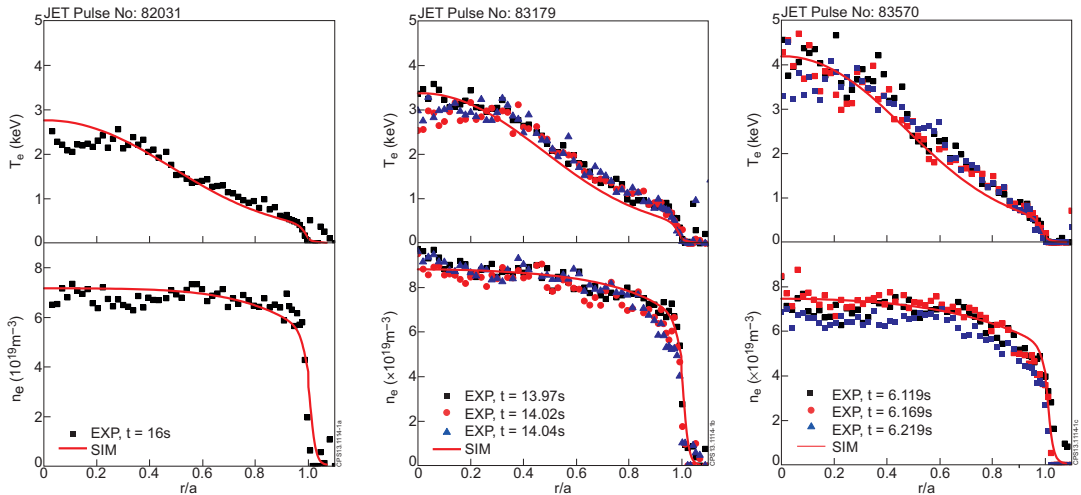


Figure 7.6: Electron temperature (top) and density (bottom) profiles from HRTS diagnostic at different time and from COREDIV simulations, as function of the normalized minor radius for shots #82031(left), #83179(middle) and #83570(right).

In the Fig.7.6, the experimental and simulated electron density and temperature profiles are shown for shots #82031, #83179 (H-mode) and #83570 (hybrid scenario). It can be seen, that radial profiles are nicely reproduced by the code. Note also, that in the considered shots tungsten accumulation is not observed, which is consistent with the assumption, that the impurity transport is dominated by anomalous contribution. This assumption is also consistent with the radiation distribution as it can be seen from Fig.7.7, where experimental and simulated radiation profiles in the plasma core are shown for this same shots. The calculated radiation profiles agree relatively well with the experimental data showing strong contribution of tungsten to the radiation losses in core. Radiation losses due to nitrogen are important only very close to the

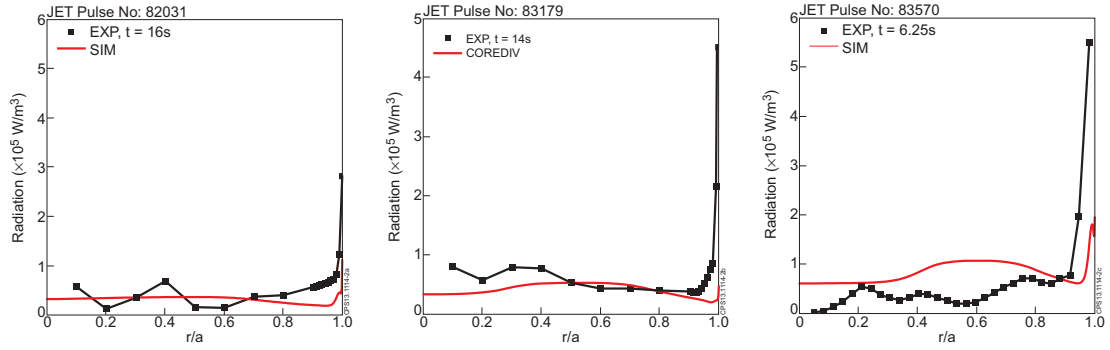


Figure 7.7: Profile of the radiation at $t = 16$ s for shot #82031(left), at $t = 14$ s for shot #83179(middle) and at $t = 6.25$ s for shot #83570(right).

separatrix.

It is important to note that in all considered shots tungsten radiation in the core is the dominant energy loss mechanism, which is good correlation with JET experimental results showing that in the JET ILW plasma performance is strongly affected by tungsten impurity.

7.2 Influence of the neon seeding

Historically, second impurity used as seeded impurity in JET ILW was neon (Ne). For illustration of the case with neon seeding, simulations for JET experiments M13-17: *maximum radiation fraction* are presented. These experiments were characterized by strong deuterium puff and neon seeding, which lead to strong peaked profile for density ($n_e(0)/n_e^{ped} \cong 1.6$). Experimental and simulated profiles for electron density and temperature are presented in Fig.7.8(a,b) together with the radiation profile Fig.7.8(c) for shot #85441, $t = 15$ s. The experimental profiles are nicely reproduced by simulations together with the global parameters: $R^{TOTAL} = 11.9$ MW, $R^{CORE} = 7.49$ MW, tungsten concentration: $c_W = 7.4 \times 10^{-5}$; $Z_{EFF} = 2.28$ in simulations and in experiment we have: $R^{TOTAL} = 12.6$ MW, $R^{CORE} = 7.3$ MW, $c_W = 6 \times 10^{-5}$; $Z_{EFF} = 2.14$, respectively.

Fig. 7.9 shows simulated radiation losses versus Z_{EFF} value for neon seeding together with experimental points for JET shots: #85438, #85439, #85441. It can be seen that the experimental points fit quite well into simulation curves.

Another experiment with neon seeding was performed in the ITER relevant high-triangularity, vertical-target configuration, at $I = 2.5$ MA and $B_T = 2.7$ T. The D puffing rate was maintained constant at 4.1×10^{22} el/s (leading to a volume average density, $\langle n_e \rangle$, in the range $8 - 8.7 \times 10^{19} \text{m}^{-3}$) and the auxiliary heating power was about 18 MW NBI + 4-5 MW ICRF heating. The neon seeding rate was increased pulse by pulse resulting in the increase of the total radiated power (R^{TOTAL}) in the range 9.5 to 13 MW. Numerical simulation of these five discharges has been made also in view of extrapolating a scaling for neon seeding, based on experimental JET data. Results of these simulations are presented in Ref. [145]. Since these simulations aimed at producing a scaling based on experiments, also to predict global trends, the

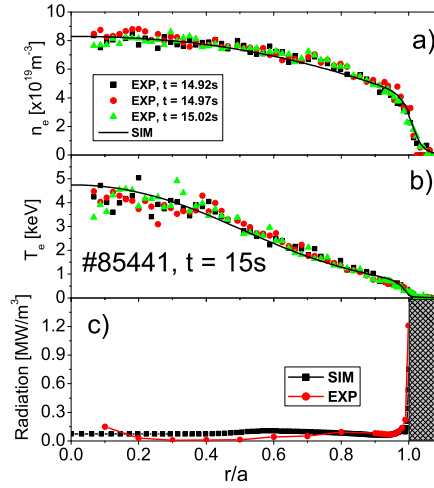


Figure 7.8: Experimental electron density (a) and electron temperature (b) profiles from HRTS diagnostic at different times and from COREDIV simulations, as function of the normalized minor radius for the JET shot #85441. For the same shot radiation profiles in the core from experiment and from simulations (c) [144].

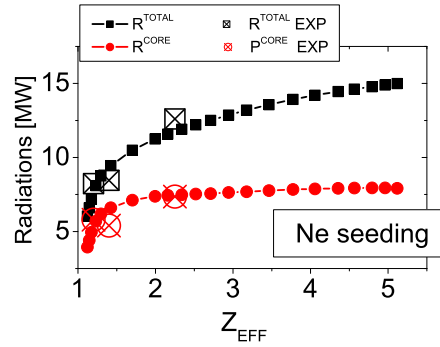


Figure 7.9: Simulated radiation losses versus Z_{EFF} value for neon seeding together with experimental points for JET shots: #85438, #85439, #85441.

COREDIV Ne seeding rate was increased up to $\Gamma_{Ne} = 2 \times 10^{21}$ el/s and added the case for $\Gamma_{Ne} = 0$ for two slightly different densities ($\langle n_e \rangle = 8.7$ and $8.0 \times 10^{19} \text{ m}^{-3}$), keeping $P_{TOTAL} = 23$ MW. All the input parameters, but Γ_{Ne} and radial diffusion in SOL, were maintained constant in these scans. On the basis of the numerical results shown in Figs. 7.10 and 7.11 the following considerations can be done.

The quick increase of total radiation R^{TOTAL} and of W concentration C_W together with the drop of R^{DIV}/R^{TOTAL} for Γ_{Ne} between 0 and 2×10^{21} el/s shows, that the main effect of Ne seeding at high T_e^{PLATE} is tungsten release (and core radiation) with marginal effect on the radiated power in the SOL. In parallel with the quick increase of R^{TOTAL} with increasing Γ_{Ne} at low Γ_{Ne} , the power to the plate drops also quickly. In contrast, at high Γ_{Ne} the rate of change of R^{TOTAL} with increasing Γ_{Ne} is marginal as is that of the power to the plate. Therefore, since with increasing Γ_{Ne} also Z_{EFF} increases, see Fig. 7.11, a careful analysis of advantages (reduction of P_{PLATE}) and disadvantages (increase in Z_{EFF}) has to be done to establish the most appropriate neon seeding level in terms of the overall performances.

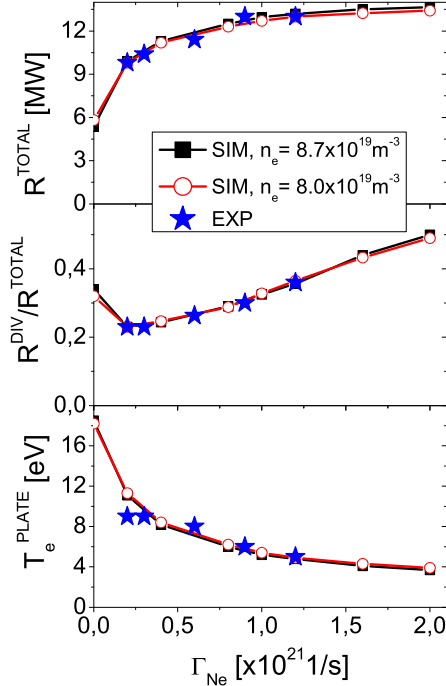


Figure 7.10: Experimental and CORE-DIV simulated (from top to bottom) total radiated power, ratio of radiated power in the divertor and the total one, electron temperature at the target plate as a function of the COREDIV Ne seeding rate.

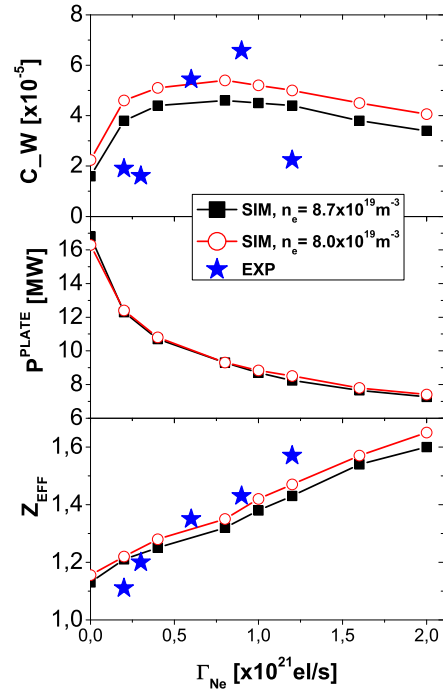


Figure 7.11: Experimental and CORE-DIV simulated (from top to bottom) W concentration, power to the target plate and Z_{EFF} as a function of the COREDIV Ne seeding rate.

Apart from the obvious difference in recycling behaviour, the basic trends of nitrogen seeding (presented above) regarding radiation and contamination have been found to be rather similar to those of neon, both in experiments and in simulations, as expected, considering the little difference in the atomic number of N and Ne.

Within the uncertainties of the presented in this section simulations, caused mainly by the simplified neutral model and by the absence of ELM modelling, the main experimental trends of Ne seeded discharges in JET with the ILW have been numerically reconstructed. Indeed, even though the actual dynamic of ELMs (W production, flushing out and transport) is bypassed by the assumptions of the steady-state W source and the W anomalous transport in the core, the simulated radiated power as well as the W concentration match well experimental data, showing the rollover in the W concentration with increasing Ne seeding level. The positive effect of Ne seeding on the power to the plate, which decreases significantly, is partly balanced by the increase in Z_{EFF} .

7.3 Influence of the sputtering coefficient

As already mentioned, in some cases it is difficult to fit by COREDIV simulations all the experimental global parameters like radiations and Z_{EFF} simultaneously. It can be attributed to the assumptions made in the model as well as to the unknowns related

to the experimental data. In particular, assumptions made to describe the impurity production at the plate might influence the results. They are related to the proper definition of the incident ions characteristics (energy, angle of incident), target surface properties (e.g. roughness) or the prompt reposition process.

Therefore the question is: *What is the role of the sputtering model used in the code and in particular the effect of prompt re-deposition on the results?*

Certain plasma parameters in the SOL, like separatrix density, deuterium puff or radial transport have influence on tungsten retention and by consequence on core parameters. In order to understand the reason for the differences between experimental and computation results, we have performed numerical studies to see which parameters have strong influence on the plasma parameters, in particular on the radiation level and its distribution.

It is believed that in case of tungsten, the prompt re-deposition might strongly reduce effective sputtering yield. Therefore, simulations have been performed to check sensitivity of the results on the total sputtering yield. For this aim, the sputtering yield due to all ions was reduced by factor: 0.3, 0.24, 0.18 and 0.06 in comparison to the standard model (first row in the table) and the results are presented in Table 7.4.

Table 7.4: The caption inside a table environment.

Sput. coeff.	C_W [10^{-5}]	Z_{EFF}	T_e^{PLATE} [eV]	R^{TOTAL} [MW]	R^{CORE} [MW]
1	1.96	1.14	5.62	5.63	2.92
0.3	1.72	1.13	5.95	5.3	2.62
0.24	1.49	1.11	6.13	5	2.33
0.18	1.22	1.11	6.27	4.64	1.98
0.06	0.5	1.11	7.25	3.66	1.05

It can be seen, that the reduction of the sputtering coefficient leads, as expected, to the smaller tungsten production and by consequence to the reduction of the core and total radiation. However, the effect is rather moderate, since the change of the sputtering yield by factor ~ 17 , reduces W concentration 4 times, core radiation by factor 3 and total radiation only by 1.5. The reason is such that the reduction of the sputtering yield is compensated by the increase of the plate temperature due to self-regulating mechanism coupling efficiently W production in the SOL with tungsten radiation in the core. In addition, sputtering yield has almost no influence on the effective charge and SOL radiation.

It should be noted, that prompt re-deposition is more important for the cases with lower plasma density and magnetic field (see Chapter 2.1.4). For this reason, to reproduce C_W for hybrid discharges prompt re-deposition is included. For example in the Ref.[146], a set of hybrid discharges have been studied, where Ne was injected from GIM9 in the divertor private flux region, and its rate was changed from pulse to pulse. At the same time, other parameters such as the plasma current, magnetic field, and

neutral beam injection (NBI) were kept constant at 1.4 MA, 1.9 T, and 16.3 MW, respectively. The series of the studied discharges consists of 5 pulses with increasing Ne seeding rate (#90336, #90337, #90339, #90279, and #90280), as well as reference one, without any injection of external impurity (#90287). What is also important, the hybrid discharges selected for this analysis were characterized by the magnetic configuration with the outer strike point close to the pump out valve (the so-called corner configuration). This configuration has some implications for the modeling of the W penetration into the plasma. The W atoms which enter the divertor plasma represent only a small fraction of the sputtered ones due to prompt re-deposition processes. Therefore, to reproduce lower radiation, the prompt re-deposition model was included in simulation. In these simulations, the W source is calculated from sputtering processes by main ions (D), impurity: seeded (Ne, Ni) and intrinsic (Be) and W self-sputtering. As it is presented in Fig. 7.12, experimental results concerning W are consistent with numerical modeling from COREDIV due to the fact that also simulations indicate a noticeable increase in W concentration for the plasma core and mid-radius region.

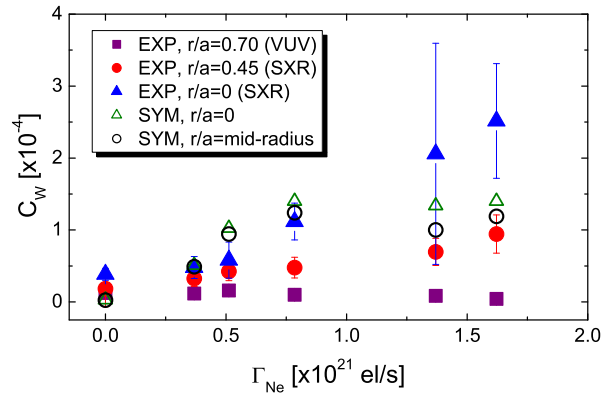


Figure 7.12: Comparison of W concentration obtained by using the SXR system and VUV spectrometer with the modeling one based on simulation with the COREDIV code for different plasma radii (especially in the plasma core and at mid-radius).

This comparison suggests that for higher Ne seeding rate, besides W also Mo is contributing to the SXR radiation. It is worth emphasizing that the Mo, as an interlayer in the divertor tiles, comes from the same region as W, what can explain their similar behavior during the presented experiment. A different trend is observed for mid-Z impurities such as Ni, Cu, and Fe. In the case of Ni, its production comes from structures within the vacuum vessel or is caused by contamination of the plasma facing components. For this reason, the effect of Ne seeding on Ni production should be significantly different compared to W and Mo release. As Fig. 7.13 shows, a decrease in the Ni intensity line with the increase in the Ne seeding rate was observed for the plasma region $r/a = 0.3-0.4$. This trend was confirmed by simulations, which rely on an assumption that the Ni source is by gas puff in midplane ($\Gamma_{Ni} = 1.5 \times 10^{19}$ 1/s), with recycling coefficient ($R_{Ni}^{REC} = 0.25$) and it remains unchanged for all discharges.

Additionally, total Ni radiation for two marginal discharges - characterized by the lowest (#90336) and the highest (#90280) amount of injected Ne, shown in Fig.7.14, as

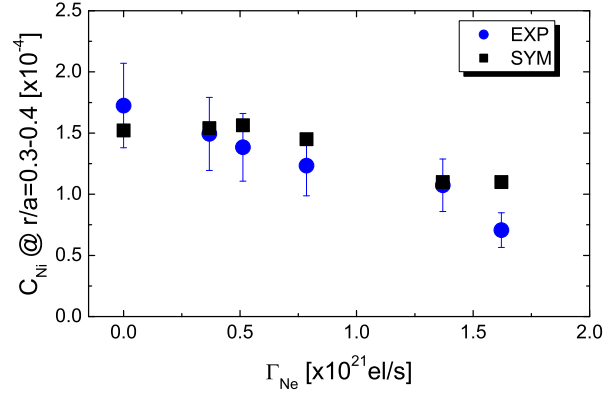


Figure 7.13: Comparison of Ni concentration obtained by using the VUV spectrometer with the modeling one based on simulation with the COREDIV code for the plasma region $r/a = 0.3-0.4$

a function of the plasma radius. As in the case of W (see Fig.7.12), here it is possible to observe higher radiation for the case of higher seeding. This is due to the fact that for the pulse #90280, we observed higher plasma density (n_e) and lower electron temperature (T_e) in comparison with #90336. In turn, these two parameters have a significant impact on the cooling factor rate, which in addition to plasma volume, Ne, and impurity density is proportional to the calculated Ni radiation. However, it is worth noticing that despite a similar trend for these two types of impurities (high and mid-Z), the total Ni radiation is an order of magnitude smaller than in the case of W.

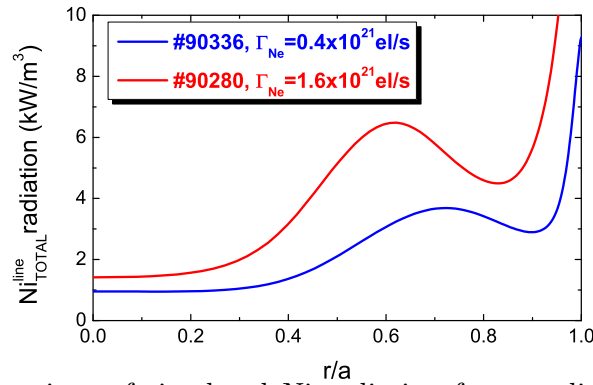


Figure 7.14: Comparison of simulated Ni radiation for two discharges with different Ne seeding rates.

7.4 Comparison of the different impurity seedings in JET ILW

The scrape-off layer (SOL) radiation of intrinsic impurities in tokamaks with tungsten (W) as target plate material, is strongly limited. That might lead to high heat fluxes to divertor and corresponding high target plate temperatures, with the consequence of increased W sputtering. However, the reduction of divertor target power

loads to an acceptable level is a critical issue for future tokamaks and fusion reactors. The radiative exhaust of energy by externally seeded impurities is considered presently as a promising way of spreading energy over a large wall area and therefore the effect of the impurity seeding on the plasma performance and heat load mitigation has to be understood. In particular, experiments have been performed to study the so called radiative scenarios, where the influence of the seeding impurity on the main plasma parameters is studied [147]. It has been found, that seeded impurities can affect the shape of density and temperature profiles, influence the L-H power threshold, the pedestal position and parameters as well as, the pedestal stability with its direct consequence on plasma performance.

The impact of impurity seeding on plasma transport and confinement is the major issue to be understood. In this regard, it should be pointed out that the Eq. 1.8 for the energy confinement does not take the radiated power into account. Already in present tungsten machines, this high-Z impurity might radiate strongly in the core and the inclusion of the radiation losses is therefore crucial.

In order to address that problem, some simulations have been performed aiming at comparison of the main plasma parameters (radiation, Z_{EFF} , impurity concentration ...) with experimental data for different scenarios: hybrid with nitrogen [143] and neon [146] seeding, L - mode with N seeding [142] and H-mode with N, and Ne seeding.

More systematic study of the influence of different seeding gasses: nitrogen (N), neon (Ne), argon (Ar) and krypton (Kr) on plasma parameters in JET ILW discharges has been presented in Ref.[148]. Since the energy balance in tokamaks with metallic walls depends strongly on the coupling between bulk and the SOL plasma integrated modelling approach has to be applied. From one side, the seeded impurities can, reduce the power to the SOL/divertor regions leading to reduction of the W influx, but from the other side, they can increase the W production due to enhanced sputtering. Therefore, the joined treatment of both regions is necessary, as long as the edge plasma is not separated from the bulk plasma.

The main questions to be answered are:

- *What impurity is the best and optimal?*
- *How much impurity ions can influence the plasma confinement?*

Simulations are performed for different seeding gasses (N, Ne, Ar and Kr) assuming different levels of impurity influx. As a reference scenario high power JET shot is chosen (#87194) with Ne seeding. Fig.7.15 shows the time traces of the main parameters of a neon seeded discharge where all the heating systems are employed.

The shot is characterized by the following main parameters: plasma current $I = 2.6$ MA, toroidal magnetic field $B_T = 2.5$ T, volume averaged density $\langle n_e \rangle_{VOL} = 6.2 \times 10^{19} \text{ m}^{-3}$ and line averaged $\langle n_e \rangle_{LINE} = 6.7 \times 10^{19} \text{ m}^{-3}$ electron density, separatrix density $n_s^{sep} = 3.0 \times 10^{19} \text{ m}^{-3}$, H-factor (IPB98_(y,2)) $H_{98} = 0.8$ and auxiliary heating $P_{aux} = 25\text{MW}$. It should be pointed out, that possible changes in confinement due to the level of the different gases and to the different radiation patterns are not accounted in this simulations.

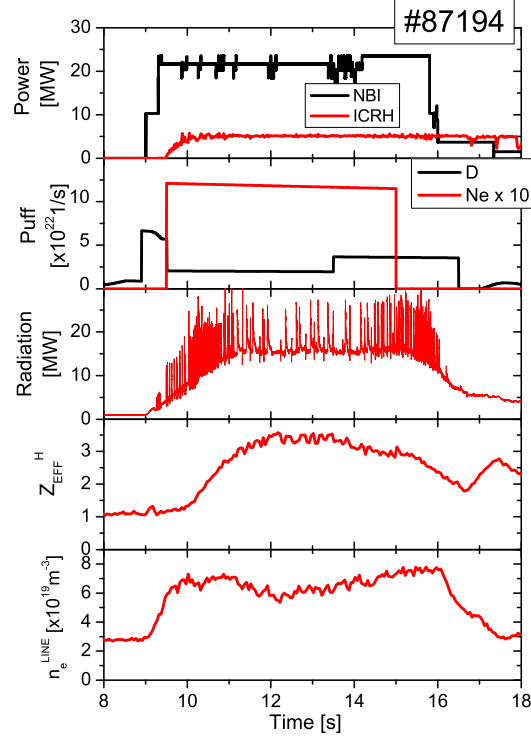


Figure 7.15: Time traces of main plasma parameters of discharge #87194.

The results of the transport analysis are displayed in Fig.7.16 and comparison between experimental and simulated profiles of electron density and electron and ion temperatures is shown.

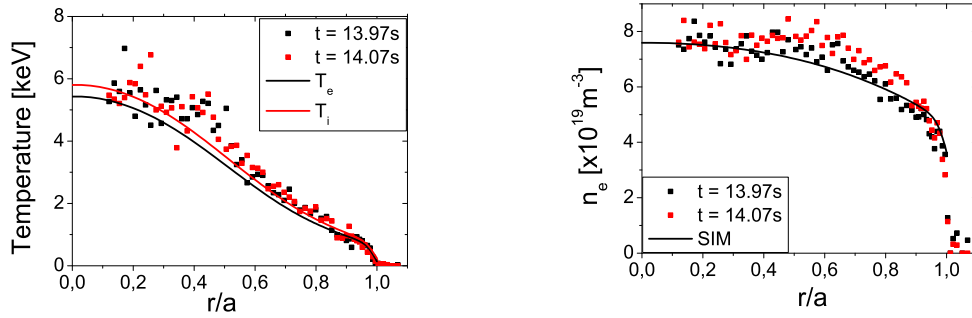


Figure 7.16: Temperatures (left) and density (right) profiles by simulation and experiment for shot 87194 at the time $t = 14s$.

All the simulations are done for the same input parameters, except seeded impurity type and its puffing rate. In case of N seeding, since nitrogen is not recycling impurity recycling coefficient $R_N^{REC} = 0.25$ is used, whereas for the noble gases Ne, Ar and Kr the coefficient is $R_{Ne,Ar,Kr}^{REC} = 0.925$. For the radial diffusion in the SOL, we use $D_{perp}^{SOL} = 0.5m^2/s$ whereas for the core transport only anomalous transport is considered neglecting contributions from the neoclassical transport.

Main plasma parameters versus impurity influx for different gasses (N, Ne, Ar and Kr) are presented in the Fig.7.17. In particular, we show radiation fraction (f_{RAD}), power to the SOL (P^{SOL}) and to the plate (P^{PLATE}), electron temperature at the

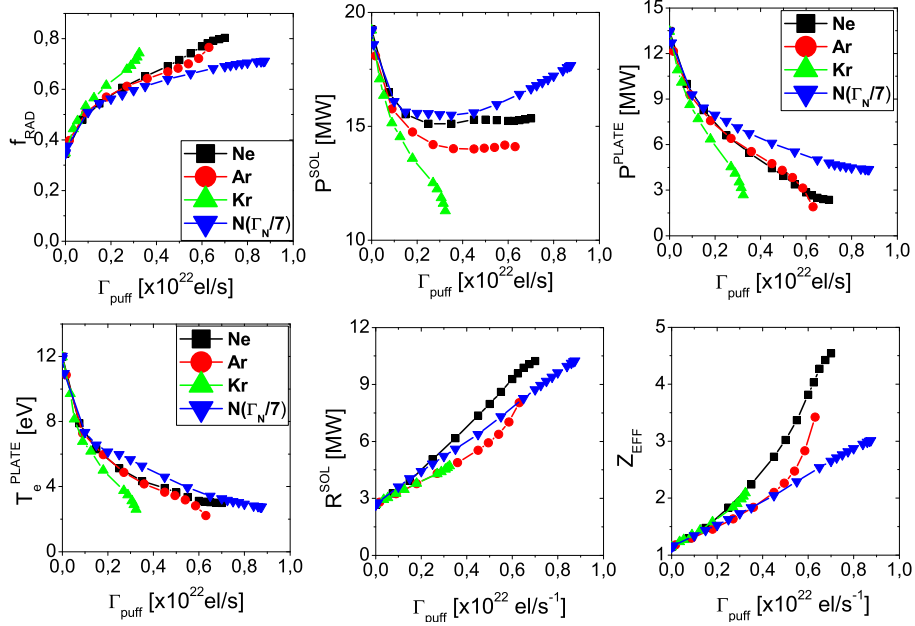


Figure 7.17: Main plasma parameters versus impurity influx for different gasses (N, Ne, Ar and Kr): radiation fraction (f_{RAD}), power to the SOL (P_{SOL}) and to plate (P_{PLATE}), electron temperature at the plate (T_e^{PLATE}), SOL radiation (R^{SOL}) and effective charge Z_{EFF} [148].

plate (T_e^{PLATE}), SOL radiation (R^{SOL}) and effective charge (Z_{EFF}). It should be noted, that the nitrogen puff level is reduced by factor 7 in the figures in order to have better comparison between all impurities. Simulations are performed from a negligible level of the seeding until the maximum value allowed by the numerical code stability and consequently, full detachment is not considered in the simulations.

The threshold power (P_{H-L}), calculated according to the Martins law [14] is found to be 9.5MW for the considered JET shot and it can be seen that there is no problem to stay in H-mode for all impurities and seeding levels. However, the power to the plate without impurity seeding (13.5MW) (Fig.7.17) would be relatively high (exceeding technological heat flux limits 10MW/m^2 (and assuming, that divertor plate surface is 1m^2) and impurity seeding is necessary to reduce the power to the target plates for the simulated discharge.

The achieved total radiation fractions are between 70% and 80%: 71% for N, 80% for Ne, 76.5% for Ar and 74.5% for Kr seeding, respectively. The radiation fraction for low Z impurities (N, Ne) goes to saturation with the increasing of the seeding rate. It has been found that for every gas at the maximum level of the seeding the power to the plate is reduced down to 2-5 MW and the electron temperature at the plate is about 2-3 eV, indicating semi-detached conditions in the divertor region. In case of Kr seeding, the reduction of the power to the plate is very sensitive to the seeding level. For puffing levels smaller than 0.3×10^{22} el/s, we observe similar values of $Z_{\text{EFF}} \approx 1.8 \div 2$ but for higher puffing rates there are significant differences in the Z_{EFF} values. The maximum Z_{EFF} is obtained for the Ne seeding, which is about 2 times higher than in case of Kr seeding.

SOL radiation increases almost linearly with the seeding level, and the largest

radiation is achieved for N and the smallest for Kr seeding, depending on the cooling rates of the impurity type. The behaviour of the power to the SOL as a function of the impurity puff rate depends on the impurity atomic number. For Kr, it always decreases with the increase of the seeding level, for Ne and Ar saturation is achieved, whereas for N seeding, increase of P^{SOL} is seen after initial reduction. Therefore, for nitrogen, large seeding levels are possible to work in H-mode.

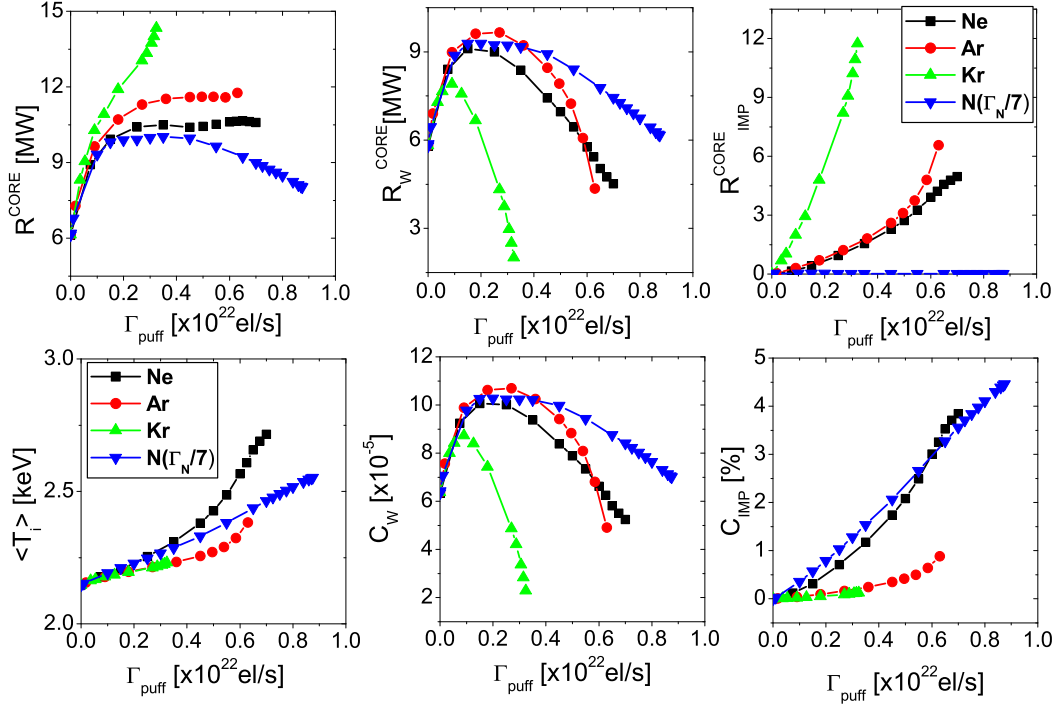


Figure 7.18: Main plasma parameters for different impurity puff: N, Ne, Ar and Kr level: total (R^{CORE}), W (R_W^{CORE}) and by seeding impurity (R_{IMP}^{CORE}) radiation in the core, average ion temperature ($\langle T_i \rangle$), W (C_W) and impurity (C_{IMP}) concentration.

In the Fig.7.18, I present total core radiation, W radiation in the core (R_W^{CORE}), radiation by seeding impurity (R_{IMP}^{CORE}), average ion temperature ($\langle T_i \rangle$), tungsten concentration (C_W) and seeded impurity concentration (C_{IMP}) versus impurity puffing level. The maximum seeded impurity radiation in the core is observed for Kr seeding, with the smallest for nitrogen, which is consistent with our expectations coming from corona equilibrium (see Fig. 2.9). For typical core temperatures ($T_e \gg 150$ eV), the radiation efficiency of Kr is about 1000 higher than for N.

Only for Kr seeding, the W radiation in the core might be fully replaced by Kr radiation whereas for other impurities the W radiation in the core remains a significant part of the total radiation losses. For low and medium Z impurities (N, Ne and Ar), tungsten radiation is a significant part of radiation losses and stays above 22-32% of the total energy losses, but for high Z impurity (Kr) it is reduced down to 10% of the total losses. Correspondingly, W concentration for N, Ne, Ar goes down to $5 \div 6 \times 10^{-5}$ level whereas only for Kr it is reduced to 2×10^{-5} . For all impurities, similar temperatures at the plate are achieved of about $2 \div 3$ eV, as can be seen in Fig.7.17 which corresponds to similar sputtering yield values. However, the total tungsten influx due to sputtering

processes is higher for low Z impurities, which is the effect of higher impurity flux to the target plates. At maximum seeding rate, the impurity concentrations are from 4% for Ne and N to 0.1% for Kr. It can be seen from Fig.7.18, that with the increase of the impurity puff level, the average ion temperature increases as the effect of plasma dilution by impurity ions.

The target power load can be mitigated by increasing the level of seeding. In the presented simulations, confinement was kept constant (the H_{98} factor (total energy) and the energy (and particle) transport coefficients (C_E) were changed depending on the seeding gas type and puff intensity. Indeed, depending on the specific JET-ILW experimental situation, in some cases the H_{98} factor decreases [149] with increasing the Ne seeding level, in others it remains nearly constant. The Fig.7.19 shows the changes of the parameter C_E versus impurity puffing.

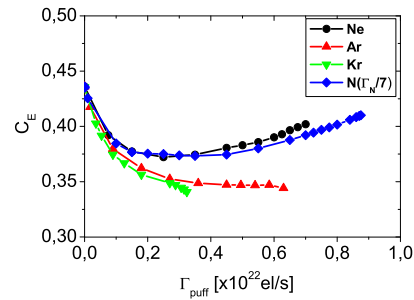


Figure 7.19: Transport coefficient C_E for different impurity puff: N, Ne, Ar and Kr level.

It is clearly seen that the coefficient C_E is reduced for all considered impurities at the initial stage of the impurity puff and therefore would lead to the degradation of the plasma confinement. However, for high seeding levels, in the cases with Ne and Ni, C_E increases. For discharges with similar parameters: magnetic field, density, plasma current, the confinement of the plasma will be hardly affected at the highest N and Ne seeding levels. The strongest degradation of the plasma confinement is expected for Kr seeding.

The radiation profiles in the core for different impurities at the maximum impurity seeding level are shown in the Fig.7.20. As can be seen, radiation in the core by seeded impurities increases with the impurity atomic number, and simultaneously tungsten radiation is reduced. Only for nitrogen, the extrinsic impurity radiation is located close to the separatrix, whereas for other impurities strong radiation in the pedestal region is observed which might affect the confinement properties. In addition, for Ar and Kr, significant part of the radiation is localised in the core. The maximum of the radiation for N, Ne and Ar is at the separatrix, but for Kr the maximum is between separatrix and pedestal. In the case of Ar and Kr seeding, the formation of the radiating belt might be possible.

7.5 Summary

For the examined JET pulses with N and Ne seeding, core and edge parameters as the electron temperature in the central plasma and on the plate, Z_{EFF} , the W

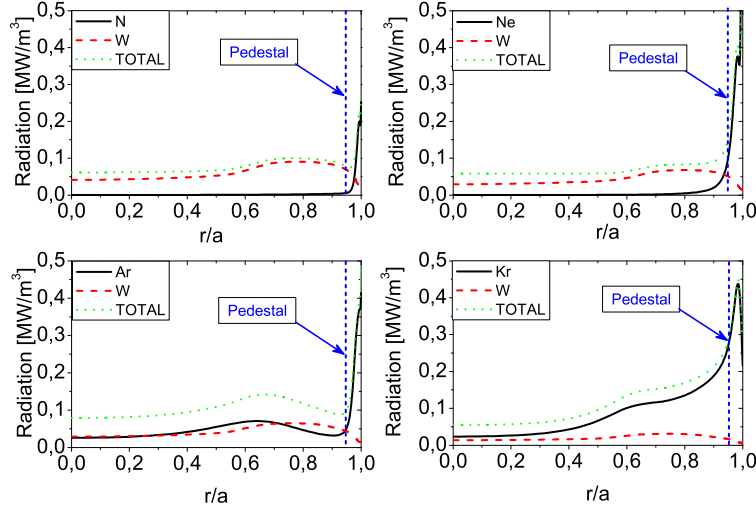


Figure 7.20: Radiation profiles: total, W and seeded impurity in the core. The dotted line shows the pedestal position.

concentration and so on, are fairly well reconstructed with the COREDIV mode, not only for the ONE shot, but for the FULL impurity scan. The module for sputtering and prompt re-deposition reproduces correctly tungsten production.

Simulations show that high-Z impurity behavior can have a detrimental effect on plasma performance. In the case of mid-Z impurities like Ni or Fe, with the larger amount of injected gas, their concentration decreases. It can be explained by the fact that mentioned mid-Z impurities are located outside the divertor region, where Ne seeding was directly applied. For this reason, the process of their release was almost negligible in comparison with W. In the case of Ni, its higher release is usually correlated with RF heating, while during the presented experiment, only NBI heating was in use. In the Chapter 8 analysis of the influence on the auxiliary heating on the impurity transport in JET ILW is presented.

What is also important, results obtained by analysis of the experimental data were consistent with those simulated with the COREDIV code, where prompt re-deposition is included.

For the relatively high levels of the auxiliary heating ($P_{aux} > 13$ MW) impurity seeding to reduce the power to the target is required. Sensitivity studies have been done to give insight on the influence of different impurities on main plasma parameters. The Z_{EFF} is defined by low-Z impurity level, smaller dilution for the case with Kr, $Z_{EFF} \sim 2.2$. Only for nitrogen, radiation is localised close to the separatrix and for Ar and Kr, significant part of the radiation is localised in the core. The maximum radiation fraction (80%) is observed for case with Ne seeding. The W radiation decreases with increasing the impurity atomic number and only for Kr, $C_W \sim 2 \times 10^{-5}$, the W production practically stops. It is possible pedestal degradation and formation of radiation belt for Ne, Ar and Kr seeding. From the simulation with COREDIV code, the better plasma confinement is for cases with N and Ne seeding. It should be stressed, that this conclusion is in full agreement with experimental observations [150].

Chapter 8

Analysis of the influence of the auxiliary heating on the impurity transport in JET ILW

Impurities released from interactions between plasma and material surfaces can lead to major effects on plasma behaviour in tokamaks. This is in particular true for JET experiments with the new ITER-like wall (ILW) configuration (ILW: Beryllium wall + W divertor), which show that the plasma performance is strongly affected by tungsten impurity. Plasma contamination depends strongly on the plasma temperature at the plate which to large extent is defined by the level of the heating power. In addition, depending on the type of the applied heating mechanism (NBI, ICRH), impurity production can be directly affected by the heating scheme.

Therefore, important question is: *How much auxiliary heating influences the impurity behaviour in tokamak plasmas?*

In this chapter, the effect of:

- different heating schemes (NBI, ICRH)
- the applied auxiliary heating power level

on the impurity transport in JET ILW is presented.

8.1 Influence of the different auxiliary heating schemas: analysis with ETS code

In the JET ILW experiment, it is observed that ICRF heating results in larger tungsten and nickel contents in the plasma and in a larger core radiation when compared to NBI heating [151]. For JET ILW, a concern when using the ICRF antennas with the new wall was local heat loads on surrounding Be limiters due to the acceleration of ions in the RF sheath rectified voltages created by the residual parallel electric field near the antenna structure. For example, the pulse #81856 with 3.5 MW of central ICRF heating was applied making the total heating power (with the ohmic power) of

4.8MW and a matching NBI power phase was added to compare the overall effect of the two heating systems on the plasma properties and particularly on the radiation and impurities levels. In the Fig. 8.1, experimental time traces of auxiliary heating power, radiative losses and line-averaged effective charge in both phases are presented. Nevertheless, during ICRF heating the radiation from the core plasma is now higher. The main radiators are W and Ni. It can be seen, that ICRH results in a substantial increase not only of radiative power, P^{RAD} , but also of the effective charge, Z_{EFF} , compared to the NBI phase. Then, one can see that 52 ÷ 56% of the heating power was radiated during the ICRF phases and 23 ÷ 35% was radiated during the NBI phase, the higher percentages being obtained for the lowest density case.

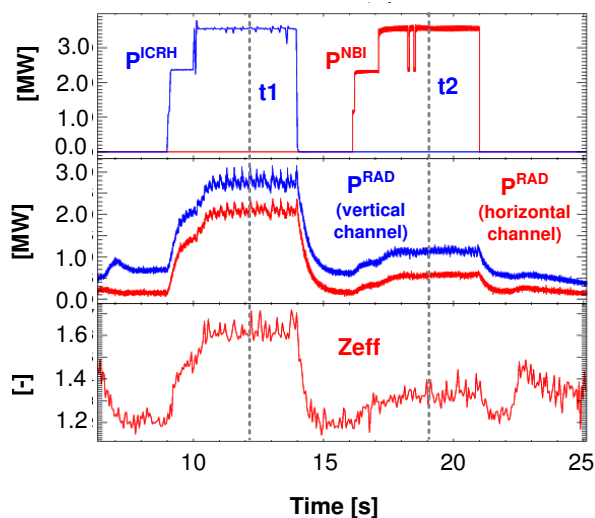


Figure 8.1: JET shot #81856. Experimental time traces of auxiliary heating power, radiative losses and line-averaged effective charge.

In the Fig. 8.2 experimental profiles of the electron temperature and density in both phases are compared. Some difference in temperature is observed within 0.3 of normalized minor radius, which roughly corresponds to 10% of the volume and cannot explain the experimentally observed difference in the total radiative loss. Thus, the plasma contamination during the ICRH phase can be caused either by an increased source of impurities and/or by changes in their transport. With the Be/W plasma facing components, the VUV spectrum was dominated by mid-Z metallic impurities like Ni and also contained intense W features. Thus the question appears how much of the plasma contamination during the ICRH phase can be attributed either to an increased source of impurities or to changes in their transport.

ETS simulations were configured to reproduce experimental profiles of radiated power density and a value of line-averaged effective charge at selected times (ICRH phase, $t_1 = 12.2s$; and NBI phase, $t_2 = 19s$). Three impurity species (all ionization states of W, Ni and Be) have been simulated until the steady state impurity distribution is obtained. Initial profiles and boundary conditions for individual ionization states of impurity ions were obtained from coronal distribution using experimental n_e and T_e profiles and adjusting the total concentration for each impurity.

Spectroscopic measurements of Ni impurity along the vessel midplane were obtained

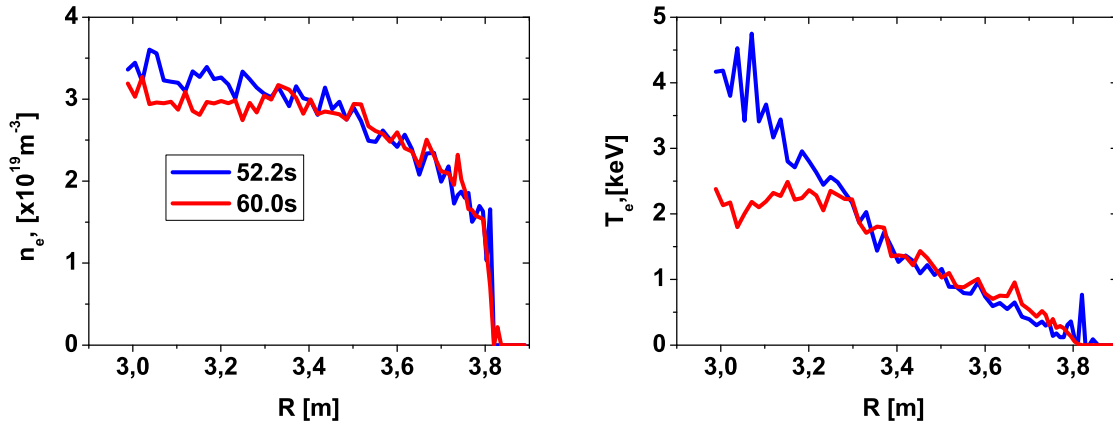


Figure 8.2: Comparison of experimental profiles of electron density and temperature for ICRH (blue) and NBI (red) heating phases in discharge#81856 [121].

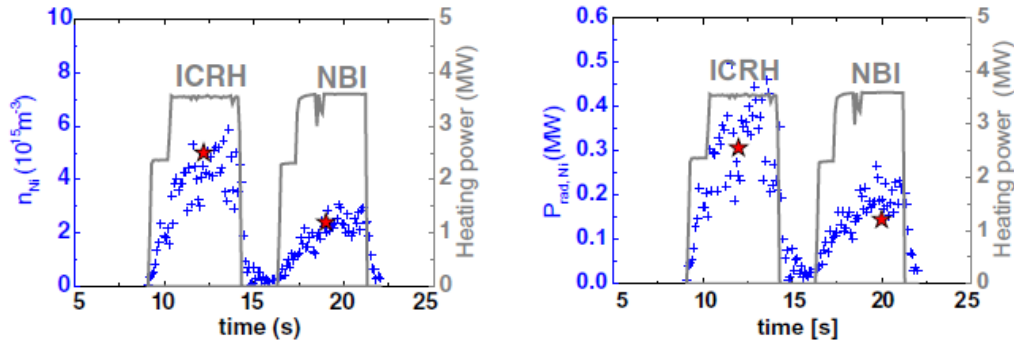


Figure 8.3: ETS input (left): total density of Ni in discharge #81856 obtained with the SPRED diagnostic (blue crosses) and assumed in ETS simulations (red stars). ETS output (right): benchmark of radiation (red stars) from Ni obtained with ETS to the one computed from experimental data using the UTC code (blue crosses).

using the SPRED (survey poor resolution extended domain) spectrometer (see Chapter 4). The time trace of the total density of Ni obtained with SPRED for this shot is shown in Fig. 8.3 (left). From the Ni density, the radiated power due to Ni and its contribution to the bulk plasma radiated power (R^{CORE}) was evaluated based on calculations of the Ni cooling factor presented in [152]. The Ni concentration is up to a factor of three higher for the ICRH phase.

In the simulations, total Ni concentration was taken from experiment, total W concentration was adjusted to reproduce radiative losses and Be concentration was adjusted to reproduce Z_{EFF} . For the NBI phase, the total boundary concentrations were selected to $n_W = 1.1 \times 10^{15} \text{m}^{-3}$, $n_{Be} = 1.0 \times 10^{17} \text{m}^{-3}$, $n_{Ni} = 2.4 \times 10^{15} \text{m}^{-3}$, and for the ICRH phase these values were increased to $n_W = 4.5 \times 10^{15} \text{m}^{-3}$, $n_{Be} = 2.2 \times 10^{17} \text{m}^{-3}$, $n_{Ni} = 5.0 \times 10^{15} \text{m}^{-3}$. The impurity diffusion coefficients have been computed with the L-mode particle Bohm-gyroBohm transport model [106] and assumed to be the same for all impurity ions and all ionization states. Fig. 8.3 (right) compares the radiated power from Ni obtained in ETS simulations to the one computed directly from experimental data using the UTC code. Fig. 8.4 compares the simulated steady state profiles of radiative power density and Fig. 8.5 effective charge with the experimentally

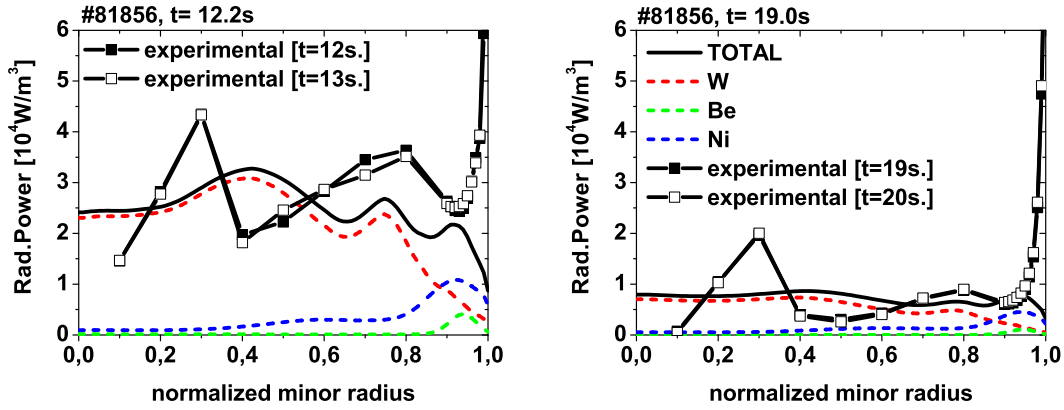


Figure 8.4: Comparison of simulated steady state profiles of radiative power density with experimentally measured ones: black curves total profiles, red curves W contribution to the total; blue curves Ni contribution to the total; green curves Be contribution to the total.

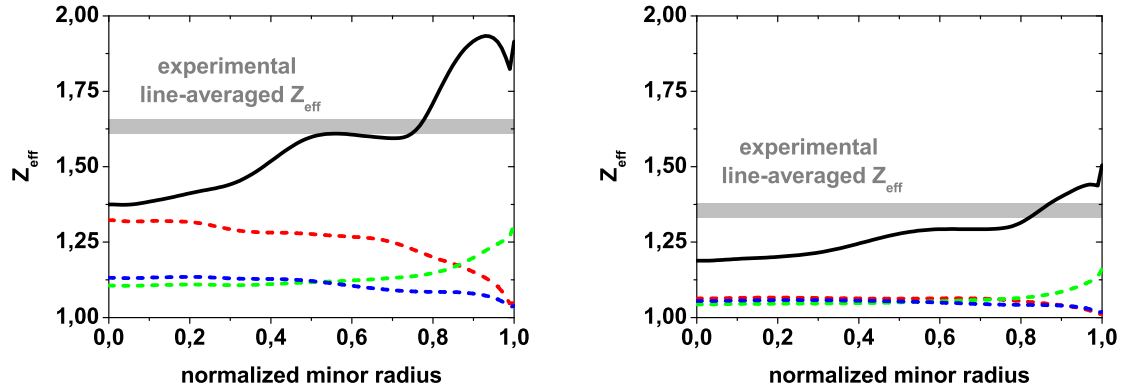


Figure 8.5: Comparison of simulated steady state profiles of effective charge with experimentally measured ones: black curves total profiles, red curves W contribution to the total; blue curves Ni contribution to the total; green curves Be contribution to the total.

measured ones. A reasonable agreement for the total radiative power density profile inside normalized radius 0.95 has been obtained for both heating phases. The core radiation is dominated by W during both, ICRH and NBI phases, with the largest contribution from W^{25+} - W^{35+} ionization states. The radiation near the separatrix is dominated by Ni ions, whereas Be does not contribute much to the radiative losses. Instead, plasma effective charge is mostly due to light ions, e.g. Be and Ni. In contrast to the radiated power profile, flat or slightly peaked in the centre, the effective charge profile is hollow with the maximum at the edge. These computations exclude light Z impurities (like C, O or N), which dominate the radiation over the last centimetres inside the separatrix. Therefore, there is a difference between experimental and computed profiles of the radiated power density outside the normalized radius of 0.95. The total radiated power caused by the light elements is about $12 \div 15\%$. Nonetheless, experimental radiation caused by light impurities is not sensitive to the heating scheme. The increased radiation during the ICRH phase as compared to the NBI is due to increased tungsten and Ni concentration in the plasma. In the simulation performed above the high radiation power during ICRH phase has been obtained by increasing the boundary density for W (source from SOL plasma). Another approach to increase

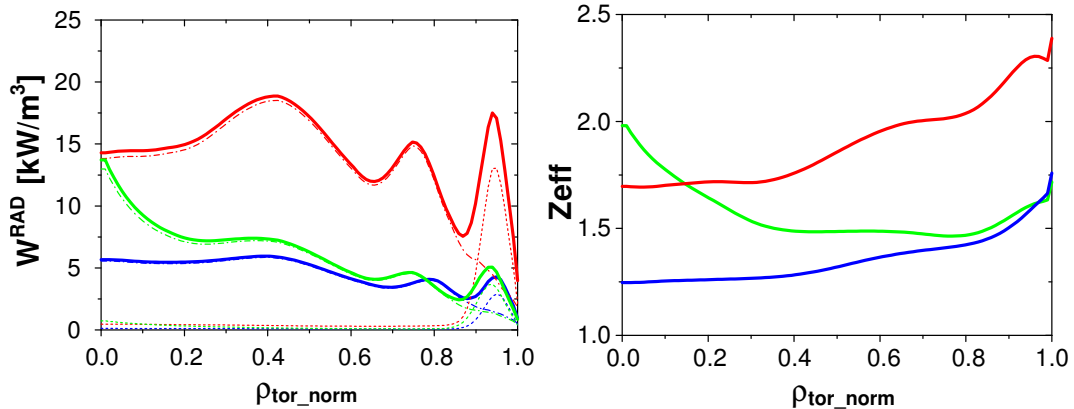


Figure 8.6: JET shot #81856. Simulated steady state profiles of radiative power density and Z_{EFF} : The reference case (blue curves) corresponds to the NBI phase (time t_2). The effects of ICRH (time t_1) are simulated by either increasing the Be and W source (red curves) or increasing the inward Be and W pinch (green curves). Dashed curves total Be contribution; dash-dot curves total W contribution to radiative loss.

the W concentration in the core can be an increase of the inward W convection. Another set of simulations including Be and W was performed to study the sensitivity of core radiation and Z_{EFF} to the boundary concentration versus convective velocity of impurity particles. Starting with the NBI phase, the Be and W sources were adjusted through their boundary values to match the experimentally measured impurity concentration and radiative losses ($n_W = 8.0 \times 10^{14} \text{m}^{-3}$; $n_{Be} = 3.0 \times 10^{17} \text{m}^{-3}$) for Be and W impurity densities assuming zero impurity convective velocity (Fig. 8.6, blue curves). Taking these results as a reference the impurity distribution during the ICRH phase has been first simulated by assuming a radially constant inward impurity convective velocity of 0.5 m/s. This results in an increase of W^{RAD} and Z_{EFF} , mostly at the magnetic axis, where impurities start to accumulate (Fig. 8.6, green curves). Such W^{RAD} profile appeared to be inconsistent with the bolometric measurements showing a rather flat profile (see Fig.8.5) of radiative power during the ICRH phase. In addition, taking into account a small volume contribution from the plasma centre, the total radiative losses change only within a few percent compared to the factor of 2.5 measured in experiment. At the next step, the reference case has been repeated with zero convective velocity and increased (roughly by factor 3) impurity boundary densities ($n_W = 2.35 \times 10^{15} \text{m}^{-3}$; $n_{Be} = 9.1 \times 10^{17} \text{m}^{-3}$). In this case a much better agreement with measurements for W^{RAD} profile and Z_{EFF} is obtained. These simulations indicate that an increased impurity density is a possible reason for the W accumulation during the ICRH phase of #81856, although the effect of a radially shaped convective velocity (not tested here) can not be excluded.

8.2 Influence of the auxiliary heating power level

The time confinement depend on auxiliary power level $\tau_E \sim P_{core}^{-0.69}$ (see Eq. 1.9). In the COREDIV transport model, transport coefficients depend on τ_E . The influence of auxiliary heating is important not only for steady state, but more important for

the ramp-down phase, because one of the major problems in present tokamaks is the presence of disruptions. In this section, results of analysis of the influence of heating power level for both: the ramp-down phase and steady state are presented by means of COREDIV simulation.

8.2.1 Influence of auxiliary power on the impurity in ramp-down phase

Disruptions occur in tokamaks due to loss of stability and/or confinement of tokamak plasmas [2]. Because of the fast time scale on which the plasma thermal and electromagnetic energy are released, strong electromagnetic forces and large thermal loads on the surrounding components can be induced. Understanding of disruptions plays an important role for design of the future fusion devices as they cause large thermal and mechanical loads on a vacuum vessel. The magnitude and scope of these challenges arise from a combination of physics, structural and thermal engineering considerations and from inherent limits on the thermal energy handling capabilities of materials available for plasma-facing component surfaces.

JET with carbon (C) wall and divertor has operated previously with a low frequency of disruptions [153] (i.e. disruption rate) of 3.4%. The analysis of pure Ohmic and L-mode current-ramp-down phase of three JET hybrid pulses is shown in Ref. [154]. JET disruption rate has dramatically increased for JET with the ITER-like wall (equipped with W divertor, and Be wall) [155].

JET discharges with the new ITER-like wall has changed the radiation distribution towards higher plasma core radiation. Switching off the power at termination, as was done with the JET-C, often resulted in a radiative collapse and a disruption.

The percentage of disruptions in JET discharges with the new ILW configuration at high current can exceed 30%. Disruptions in a tokamak can cause dramatic damage to the device. The tolerable heat loads with the ILW are more restricted because of the potential for melting of the tungsten coated tiles at the target or the beryllium PFCs in the main chamber. For ITER an engineering limit for the number of disruptions that can be tolerated has been set to a fraction of 10% of the plasmas operated at high current.

Disruptions represent a complex, multi-faced issue. The understanding of the physics of the causes of disruptions remains an important subject of investigations in order to reduce disruptivity, particularly for the ITER-relevant high density and high current operation. The current ramp-down (RD) of a burning plasma is a challenging part of plasma operation in any fusion reactor and ramp-down simulations and modelling studies have acquired particular importance in a number of papers which have been published recently [156], [157].

The increase in ELM frequency is beneficial and can play an important role in preventing the contamination of the plasma by W in metallic wall devices [158, 159]. Strategies have been developed in present experiments to avoid W accumulation in stationary phases of H-mode discharges by ELM triggering to control the edge W density and by central RF heating to prevent core accumulation. On the other hand,

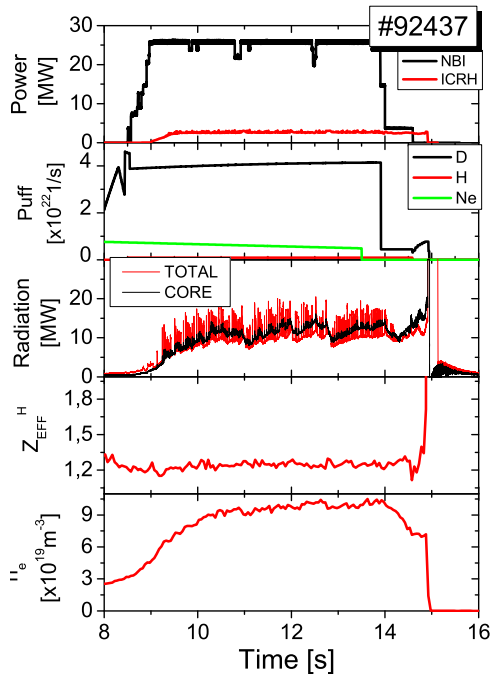


Figure 8.7: Experimental time slices for shot # 92437.

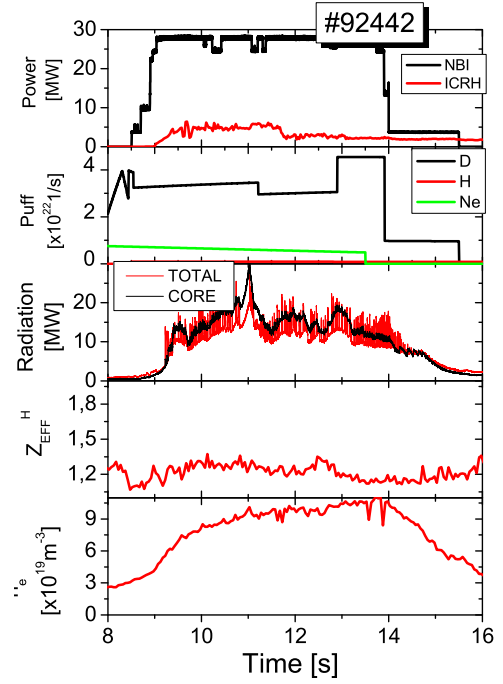


Figure 8.8: Experimental time slices for shot # 92442.

the control of W transport can be more challenging during the confinement transient phases between L-mode and H-mode and in particular in the transition from stationary H-mode to L-mode. During this phase the pedestal plasma density and temperature decrease as the input power is decreased. This can lead to reduced ELM frequencies and extended intermittent ELM-free phases causing uncontrolled increase of the edge W density and peaking of the core density profile, which is favorable for W accumulation. The required ELM frequency to avoid W accumulation can be achieved at JET through adjustment of the gas fuelling level or/and by active ELM control with pellets or kicks (fast vertical plasma motion at an adjustable frequency) [160, 160].

The influence of auxiliary power have been analysed for the ramp-down phase of a set of representative high current JET ILW discharges. The experimental data for two discharges: # 92437(disrupted) and # 92442 (soft landing) characterized with high plasma current $I_p = 3.5\text{MA}$ and high toroidal magnetic field $B_T = 3\text{T}$ have been analysed. The time slices of evolution of the main parameters: auxiliary power, gas puffing, total and core radiation, effective charge (Z_{EFF}) and line average electron density are shown in Fig.8.7 for shot # 92347 and Fig.8.8 for shot # 92442.

In the experimental study of the W concentration in the JET ILW configuration, it was assumed that the main radiator in soft X-ray is W, while the radiation from other metallic impurities is negligible. In Fig.8.9, we present time evolution of W concentration for both shots. As a first observation (see Fig.8.9), the W concentration is similar for both shots at time $t = 13.9\text{s}$ for three positions at the normalised radius (r/a): 0.0 (centre), 0.3 and 0.45 before the start of ramp-down. After reduction of the D puff (see Fig.8.8), the W concentration starts to increase. It can be seen that W concentration is higher at the time $t < 14.5\text{s}$ for the shot with lower D puff (#92437). In

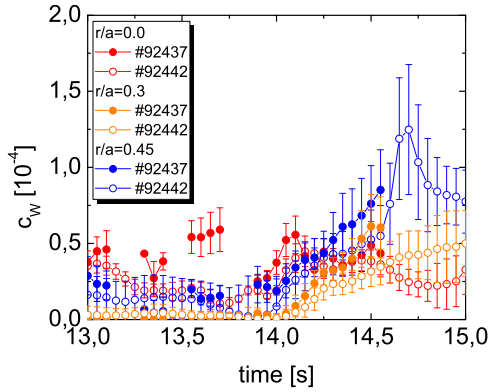


Figure 8.9: The experimental data for W concentration based on soft X-ray for # 92437 (full symbol) and # 92442 (open symbol) for three different position at the normalized radius ($r/a = 0; 0.3; 0.45$).

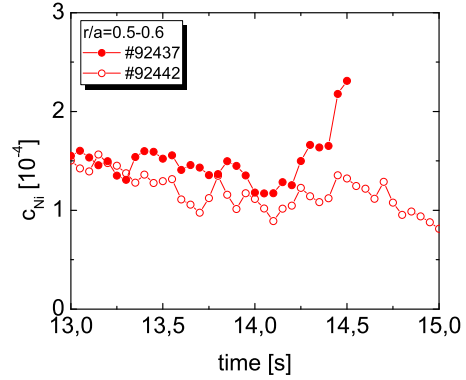


Figure 8.10: Time evolution on the Ni concentration for # 92437 (open symbol) and # 92442 (full symbol) for position at the normalized radius ($r/a = 0.5 \div 0.6$).

Fig.8.10, we show the Ni concentration (C_{Ni}) for both shots obtained at the normalised radius 0.5-0.6. It can be seen that Ni behaves similarly to W. In the case of the disruptive shot (# 92437), we observe an increase of the Ni concentration from 13.9s to 14.25s which is connected to the decrease of the electron density and for $t > 14.25$ s Ni starts to accumulate.

The comparison of the time evolution of the D_α and tungsten WI emission in divertor for both shots is presented in Fig. 8.11 and Fig. 8.12, respectively. Small difference in ELM frequency in both shots of about 20% (see Fig.8.11) for steady state are observed, which could have influence on the higher W and Ni concentration for # 92437 (see Fig.8.9 and Fig.8.10). At the time when the ramp-down phase starts

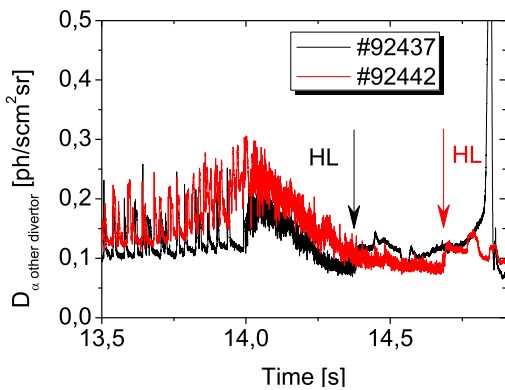


Figure 8.11: Comparison of two discharges.

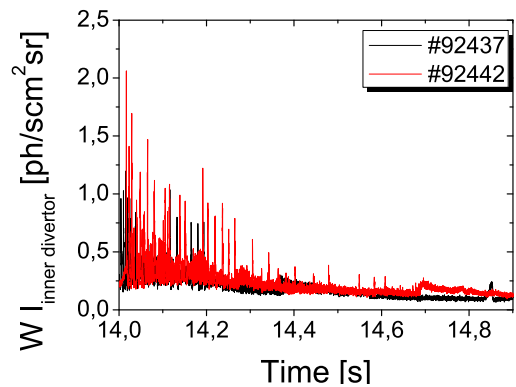


Figure 8.12: Tungsten emission in inner divertor.

($t > 13.9$ s), as the input power (NBI) is decreased, for $t > 14.2$ s an extended ELM-free phases starts. For the shot with lower D puff, increase of the core radiation is observed during the H-mode termination phase, leading to a faster transition to L-mode (marked as H-L transitions Fig. 8.11) for that shot.

It should be noted first, that the maximum of the W and Ni cooling rate is at about

1.4-2keV for coronal distribution (see Fig.8.13) and second, for the electron temperature lower than 200eV, the Ni cooling rate is higher in comparison to W cooling rate and it has a maximum at about 20eV (SOL region for JET ILW). The W radiation for JET ILW in the SOL region is negligible usually ($< 0.14MW$).

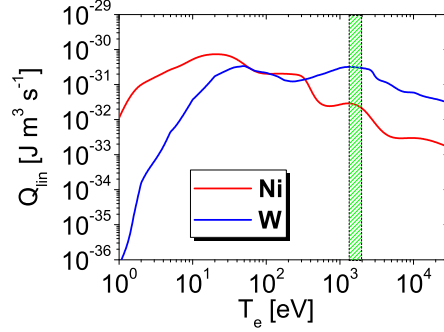


Figure 8.13: COREDIV cooling rates for nickel(Ni) and tungsten(W) in corona equilibrium.

The detailed analysis with COREDIV code have been performed for four different times at the ramp-down phase: $t = 13.9s$; $14.25s$, $14.5s$; and $14.75s$, corresponding to different levels of the electron density and auxiliary heating power. For both pulses between time $13.85s$ and $14.05s$, the NBI heating decreases from $26MW$ to $4MW$ (see Fig.8.7 and Fig.8.8), but electron density does not change significantly. For this reason, at the beginning we present the analysis of the influence of the decrease of the auxiliary heating on the tungsten production and Ni and W concentration in the core plasma. The comparison between experimental (at $t = 13.9s$) and simulated electron density and temperature profiles for different auxiliary heating (all other inputs parameter unchanged) is presented in Fig. 8.14. With the decrease of the auxiliary heating we observe stronger changes in the central electron temperature in comparison to the pedestal region, where the influence is small.

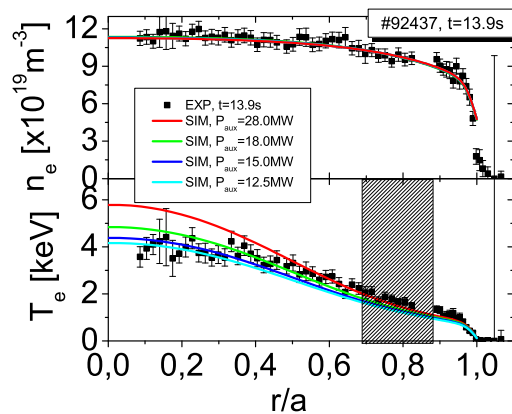
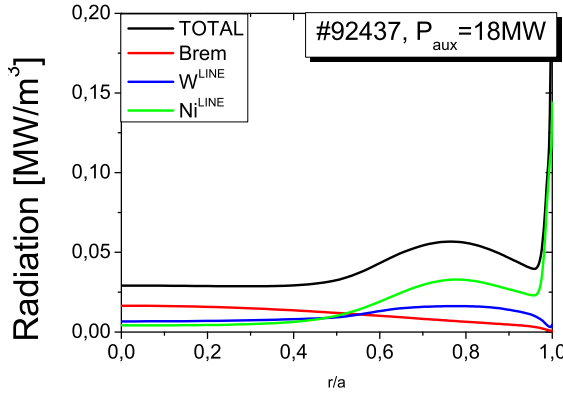
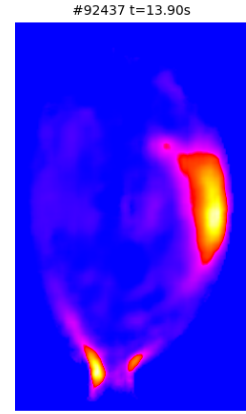


Figure 8.14: The electron density (top), temperature (bottom) profile from HRTS diagnostic at time $t = 13.9s$ for # 92437 with different auxiliary heating.

In the table 8.1, the main plasma simulated parameters are presented: power to the scrape-of-layer (SOL) (P^{SOL}), electron temperature at the plate strike point (T_e^{PLATE}), the total (R^{TOTAL}) and SOL (R^{SOL}) radiations, core line radiation by Ni (R_{Ni}^{LINE}) and by W (R_W^{LINE}), W (C_W) and Ni (C_{Ni}) concentration in the core and W sputtering by W (Γ_{sput}^W) (self-sputtering), by Be (Γ_{sput}^{Be}) and by Ni (Γ_{sput}^{Ni}). The Be core

Table 8.1: Main plasma parameters with different auxiliary heating.

Parameters	$P_{aux}=28\text{MW}$	$P_{aux}=18\text{MW}$	$P_{aux}=16\text{MW}$	$P_{aux}=12\text{MW}$
P_{SOL} [MW]	19.7	14.3	12.9	10
T_e^{PLATE} [eV]	8.3	6.7	5.1	3.9
R^{TOTAL} [MW]	13.1	8.96	8.2	7.6
R^{SOL} [MW]	4.5	4.6	4.6	4.5
R_{Ni}^{LINE} [MW]	1.9	2.3	2.35	2.46
R_W^{LINE} [MW]	6.0	1.1	0.6	0.2
C_W [$\times 10^{-5}$]	2.67	0.5	0.2	0.06
C_{Ni} [$\times 10^{-4}$]	1.03	1.17	1.22	1.23
Γ_{sput}^W [$\times 10^{19}$ 1/s]	1.32	0.1	0.025	0.025
Γ_{sput}^{Be} [$\times 10^{19}$ 1/s]	1.9	0.7	0.4	0.028
Γ_{sput}^{Ni} [$\times 10^{19}$ 1/s]	1.2	0.5	0.36	0.1


 Figure 8.15: Profile of the core radiation at $t = 13.9\text{s}$.

 Figure 8.16: Tomographic reconstruction of the radiated power density for shot #92347 at time $t = 13.9\text{s}$.

concentration in the simulation is about 0.7%. We observe, that with decrease of the heating power, the temperature in the core and also power to the SOL decrease, and since the radiation in the SOL does not change, the power and temperature at the plate decrease. In this situation, the decrease of the W production is observed. We note, that for temperature at the plate, $T_e^{PLATE} < 5\text{eV}$ the main source of W is sputtering due to Ni ions mainly. With the heating power decrease and related decrease of the temperature on the plate, opposite behaviour of W and Ni is observed: W concentration decreases from 2.67×10^{-5} to 0.06×10^{-5} , which is explained by lower production from the plate (see Γ_{sput}^W , Γ_{sput}^{Be} , Γ_{sput}^{Ni} in Table 1), but core Ni concentration increases by 20% and the core Ni radiation increases by 30%. This is correlated with Ni cooling rate (see Fig. 8.13). For the $P_{aux} = 12\text{MW}$, Ni is the dominant radiator in core and SOL region. Good correlation between experiment and simulation at $t = 13.9\text{s}$ is observed for the impurity concentration ($C_W = 0.5 \times 10^{-5}$ and $C_{Ni} = 1.1 \times 10^{-4}$).

The radial profiles of the total, bremsstrahlung, W and Ni radiations in the core for this time ($t = 13.9\text{s}$) from simulations are presented in Fig. 8.15. Nickel (green line) show two maxima of the radiation: one near the separatrix and the second for $r/a \sim 0.75$. We remark, that maximum of the radiation by Ni and W is at the same normalized radius ($T_e \sim 1.4 \div 2\text{keV}$). The radiation around X-point is emitted by Ne and Ni, which correlates well with the tomographic reconstruction (see Fig. 8.16).

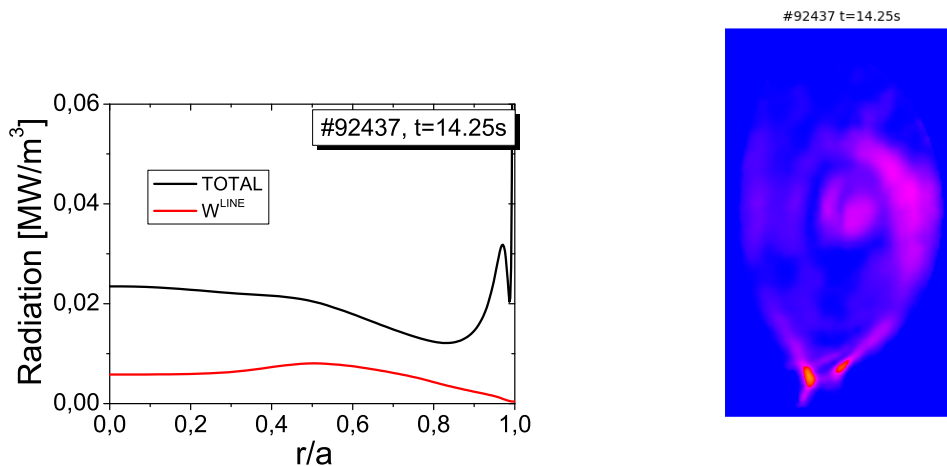


Figure 8.17: Profile of the core radiation at $t = 14.26\text{s}$.

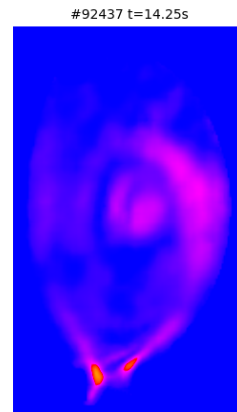


Figure 8.18: Tomographic reconstruction of the radiated power density for shot #92347 at time $t = 14.25\text{s}$.

Regarding the simulation of the second time slice ($t = 14.25\text{s}$) with lower auxiliary power (12MW), the reconstructed radiation profile is shown in Fig. 8.17 and the tomographic reconstruction in Fig.8.18.

The decrease of the heating power, affects the temperature in the core resulting in the inward shift of the maximum of the radiation from $r/a = 0.75$ to $r/a = 0.5$. The radiation is also more uniform in the core.

8.2.2 Influence of auxiliary power level on the impurity seeding in H-mode discharges

In order to characterize and understand the operational space of JET plasmas with the ITER-like wall, series of numerical scans has been performed for nitrogen seeded H-mode discharges. Extended series of simulations have been done to show the influence of input power level on JET plasma parameters for different levels of nitrogen seeding and comparison to experimental data has been done. Simulations have been performed with the basic input parameters as for the JET shot #83175 ($B = 2.7\text{ T}$, plasma current $I = 2.47\text{MA}$, $H_{98} = 0.75$). The code has been run assuming the same ratio between the edge and average density $n_e^{sep} / \langle n_e \rangle = 0.57$ and the transport in the SOL was fixed with radial diffusion $D_{perp}^{SOL} = 0.25\text{ m}^2/\text{s}$. It comes out from the COREDIV simulations, that for every power level, there is always a maximum impurity seeding level above which no steady state solution exists.

Different plasma parameters versus nitrogen influx for different heating power levels $P_{aux} = 13 \div 30\text{ MW}$ are shown Fig. 8.19. It can be seen that the radiation fraction

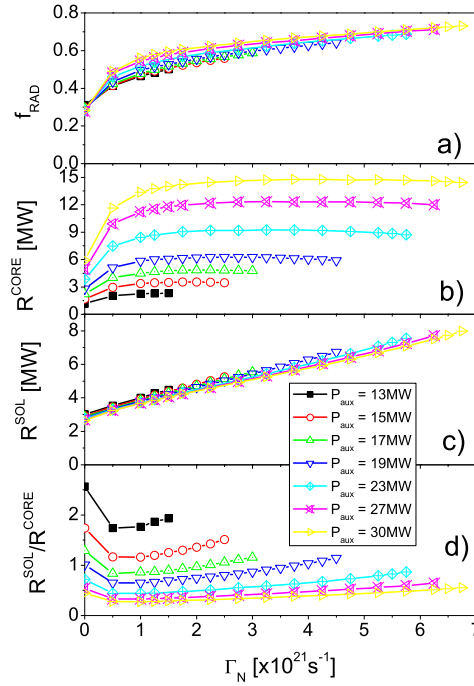


Figure 8.19: Plasma parameters versus nitrogen puff level for plasma density $\langle n_e \rangle = 7 \times 10^{19} \text{m}^{-3}$ and auxiliary heating powers $P_{aux} = 13 \div 30 \text{ MW}$: a) radiation fraction, b) core radiation, c) SOL radiation and d) ratio between SOL and core radiations

(f_{RAD}) (8.19a) weakly depends on the input power and even seeding levels, at least for $\Gamma_N > 10^{21} \text{part/s}$.

The core radiation (R^{CORE}) (Figs. 8.19b), being in principle tungsten radiation is almost independent of the seeding level, after initial increase for $\Gamma_N < 10^{21} \text{ part/s}$. However, it depends strongly on heating power, because with increase of the heating the temperature on the plate increases also (see Fig.8.20), which mostly determines the W production rate (sputtering strongly depends on temperature). Regarding the ratio between SOL and core radiations (Figs. 8.19d), it is large only for low power discharges and weakly depends on the seeding level. Z_{EFF} is almost linear function of the seeding level and independent of power levels, whereas the power to the plate

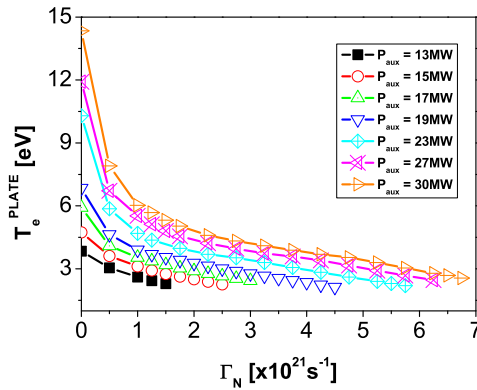


Figure 8.20: Temperature on the plate versus nitrogen puff level for plasma density $\langle n_e \rangle = 7 \times 10^{19} \text{m}^{-3}$ and auxiliary heating powers $P_{aux} = 13 \div 30 \text{ MW}$.

(P^{PLATE}), as expected, reduces with the increased seeding (not shown here). The maximum radiation fraction found in the simulations is up to 80%.

It should be noted that also other calculations have been performed for different impurity - neon puff for three values of the auxiliary heating power: that is $P_{aux}=15.2$, 27, and 40MW and the results are presented in Fig.8.21 [161]. First, it can be seen that the radiation fraction (Fig.8.21a) saturates with seeding ($\sim 80\%$) and weakly depends on the heating power level, similarly to the case with nitrogen. It is interesting to note that, at the constant heating power level, the core radiation (R^{CORE}), power to the plate (P^{PLATE}), power to SOL, and even the SOL radiation (P^{SOL}) saturate with seeding. Seeding, however, leads to strong plasma dilution ($Z_{EFF} \gg 3$), at least for the considered relatively low density scenario ($n_e = 6.2 \times 10^{19} \text{m}^{-3}$). The degradation of the transport (Fig.8.21) is larger for higher heating powers, but it saturates with seeding after an initial strong change. Strong heating leads also to significant tungsten production and, consequently, high plasma contamination by W ions ($c_W \sim 3 \times 10^{-4}$).

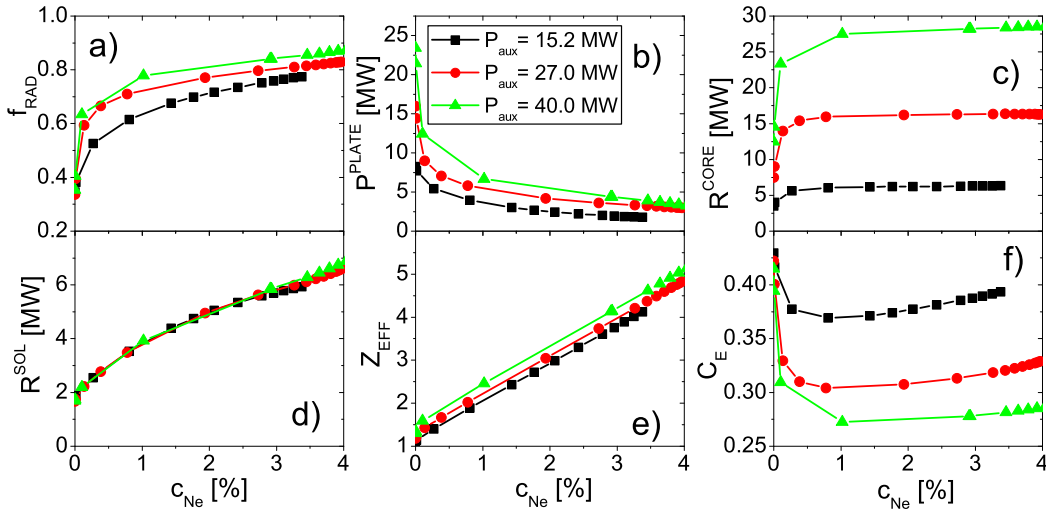


Figure 8.21: Plasma parameters versus neon concentration for $H_{98} = 1.2$: (a) radiation fraction (f_{RAD}), (b) power to the target plates, (c) core radiation, (d) SOL radiation, (e) Z_{EFF} , (f) transport multiplication factor.

8.2.3 Influence of auxiliary power level for DT plasma

The influence of the heating power level might be of extreme importance for the JET DT experiments. The temperature profile strongly depends on the heating, and since the cross section for the D-T reaction depends only on the ion temperature, the heating power affects strongly the alpha power level (P_α). The specific analyses has been prepared for hybrid shot #92398. The comparison of the experimental and simulated profiles is shown in Fig.8.22 (DD plasma).

It can be seen that the main plasma parameters for this shot with the original power of $P_{aux}=30.5$ MW have been reproduced by the simulations. Next, extrapolation has been done for DT discharges assuming the same heating power and for increased

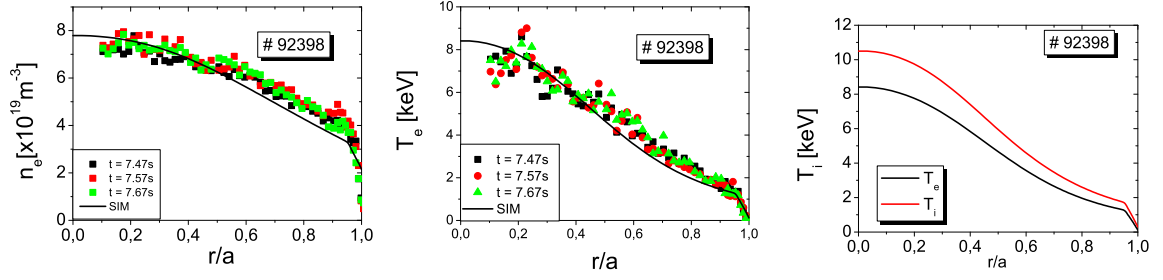


Figure 8.22: Experimental and simulated electron density (left) and electron temperature profiles (central) and electron and ion temperature (right) for #92398 at time $t \sim 7.5$ s.

auxiliary heating $P_{aux} = 39$ MW. The main plasma parameters: alpha power, power to the plate, P^{PLATE} , total (R^{TOTAL}) and core (R^{CORE}) radiation, Z_{EFF} , W and Be concentrations, W flux sputtered by D(T), He, Be, Ni and W (self-sputtering) and temperature at the plate are shown in the Table 8.2 for two different powers and plasma scenarios (DD and DT). Some experimental parameters are also shown for comparison.

It should be noted, that increase of the auxiliary heating by 20% leads to the increase of the alpha power (considering only thermal contribution) from 0.96MW to 1.2MW. For the case with highest heating power the power to plate is well above 20MW and impurity seeding might be obligatory to control the heat load to the plate.

Table 8.2: Main plasma parameters.

Parameters	EXP DD	SIM DD	SIM DT	SIM DT (39MW)
P_α [MW] [MW]			0.96	1.2
P^{PLATE} [MW] [MW]	21	18.64	18.66	25.27
R^{TOTAL} [MW] [eV]	9.4	11.86	11.84	13.73
R^{CORE} [MW]	8.72	8.7	8.6	10.2
Z_{EFF} [MW]	1.77	1.7	1.72	1.8
C_W [%]	1.4×10^{-2}	1.55×10^{-2}	1.56×10^{-2}	2.03×10^{-2}
C_{Be} [%]		1	1	1
$\Gamma_{sput}^{D(T)}$ [$\times 10^{19}$ 1/s]		0	0.038	0.67
Γ_{sput}^{He} [$\times 10^{19}$ 1/s]		0	0.01	0.021
Γ_{sput}^{Be} [$\times 10^{19}$ 1/s]		2.56	2.6	3.14
Γ_{sput}^W [$\times 10^{19}$ 1/s]		4.41	4.47	6.69
Γ_{sput}^{Ni} [$\times 10^{19}$ 1/s]		2.5	2.5	2.8
T_e^{PLATE} [eV]		26.3	26.2	29

It is found that for this JET DT case, helium has small influence on the W production. Indeed, the fusion performance of the considered hybrid scenario shot is weak in terms of the achieved fusion power and related helium particle production.

8.3 Summary

For JET ILW configuration, integrated modeling is very important and should include not only core and SOL region, but also self-consistent simulations of the W source. For that reason analysis of the impurity transport are performed with COREDIV code, which is suitable tool for such studies.

It has been found that the tungsten radiation plays always very important role and can not be mitigated even by strong influx of nitrogen (or Ne). Simulations show that the observed Z_{EFF} level is defined mostly by the low Z impurity content, Be and N₂ in the considered shots. Numerical studies for seeded plasmas indicate the existence of the limited range of accessible gas puff levels (for a given heating power level) which might impose restrictions on the JET operational domain.

In addition, the sensitivity study shows, that a possible reason for the W accumulation during the ICRH phase is an increased concentration of W at the edge.

It should be noted also that simulations leads to the observation that for the same average electron density, the decrease of the auxiliary power, leads to the reduction of the W production. The consequence is the shift of the maximum of the radiation towards the plasma centre.

Chapter 9

Influence of the electron separatrix density on the impurity

In the experiment, the leading parameter determining electron separatrix density n_e^{sep} was found to be the neutral divertor pressure, which can be considered as an engineering parameter since it is determined mainly by the gas puff rate and the pumping speed. In ASDEX Upgrade [162] and JET [163], measurements of the upstream separatrix density for H- modes reveal a strong correlation with the divertor neutral pressure. It has also been postulated that n_e^{sep} may play a role in the loss of confinement in H- modes. A low separatrix density is beneficial for the plasma energy confinement, while a high density enables and supports the achievement of divertor detachment [164]. An important tokamak operational limit, the H-mode density limit, is also connected to an upper limit of the separatrix density [165], [166].

The normalized separatrix density versus the Greenwald density, for discharges (except pellet injected) fueled by gas puffing for different tokamaks is analysed in Ref. [165] and presented Fig. 9.1. The highest values for n_e^{sep}/n_{GW} are only achieved at

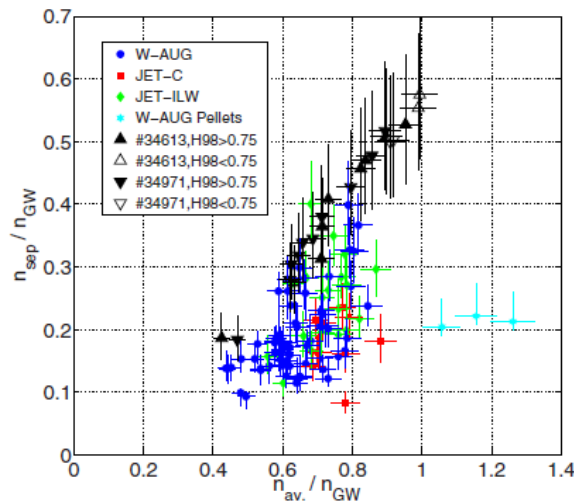


Figure 9.1: The normalized separatrix density, n_e^{sep}/n_{GW} , versus the normalized line average density, n_e^{av}/n_{GW} .

high Greenwald density fractions and hence the H-mode density limit is only observed

at $n_e^{av}/n_{GW} \approx 0.8 \div 0.9$. In general the variation of the ratio between the separatrix and line averaged density reflects the large operational condition the data base represents. For example data from JET operation with carbon plasma-facing components are observed to reach high line averaged density and simultaneous low edge density. In L-mode a n_e^{sep}/n_{GW} ratio of approximately one-third is generally assumed as reported elsewhere. In H-mode the situation is further complicated by the formation of the pedestal and the presence of ELMs. In the ELMs, density at the separatrix changes.

Direct measurements of the (upstream) separatrix density are not easily available. The major experimental problem stems from the correct assignment of the separatrix position from equilibrium reconstruction, which suffers uncertainties comparable to the radial density decay length. In JET ILW the edge Thomson scattering diagnostic and the Li-beam diagnostic are used for measurement of the density profile near separatrix.

The electron density at the separatrix (n_e^{sep}) appears to be important parameter in integrated modeling. Therefore in COREDIV modelling, separatrix density is considered usually as input parameter to match, when available, with the experimental data. Due to the self-consistency of COREDIV, even a small change in n_e^{sep} may lead to changes in the density profile in the core as well as in the SOL, resulting also in changes in the electron density at the divertor plate, and consequently, in temperature at the plate. This may finally lead to modification of W sputtering and concentration and of the level of radiation losses in the plasma core.

The main questions of this chapter are:

- *how much the density at the separatrix influences the core plasma contamination?*
- *what is the effect of the separatrix density on the W production?*

9.1 Influence of the electron separatrix density on the ramp-down phase

The influence of the plasma density at the separatrix on the impurity production and transport during the plasma termination phase for two discharges: # 92437 (disrupted) and # 92442 (soft landing) have been studied with COREDIV code. The experimental analysis for this shots has been presented in Chapter 8. Since the deuterium gas fluxes are different, we are assuming that the gas injection controls the separatrix density. In the simulations, four impurities: Be, W self-consistently related by sputtering from divertor targets, puff of Ne (very small level) in divertor region and puff of Ni are considered. The first source of the nickel particles seen in JET may originate from remote cutting of some Inconel (58%Ni, 21%Cr, 9%Mo) brackets which carried out during the ILW installation. The second source is by ICRF antenna, which is in mid-plane. Although ICRH is the main tool used to prevent W accumulation in the centre of JET plasmas, application of ICRH usually leads to an overall increase of the plasma impurity content, and in particular in JET ILW, tungsten (W) and nickel (Ni). The source of Ni is the tokamak chamber, and for this reason, in the simulations Ni impurity is represented as a uniform gas puff from the JET wall. We use in the

9.1. INFLUENCE OF THE ELECTRON SEPARATRIX DENSITY ON THE RAMP-DOWN PHASE

simulations the same transport model, in which transport coefficients depend only on confinement time (from scaling law).

The influence of the separatrix density on the plasma electron density and temperature, which might be connected with different deuterium puff in the experiment, is simulated and shown in Fig. 9.2 for the time $t = 14.48\text{s}$. With the decrease of the

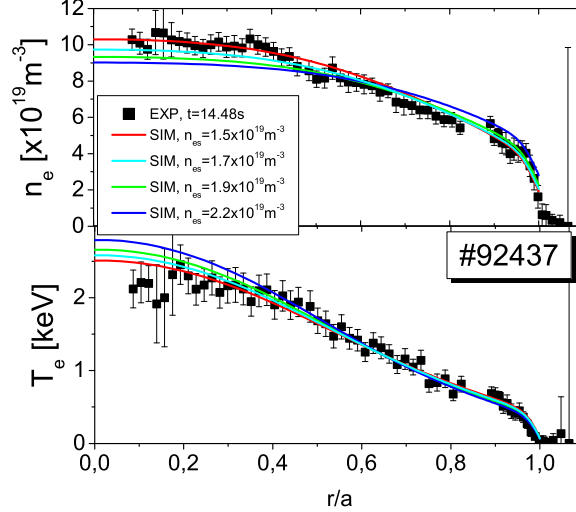


Figure 9.2: Experimental (HRTS) and reconstructed T_e and n_e profiles at $t = 14.48\text{s}$ with difference density on the separatrix (n_e^{sep}).

electron separatrix density, keeping the same volume average density, we observe the increase of the density in the centre (comparison between red and blue lines) and the related decrease of the central temperature. The main plasma parameters versus different separatrix density are presented in Table 9.1. With the decrease of the separatrix density (lower fuelling), increase of the temperature on the plate is observed. As a results, the W production and core W concentration is increasing, which is in agreement with SXR measurements (see Fig.8.9). We remark, that decrease of the separatrix density by 25% resulted in a 5 times increase of the W radiation and W concentration in the core. The change of the separatrix density in this case has no influence on the Ni concentration. The influence of the changes of the separatrix density on the profiles

Table 9.1: Main plasma parameters with different separatrix densities.

$n_e^{sep} [\times 10^{19} m^{-3}]$	2.2(0.31 n_e)	1.9	1.7	1.5(0.23 n_e)
T_e^{PLATE} [eV]	5.32	6.8	7.7	10.6
R^{TOTAL} [MW]	4.43	3.9	3.8	4.0
R^{SOL} [MW]	2.27	1.9	41.7	1.45
$C_W [\times 10^{-5}]$	0.8	1.2	2.2	4.5
R_W^{LINE} [MW]	0.13	0.18	0.31	0.7
$C_{Ni} [\times 10^{-4}]$	1.	0.98	1	1.05
R_{Ni}^{LINE} [MW]	1.51	1.44	1.45	1.49

of the radiated power (simulated and experimental) at $t = 14.48\text{s}$ is shown in Fig. 9.3.

9.1. INFLUENCE OF THE ELECTRON SEPARATRIX DENSITY ON THE RAMP-DOWN PHASE

The maximum of the W and Ni radiation is seen to move towards the centre. The dominant radiation in the core region is by nickel.

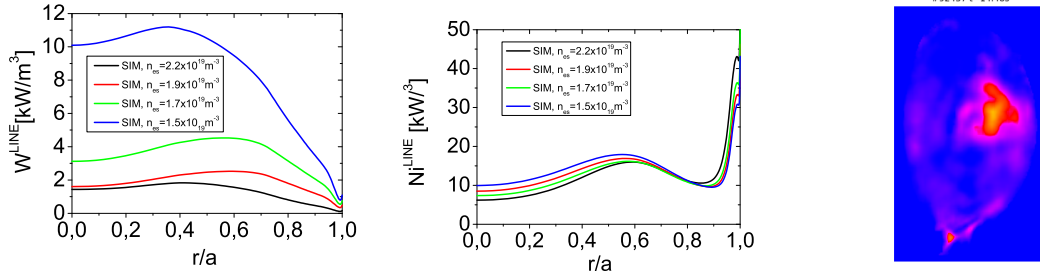


Figure 9.3: Tomographic reconstruction of the radiated power density for shot #92347 at time $t = 14.25s$.

The main conclusion from this simulations is the observation that for the same average electron density, the decrease of the separatrix density leads to an increase of the plasma temperature at the divertor plate leading to increased W production and consequently to larger W concentration and radiation in the core.

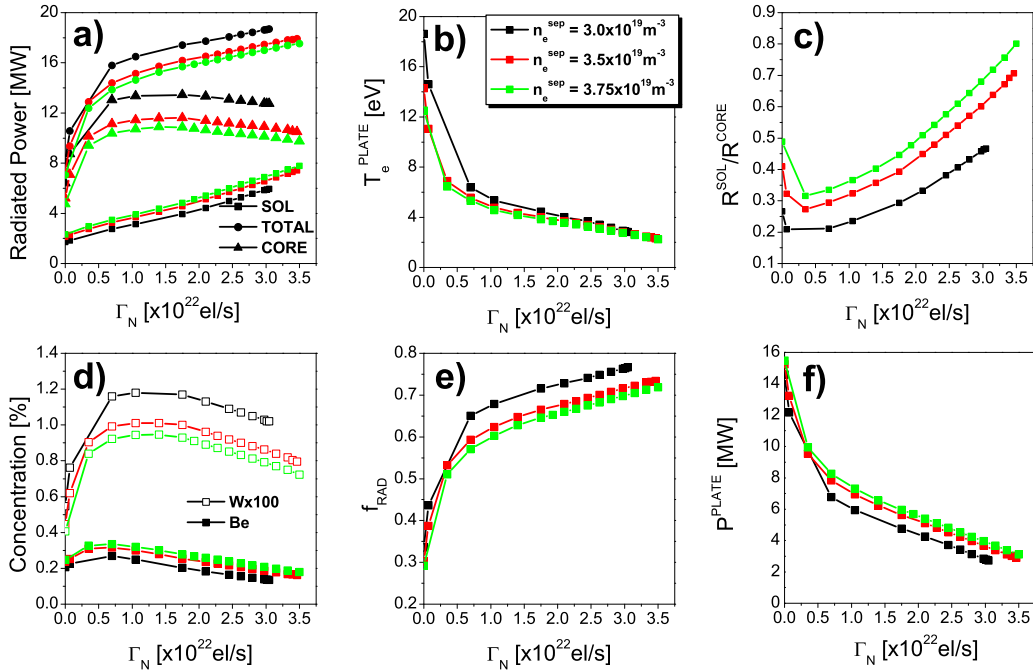


Figure 9.4: Hybrid regime: plasma parameters versus nitrogen gas puf for three different electron density on the separatrix electron density is $n_e^{sep} = 3.0 \times 10^{19}m^{-3}$ (black line), $n_e^{sep} = 3.5 \times 10^{19}m^{-3}$ (red line) $n_e^{sep} = 3.75 \times 10^{19}m^{-3}$ (green line): total (circle symbols), core (square symbol) and SOL (triangle) radiation (a), electron temperature at the plate (b), radiation SOL/CORE (c), W and Be concentration (d), radial fraction (e), power to plate (f).

9.2 Influence of the electron separatrix density on the impurity in steady state plasmas

Influence of the separatrix density on the nitrogen seeded hybrid discharge (shot # 83570) is shown in Ref.[143]. In the Fig.9.4, results of numerical scan with different levels of nitrogen gas puff for hybrid scenario with input parameters fixed for the shot # 83570 and with three different density values at the separatrix are presented. The initial increase of the N₂ influx ($\Gamma_N < 1 \times 10^{22}$ el/s) leads to strong increase of the tungsten concentration and consequently core radiation as a result of increased tungsten production. However, for higher fluxes ($\Gamma_N > 1 \times 10^{22}$ el/s) the changes to the core parameters are rather weak. This is the result of a self-regulating mechanism being a specific feature of tungsten (metallic) targets. This mechanism regulates the tungsten production due to sputtering processes at the target plates by radiative cooling of tungsten ions in plasma centre. Since the radiation efficiency of tungsten is very high and simultaneously the dependence of the sputtering yield on the temperature (incident ion energy) is very steep, the equilibrium between production and radiation appears at temperature values very close to the sputtering threshold. The SOL radiation increases linearly with gas puffing reducing effectively the power to the targets. For the highest seeding levels, semi-detached conditions are achieved in divertor with ($T_e^{PLATE} < 3$ eV). It has been found that the tungsten radiation plays always very important role and can not be mitigated even by strong influx of nitrogen in hybrid scenario.

9.3 Summary

The observed changes to the impurity behavior are related mostly to the improvement of the screening efficiency of impurity ions with higher separatrix density. The increase of n_e^{sep} leads to the reduction of tungsten concentration and correspondingly the radiation in core is also reduced. The SOL radiation increases but not strongly enough to compensate for the reduction of R_{CORE} and consequently total radiation is reduced as well. For experimental point of view, it is important to note, that strong deuterium puffing might be beneficial for seeded discharges, since it increases the edge density and plasma collisionality.

The separatrix density being a code input parameter appears to be a very important quantity controlling the SOL plasma properties. In the self-consistent simulations its effect is however limited mostly to the changes in the screening efficiency of the SOL, which leads to the better confinement of W ions in the edge and consequently to lower radiation losses in the core.

Chapter 10

Influence of the impurity radial transport in SOL

It appears that collisional transport is not able to explain the perpendicular (radial) transport coefficients derived from experimental measurements in the scrape-off layer. The measured transport coefficients are about 10 times larger than those predicted by collisional transport theory $D_{perp}^{SOL} \approx \chi \approx 1 \div 10 \text{ m}^2/\text{s}$ [2, 41, 167]. The perpendicular transport processes in the plasma edge related to turbulence convective or diffusive transport caused by microinstabilities might be responsible for SOL transport [147]. In the COREDIV code, similarly to other edge codes (SOLPS, EDGE2D, JINTRAC...) radial transport in the SOL (D_{perp}^{SOL}) is an input parameter. Therefore the question of the sensitivity of the modelling results to the assumed value of the radial transport coefficients is of the primary importance.

First investigations with COREDIV code of the influence of the radial transport JET ILW discharges have been presented in my paper Ref.[143]. The main plasma parameters: concentration of the impurities (W, Be and N), total, core and SOL radiations, electron temperature at the plate and the effective charge versus radial diffusion coefficient are presented in the Fig.10.1.

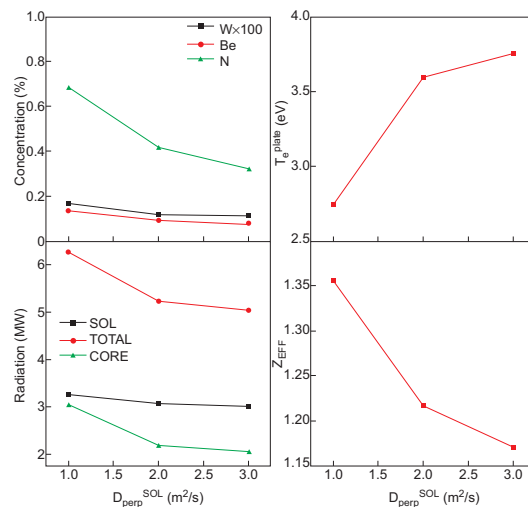


Figure 10.1: Plasma parameters for different radial diffusion coefficient in SOL (D_{perp}^{SOL}).

It can be seen that larger diffusion leads to the better screening of W impurity by SOL plasma leading to the reduction of the core W concentration and radiation, as well as Z_{EFF} . However, the effect is relatively small, 3 times higher D_{perp}^{SOL} leads only to 25% reduction of the core radiation. This effect is similar to the effect of the increased separatrix density (see Chapter 9).

In Fig.10.2, the influence of both, the edge density (n_e^{sep}) and radial transport in the SOL (D_{\perp}) on the plasma radiations is shown for the case of nitrogen seeding. The increase of n_e^{sep} leads to the reduction of tungsten concentration and corresponding core radiation (R^{CORE}) is also reduced. The SOL radiation increases, but not strong enough to compensate reduction of radiation in core and consequently total radiation (R^{TOTAL}) is reduced as well. Similarly, higher D_{perp}^{SOL} improves the screening efficiency of the SOL, which means that the impurities produced at the target do not penetrate so efficiently core plasma and stay in the divertor/edge region and as consequence, we observe reduction of the core radiation being the effect of the reduced W concentration, which leads to the reduction of R^{TOTAL} . It is important to note, that much more energy can be radiated in the SOL with the increased transport or increased edge density, which indicates that strong deuterium puffing might be beneficial for seeded discharges, since it increases the edge density and plasma collisionality.

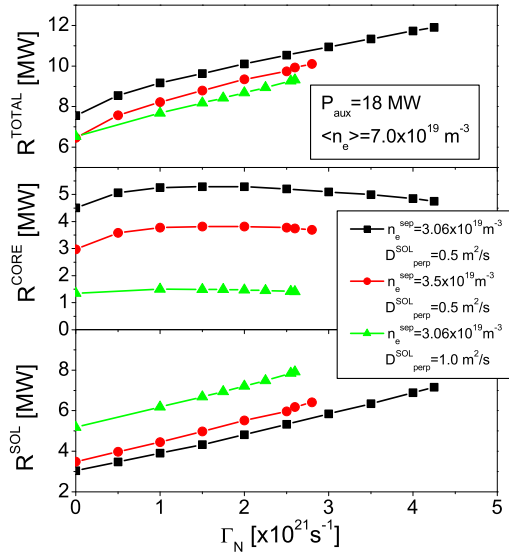


Figure 10.2: Plasma parameters versus nitrogen puff level for different edge densities, $n_e^{sep} = 3.06 \times 10^{19} \text{ m}^{-3}$, $n_e^{sep} = 3.5 \times 10^{19} \text{ m}^{-3}$ and different radial diffusion coefficients in the SOL, $D_{perp}^{SOL} = 0.5 \text{ m}^2/\text{s}$, $D_{perp}^{SOL} = 1 \text{ m}^2/\text{s}$ a) total radiation losses, b) core radiation, c) SOL radiation.

Experiments in JET ILW configuration indicate that W density in the core plasma is reduced for f_{ELM} 's frequency above 40 Hz [168] and is correlated with the impurity flushing out mechanisms by ELMs [53]. This effect of the ELM's is taken into account in the COREDIV simulations by imposing strong increase in the diffusion coefficient.

In JET ILW plasmas, the Ne injection not only leads to enhanced radiation in the SOL and around the X-point, but also to increased tungsten release, with related enhanced core radiation and possible reduced ELM frequency. Results of COREDIV

simulations on that issue are presented in Ref.[169] where focus is given to the relation between the level of Ne seeding rate and the change in the impurity transport. The series of Ne seeded low-delta ELMy H-mode pulses with heating power up to 29.5 MW and with two different levels of seeding rate, as well of gas fueling is considered in that study. It is observed experimentally, that the ELM activity decreases significantly, while the plasma energy remains unchanged. In these pulses the volume average density, $\langle n_e \rangle$, is in the range $6 \div 7 \times 10^{19} \text{m}^{-3}$, P_{aux} from 22 to 29.5 MW (NBI + ICRH), the two steps in Ne seeding rate are 5 and $12 \times 10^{21} \text{e/s}$ and the two steps in D_2 gas fuelling rate are 1.9 and $3.7 \times 10^{22} \text{1/s}$. The radiated power fraction changes from 0.47 to 0.61 and the ratio of radiated power in the SOL to the total one (R^{SOL}/R^{TOTAL}) is between 0.35 and 0.43. Although the simulations refer to the inter-ELM phase of the discharges, since production as well as flushing out of W due to ELMs is not accounted for in the present model, the numerical results might be compared with experimental data averaged over several ELM periods.

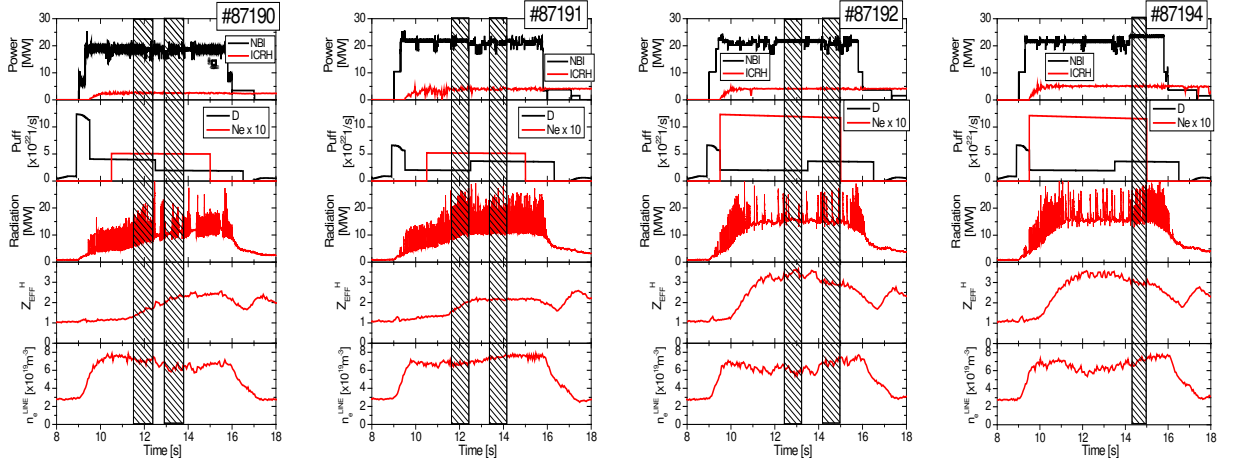


Figure 10.3: Experimental time traces of the four pulses examined. The seven time slices of the simulated shot points are shown.

Fig.10.3 shows some time-dependent traces of the four pulses. In # 87190 (first from left) axially heating is 22MW, $\Gamma_{Ne} = 0.5 \times 10^{22} \text{ e/s}$ and for $t = 14.5 \text{ s}$ with $\Gamma_D = 4.0 \times 10^{22} \text{ e/s}$ ELM activity is stationary with $f_{ELM}=40 \text{ Hz}$, $Z_{EFF}=1.9$ and radiation fraction is 0.47. Starting from $t = 14.5 \text{ s}$ the gas fuelling decreases to $\Gamma_D = 1.8 \times 10^{22} \text{ e/s}$ and the ELM behavior is non-stationary, alternating periods of ELM activity with $f_{ELM} = 40 \text{ Hz}$ with ELM-free periods. Correlated also with a slight decrease in $\langle n_e \rangle$, Z_{EFF} goes up to 2.4 and $f_{RAD} = 0.52$. In # 87191 (second from left) the two gas fuelling steps are interchanged in time, but their values are quite similar to those in the previous pulse, while remains $\Gamma_{Ne} = 0.5 \times 10^{22} \text{ e/s}$. With power heat 26MW, ELM activity is stable at both Γ_D , $f_{ELM} = 60 \div 70 \text{ Hz}$, with Z_{EFF} around 2 and $f_{RAD} = 0.54$ and 0.47, respectively. In #87192 (third), $\Gamma_{Ne} = 1.3 \times 10^{22} \text{ e/s}$ while all the other inputs are kept as in the previous pulse. ELM activity is non-stable with $f_{ELM} = 5 \div 9 \text{ Hz}$, Z_{EFF} in the range 3.4 – 3.0 and f_{RAD} around 0.55. Adding 1MW of ICRH, as in shot # 87194 (fourth) up to $t = 14.5 \text{ s}$, does not improve the situation with respect to Z_{EFF} and f_{ELM} . At $t = 14.5 \text{ s}$, 2 more megawatts NBI are added resulting in $P_{aux} =$

29.5MW. Even though no significant improvement is observed with respect to Z_{EFF} , a tendency towards a more regular ELM behavior might be seen, with f_{ELM} which becomes 15Hz.

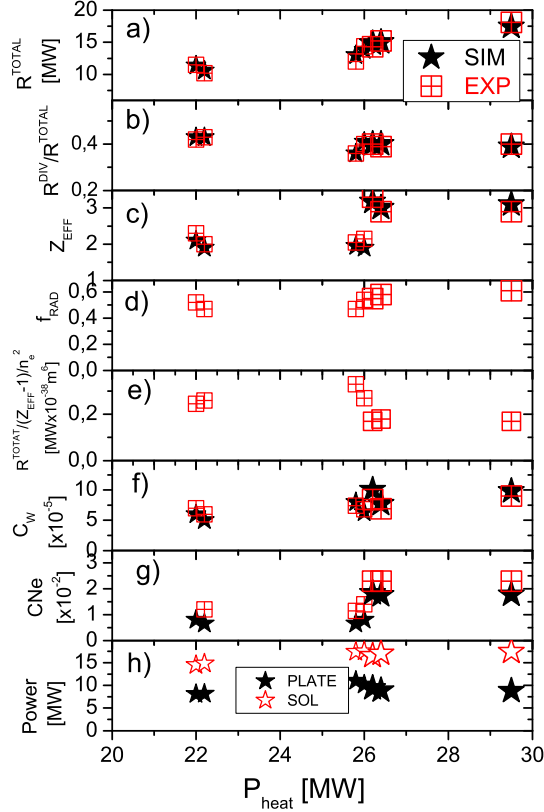


Figure 10.4: Comparison experiment-simulation for the seven "shot points" here considered.

In Fig. 10.4 the seven shot-points have been ordered according to P_{aux} and the four points referring to $P_{aux} = 26$ MW have been slightly displaced in P_{aux} to avoid superposition. The points referring to $\Gamma_{Ne} = 1.2 \times 10^{22}$ e/s have been drawn with larger symbols. Fig. 10.4a,b,c show that R^{TOTAL} , R^{SOL}/R^{TOTAL} and Z_{EFF} , which are the basis of our comparison experiment-simulation, have been numerically reconstructed with good accuracy. Fig. 10.4d shows that the experimental f_{RAD} (as well as the simulated one) does not increase significantly by increasing Γ_{Ne} , which, however, leads to a clear increase in Z_{EFF} . Note, that this conclusion is in agreement with other simulation for Ne seeding in JET ILW. Figs. 10.4f and g show that the experimental volume averaged W concentration (from SXR) and the central plasma Ne^{10+} ion concentration (from CXRS) match with the simulated ones, considering the error bar (order 20%) of the measurements. The electron temperature at the outer strike point, measured by LP (with significant error bar), is in the range $6 \div 9$ eV, while the simulated one is in the range $4 \div 6.5$ eV. Considering that the experimental T_e at the inner strike point is about 2-3 eV lower than at the outer one, the discrepancy experiment-simulation is consistent with the COREDIV SOL model, in which in-out symmetry is assumed (only one target plate). Fig. 10.4h shows that high Γ_{Ne} level is an effective tool to reduce the power to the plate also at high P_{aux} .

Together with P_{aux} , $\langle n_e \rangle$ and Γ_{Ne} two other input parameters have been changed shot-point to shot-point in order to match simulations with experiments: the perpendicular SOL diffusivity D_{perp}^{SOL} and the anomalous impurity pinch V_{pinch} . Differently from modelling of unseeded pulses with $D_{perp}^{SOL} = 0.25$ m²/s, it has been set $D_{perp}^{SOL} = 0.45$ m²/s for the points at $\Gamma_{Ne} = 0.5 \times 10^{22}$ e/s and $D_{perp}^{SOL} = 0.7$ m²/s for the points at $\Gamma_{Ne} = 1.2 \times 10^{22}$ e/s. This dependence of D_{perp}^{SOL} on the level of Γ_{Ne} is made to match the simulated with the experimental R_{SOL} . To match both the simulated R_{CORE} (i.e. $R^{TOTAL} - R^{CORE}$) and Z_{EFF} with the experimental data, V_{pinch} had to be changed from -0.3 to -0.8 m/s. It might be observed (see Fig. 10.4f) that, in contrast to neon concentration C_{Ne} , C_W is relatively insensitive to the application of a high V_{pinch} for the pulses at higher Γ_{Ne} . This depends basically on the fact that, being W highly collisional in the SOL (more than neon), a further decrease in the SOL temperature leads to a change in the balance between frictional and thermal forces in the divertor, resulting in a screening effect more pronounced for W than for Ne. In other words: increasing Γ_{Ne} , the W flux to the separatrix is reduced more than that of Ne while W and Ne suffer the same inward pinch in the confined plasma.

10.1 Summary

Using the actual steady-state version of COREDIV it is not possible to simulate the effect on W release caused by single ELMs. However, for T_e^{PLATE} above 3 ÷ 4 eV the W sputtering yield by Ne together with that by Be and by W self-sputtering provide a simulated W flux, which is comparable to that experimentally observed for the most common JET ELMy H-mode situations, once the data are averaged over times $\tau_A \gg 1/f_{ELM}$.

Indeed, in JET ELMy-H mode the experimental Γ_W is found to be in the range $3 \div 9 \times 10^{19}$ 1/s [168], as in COREDIV simulations. In particular, for this series of pulses the intensity of the WI emission line at 401 nm, measured at the outer divertor, shows a slight increase (up to about 30%) with increasing P_{aux} , but it remains nearly stationary with increasing Γ_{Ne} , at constant P_{aux} , in agreement with the calculated COREDIV total W fluxes, which increase from about 7 to 9.5×10^{19} 1/s.

In spite of the inner-outer symmetry assumption and of the analytical description of the neutrals which both might hamper the validity of the SOL model especially for situations close to detachment, the global properties of the SOL, as the radiated power and by consequence the average electron temperature at the plate, are sufficiently well numerically reproduced, due also to the adjustment of the particle diffusion coefficient in the SOL, D_{perp}^{SOL} . The change in D_{perp}^{SOL} is a technical tool to fitting the numerical power to SOL with the experimental one and it reflects the increase in collisionality with decreasing the divertor temperature [147].

Experiments and COREDIV modelling indicate that Ne seeding is an efficient method to maintain the power load to the target plates at an acceptable level also at high P heat (order 30 MW) in JET-ILW pulses. However, the level of Γ_{Ne} should be modulated according to the level of Γ_D and of P_{aux} to maintain Z_{EFF} at acceptable

values. Indeed, when for given Γ_D and P_{aux} the neon seeding rate exceeds a certain threshold, COREDIV simulations indicate that an inward impurity pinch is triggered, experimentally related to the reduction in the ELM activity.

The simplifying assumptions made in the SOL and in the core of COREDIV in order to model self-consistently the complex interaction core-edge plasma certainly attenuate the validity of the quantitative numerical results. However, the modeling of the considered pulses indicates a clear trend and suggests, for given auxiliary heating and deuterium puff, a limit in the level of Ne seeding.

Chapter 11

Modelling of JET DT experiments in ILW configurations

Significant controlled fusion power was first produced during the Preliminary Tritium Experiment (PTE) in JET in 1991, when a hot ion H mode plasma containing 11% tritium in deuterium produced 2 MJ of fusion energy and a fusion power gain $Q = 0.12$ [170]. In 1997, a series of high-power discharges ($P_{aux} \approx 21 \div 26$ MW) using DT (deuterium, tritium) mixtures in edge-localized mode(ELM)-free H mode were performed in the JET DTE1 experimental campaign with carbon walls and a divertor. A fusion power of 16.1 MW was achieved at 4.0 MA/3.6 T corresponding to the record fusion yield of $Q = 0.64$ [171]. Since 2016, the JET scientific programme is engaged in a multi-campaign effort including experiments in D, H and T [172], leading in 2020 and the experiments with DT mixtures [173]. The highest performance DTE1 plasmas were dynamic in terms of energy confinement, whereas plasma scenarios are being developed for DTE2 with the aim of maintaining high fusion performance in steady conditions with respect to the energy confinement and fast ion-slowing-down times. The energy confinement of JET plasmas has also been affected by the change in first wall materials [174] and the constraints for divertor compatibility with metal plasma-facing components are more challenging. Consequently, the benefits of direct extrapolation from the highest performance DTE1 experiments to the conditions expected in DTE2 are limited. Therefore, the high-performance plasma scenarios that are foreseen for DTE2 operation are based either on a conventional ELMy H-mode at high plasma current and magnetic field or on the so-called improved H-mode or hybrid regime of operation with higher normalized energy confinement. The preliminary COREDIV extrapolation of the reference ELMy H-mode shot #87412 to high-power ($P_{aux}=41$ MW) DT operation shows good core plasma performance with a fusion power of ~ 6.5 MW [141] and is presented in Chapter 6. Although for hybrid plasmas it might be possible to sustain 40 MW of heating power for $\sim 5 \div 6$ s within the ILW divertor temperature limits [175], it would be advantageous to be able to use impurity seeding (e.g., Ne) to increase the margin with respect to the engineering limits. COREDIV preliminary simulations [141] showed that neon seeding leads to rather beneficial effect on the plasma performance, allowing for a relatively wide operational window in terms of the amount of the allowed neon influx. That prediction, however, should be confronted with the fact that

impurity seeding dilutes fuel and, in most instances, reduces the fusion performance of JET plasmas in the plasma domain relevant for high-performance in DTE2 [176].

In order to further investigate the possible range of operating scenarios, COREDIV modelling was used to investigate the effects of impurity seeding (Ne, N) in extrapolation to high power/current/field scenarios for the DT operation. In particular, numerical scans have been performed in terms of different input powers ($P_{aux} = 15 \div 40$ MW), confinement factors ($H_{98} = 0.8 \div 1.2$), plasma currents ($I = 2.5 \div 4.5$ MA), magnetic fields ($B = 2.1 \div 4.0$ T), and plasma densities ($n_e = 0.6 \div 1.1 \times 10^{20} \text{m}^{-3}$). As a first step, it is simulated plasma performance by increasing the input power and simultaneously changed other parameters, keeping constant the β_N value (normalized beta). Next, the power scan at constant current ($I=2.5$ MA) is presented for two seeding gases: neon and nitrogen.

One of the main objectives of the coming deuterium and deuteriumtritium JET campaigns is to extend the performance of the ILW at higher plasma current (> 2.5 MA) by fully exploiting the JET machine capability at high additional powers in the range of 40 MW. To reach these objectives, two main approaches are being pursued: (a) the ITER baseline scenario by simultaneously increasing the current, toroidal field, and applied powers at $q_{95} > 3$ and $\beta_N > 1.8 \div 2$, and (b) the ITER hybrid scenario at slightly reduced plasma current and higher $q_{95} > 3 \div 4$ but at $\beta_N > 1.8 \div 2$, where confinement is increased at high beta through the interplay between the core and edge confinement optimization [177].

In our study, first the expected level of radiation and heat loads at high current scenarios without impurity seeding is assessed, considering that the strike point sweeping might be sufficient to control the heat loads to the divertor targets. The following assumptions have been made: $q_{95} = 3 = \text{const}$; $B = I \times 3.8/4.5$ (B in T, I in MA); $n_e/n_{GR} = \text{const} = 0.62$; $\beta_N = \text{const}$ ($=1.6$ at $H_{98}=0.8$) $\sim W_{th}/I^2$; $H_{98} = \text{const}$; $P_{aux} \sim I^{1.65}$; and $n_e^{sep} = 0.4 \times n_e$. Numerical scans have been performed for values of the plasma current given in Table 1 and H_{98} ($=0.8, 1.0, 1.2$) with the corresponding β_N values $\beta_N=1.6, 2.0, 2.4$, respectively. It should be noted that, in order to keep β_N constant, the power increases strongly with the current.

Table 11.1: Main plasma parameters for different plasma current.

I [MA]	2.5	3.0	3.5	4.0	4.5
P_{aux}	15.2	20.5	26.4	32.9	40
B [T]	2.11	2.53	2.96	3.38	3.80
n_e [$\times 10^{20} \text{m}^{-3}$]	0.62	0.74	0.86	0.99	1.11
n_e^{sep} [$\times 10^{20} \text{m}^{-3}$]	0.24	0.29	0.34	0.39	0.43

Fig. 11.1 shows total heat load to the divertor (P^{PLATE}), radiation fractions (f_{RAD}), and tungsten concentration (c_W) versus the plasma current for different H_{98} values. It appears that most of the global parameters (radiation levels, particle and energy fluxes) are very weak functions of H_{98} . However, the core and pedestal temperatures increase

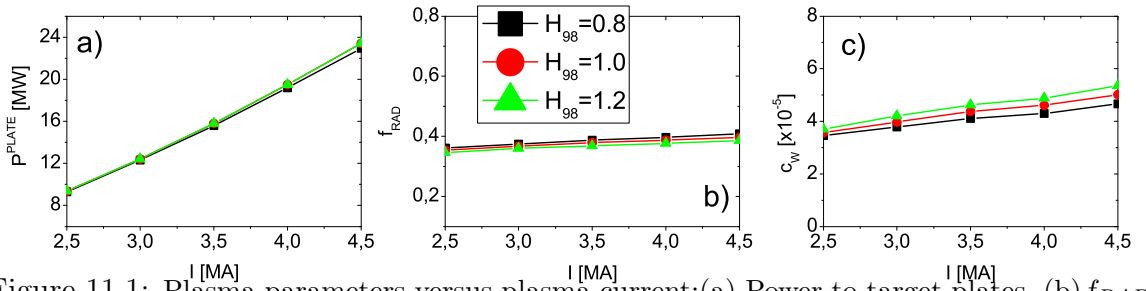


Figure 11.1: Plasma parameters versus plasma current:(a) Power to target plates, (b) f_{RAD} , (c) W concentration.

with H_{98} , as can be seen from Fig. 11.2, where the radial temperature profiles are shown together with the core radiation profiles, which are also affected by changes to H_{98} . With a higher core electron temperature, the maximum of the radiation profile shifts from a more central radial position $a/r=0.8$ to the pedestal region $a/r=0.93$.

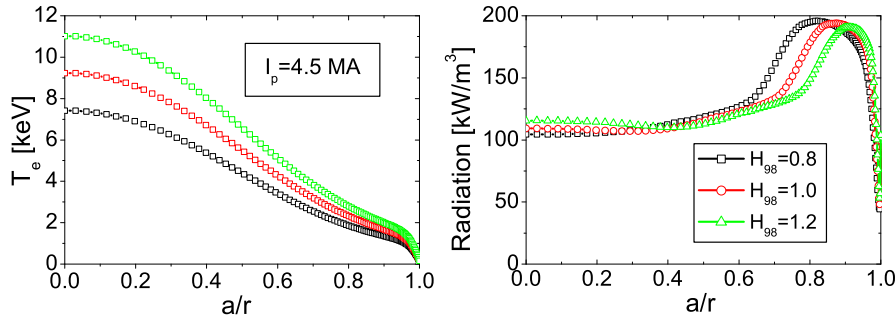


Figure 11.2: Radial profiles of electron temperature and plasma radiation for the highest plasma current ($I=4.5$ MA).

Without seeding, the radiation level is rather low ($\sim 35 \div 40\%$) (Fig. 11.1b), and the corresponding heat load to divertor target plates might not be sustained in the steady-state high-current operation [175]. That indicates that strike point sweeping might not be sufficient to control the heat loads to the target plates at peak plasma performance, and additional impurity seeding might be necessary.

In order to check the effect of seeding on the plasma performance, simulations have been done assuming different levels of the Ne puff (the source of Ne is placed at the wall in the divertor region). Only cases with $H_{98}=1$ and $I \geq 3$ MA are considered, and the results are presented in Fig. 11.3.

The influence of neon seeding on the plasma performance is quite positive. Already small amounts of neon puff ($C_{Ne} \geq 0.2\%$) leads to the increase of the W production and the corresponding significant plasma radiation (Figure 11.3a) and reduction of the power to the divertor plates (Fig 11.3b) [176]. It should be noted that the radiation fraction is independent of the plasma current and approaches $\sim 70\%$ of the input power. That, however, is enough to reduce the heat load to the target plates to sufficiently low levels (~ 5 MW). The plasma radiation is always dominated by the core tungsten radiation, which saturates already at relatively small neon concentrations ($C_{Ne} \geq 0.2\%$) (note that our transport model does not consider strong W accumulation). We note also that the tungsten concentrations are always low and stay below $\ll 10^{-4}$ level, in

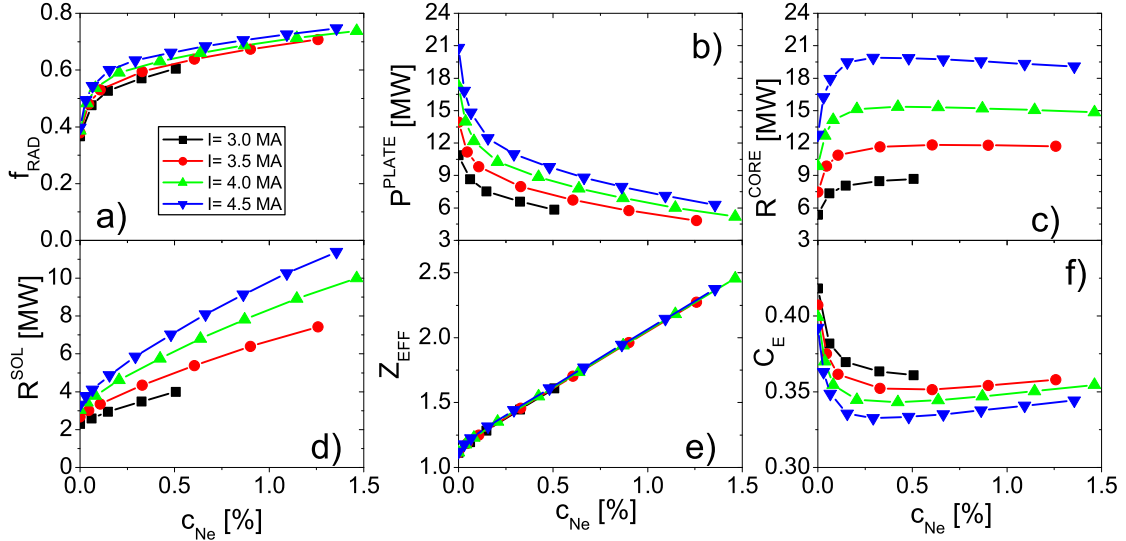


Figure 11.3: Radial profiles of electron temperature and plasma radiation for the highest plasma current ($I=4.5$ MA).

agreement with experimental findings. The SOL radiation increases almost linearly with seeding, and at high seeding levels contributes significantly to the energy losses. Simultaneously, Z_{EFF} stays at a reasonable level (≤ 2.5), showing that the plasma dilution due to seeding should not be a problem at the highest performance thanks to the plasma density increase with the power (in line with our constant β_N assumption). The confinement factor H_{98} is kept constant in our simulations, which is achieved by feedback control of the transport coefficients. The corresponding control parameter (CE) is plotted in Fig 11.3f. It can be seen that when the seeding starts, the plasma transport (proportional to CE) has to be reduced to keep H_{98} constant, which indicates that seeding might lead to some degradation of the transport. Note that the radiation from the plasma core increases while the H-factor is fixed, so the net energy confinement time ($\sim W_{th}/(P_{in} - R^{CORE})$) increases and the local transport reduces. However, at higher seeding ($c_{Ne} > 0.25\%$), confinement starts to improve with seeding because of the lower W radiation caused mostly by reduction of the W source (due to neon cooling of the divertor region).

11.1 Summary and discussion

The high performance plasma scenario, which was proposed recently for the DT operation based on a conventional ELMy H-mode at high plasma current and magnetic field has been analyzed. Simulations for the reference shot #87412 show good agreement with the experimental data but the direct extrapolation of the DD results to deuterium-tritium operation shows relatively poor performance in terms of the achieved fusion power.

The situation improves, if the highest heating power is assumed (41 MW) and JET configuration with high magnetic field (3.9 T) and plasma current (4.1 MA) is

considered. Assuming good energy confinement ($H_{98} = 1$), fusion powers in the excess of 12 MW can be achieved. All the high performance shots require the heat load control by neon seeding which shows rather beneficial effect on the plasma performance allowing for relatively wide operational window in terms of the amount of the allowed neon influx.

A constant β_N scan was performed for the so-called hybrid scenario. The results of simulations showed that, without seeding, the radiation level was rather low ($\sim 35 - 40\%$) and the corresponding heat load to the divertor target plates might not be sustained in the steady-state high-current operation. That indicates that, strike point sweeping might not be sufficient to control the heat loads to the target plates at peak plasma performance, and additional impurity seeding might be necessary[10]. The effect of neon seeding on the plasma performance is quite positive, and already a small amount of neon puff ($C_{Ne} > 0.2\%$) leads to significant plasma radiation and reduction of the power to the divertor plates. It is interesting to note that at the constant heating power level, the core radiation, power to the plate, power to SOL, and even the SOL radiation saturate with seeding.

Chapter 12

Summary and Outlook

This thesis is devoted to the investigations of the impurity transport in the JET ILW configuration, using numerical codes COREDIV and ETS with the most complete available description of the relevant physics processes. Presented analysis are to provide the results necessary to assess the suitability of the COREDIV and ETS codes for the simulation of impurity transport and their effect on plasma parameters. In the experiments carried out over the course of this work the impurity seeding was applied to L-, H-modes and hybrid discharges by means of nitrogen and neon seeding.

Sensitivity numerical studies have been done to give insight on the influence of different impurities on main plasma parameters: Z_{EFF} is defined by low-Z impurity level and only for nitrogen, radiation is localised close to the separatrix, for Ar and Kr, significant part of the radiation is localised in the core and possible pedestal degradation for Ne, Ar and Kr seeding and formation of radiation belt for Ar and Kr seeding are foreseen.

Since one major uncertainty in impurity modelling is related to the role of anomalous transport, analysis have been done to assess the effect of the transport on the results in order to obtain a better understanding of the influence of the impurities on the plasma parameters. On the basis of the results of experiments and numerical analyses, the influence of the following physical factors on the concentration and properties of plasma pollution in the JET system was investigated: impurity seeding, auxiliary heating, density of the plasma at the separatrix, transport in SOL, prompt re-deposition effect. The work presented in this thesis leads to some important conclusions:

- The auxiliary heating have important role on the impurity transport. The degradation of the transport is larger for higher heating powers, but it saturates with seeding after an initial strong change. Strong heating leads also to significant tungsten production and, consequently, high plasma contamination by W ions. In ramp-down phase, for the same average electron density, the decrease of the auxiliary power, leads to the reduction of the W production, which is mainly due to Ni (mid Z impurity) sputtering. In the core, the consequence is the shift of the maximum of the radiation towards the plasma centre.
- The sensitivity study shows that a possible reason for the W accumulation during the ICRH phase is an increased concentration of W at the edge.

-
- The transport analyses conducted here indicate a strong role of the electron separatrix density, which in experiment might be controlled by D puff or pellet injection.
 - COREDIV results show that the frictional drag is an important parallel transport mechanism for W in the SOL, contributing to the W screening.

It was also shown that using appropriate scenarios of plasma discharge and plasma heating it is possible to reduce concentration of plasma impurity. In addition, it has been proven that the analysis of the transport of impurity can be carried out using the COREDIV code reliably and quickly compared with other codes. That has been recognised by fusion community members and directly expressed in the paper by Marco Wischmeier [178] *"While the total radiation from impurity seeding simulated by the code COREDIV is the same as that of SOLPS5.0, the underlying plasma profiles in the divertor are very different and so will be other aspects that may be extracted. However, in view of extrapolating to a Fusion Power Plant and being able to quickly assess the operational space such reduced numerical models as well as even simpler 1D or 0D scalings are the currently only feasible path. Validated reduced models of various levels of complexity may then be used in system codes to determine the performance of future devices and to specify their design. "*

Based on the good agreement between the experiments and numerical analyses with COREDIV and ETS codes, a number of physical factors have been investigated to assess the influence of the impurities on JET ILW plasma discharges and provide necessary understanding of the related phenomena, and thus contributing to the optimization of plasma discharges in the ITER and the DEMO reactors and other devices under construction (eg. DTT, JT60SA).

The results of the described studies are presented in numerous publications in scientific journals and were the basis of many communications presented at international scientific conferences.

The content of the presented work fully justifies the thesis **that physical models applied in COREDIV and ETS codes allow to obtain results in accordance with experimental results and explain a number of phenomena related to the transport of impurities in the JET ILW tokamak.**

List of Tables

7.1	The experimental and simulated global plasma parameters for shots #82031 and #82033.	70
7.2	The experimental and simulated global plasma parameters for shots #83178-80.	70
7.3	The experimental and simulated global plasma parameters for hybrid regime.	71
7.4	The caption inside a table environment.	75
8.1	Main plasma parameters with different auxiliary heating.	93
8.2	Main plasma parameters.	97
9.1	Main plasma parameters with different separatrix densities.	101
11.1	Main plasma parameters for different plasma current.	111

List of Figures

1.1	Reaction rates of potential fusion reactions for reactors [1].	8
1.2	Basic structure of a tokamak [10].	10
1.3	Limiter and divertor configuration shown in the poloidal cross-section of a tokamak with indicated flow pattern [3].	11
1.4	L- and H- mode pressure profile [12].	12
1.5	Thermal energy confinement: observed vs. predicted [24].	14
1.6	JET ILW [29].	15
1.7	The ingredients in plasma physics.	18
2.1	Energy dependence of the sputtering yields of Be and W bombarded by D, C, O, Ne and Ar ions. Experimental data are fitted using an empirical equation for the sputtering yields [33].	21
2.2	Self-sputtering yield of W versus angle of incidence(α) at fixed energy of incidence [35].	21
2.3	Sputtering yield of W by different impurities implemented in the COREDIV code.	22
2.4	Chemical erosion for carbon by incident deuterium ion with different energy at elevated temperature.	23
2.5	Schematic depiction of prompt redeposition during the first cycle of gyration around the magnetic field line. The magnetic field is directed toward the viewer as indicated [30].	26
2.6	The fraction of not promptly redeposited W ions [54].	26
2.7	Energy levels and processes on the atoms[61].	27
2.8	The carbon(left) and argon (right) equilibrium ionization state distribution.	30
2.9	Cooling rate for Be, N, Ne, Ar, Kr, W in coronal equilibrium.	31
3.1	Illustration of the dependence of the diffusion coefficients on collisionality and the identification of the different regimes contributing to neoclassical transport [2].	41
3.2	Stability diagram of ITG/TEM modes. Electron and ion temperatures are equal [71].	42
3.3	Shape on the barrier in the COREDIV code depend of the barrier depth(A) and parameter EX	44
4.1	Positions of the KY4D Langmuir probes in the JET divertor.	46
4.2	Lines-of-sight of the bolometer system, including main chamber and divertor viewing systems.	47

4.3	LOS of the SXR, XUV and VUV diagnostics at JET used for determining mid- and high-Z impurities concentration. The lines of sight of vertical SXR cameras (blue) as well as KT2 (pink) and KT7 (orange) VUV spectrometers with the magnetic equilibrium of JET pulse # 92398 at 7.5s.	48
4.4	The new JET CXRS system [86].	49
5.1	Schematic diagram of integration of modules in ASTRA.	54
5.2	European Transport Solver: a schema of the workflow [121].	55
5.3	Benchmarking of ETS impurity solver with SANCO code for conditions of JET tokamak assuming parabolic plasma profiles.	56
5.4	Schematic diagram of integration of codes in JINTRAC [127].	57
5.5	Scrape off layer in COREDIV code.	59
6.1	Electron temperature (top) and density (bottom) profiles from HRTS diagnostic and from COREDIV simulations as function of the normalized minor radius. From left to right: #80896,#80889 and #80893 at time $t = 19.5s$ [139].	62
6.2	(a) Experimental and COREDIV input Be fluxes, (b) experimental and simulated D fluxes, (c) experimental and simulated total radiated power, and (d) power radiated inside the separatrix for the three discharges considered, labeled according to their line average density [139].	63
6.3	(a) Experimental and simulated W concentration (C_W), (b) experimental and simulated Z_{EFF} , (c) experimental electron temperature measured at the outer strike point and simulated with COREDIV, and (d) experimental electron density measured at the outer strike point and simulated with COREDIV for the three discharges considered, labeled according to their line average density.	64
6.4	Calculated and experimental plasma profiles (left) for the JET ILW shot #87412 at $t = 10.3s$ [141]. Tomographic 2D reconstruction of the SXR radiated power density the JET ILW shot #87412 at $t = 10.3$ sec.(right).	65
7.1	Electron density (left), electron (right) temperature profiles from HRTS diagnostic at different time for shot #82291 (top) and shot #82295 (bottom).	68
7.2	Total(black), core(red) and SOL(green) radiations versus nitrogen gas puff level.	69
7.3	Simulated and experimental tungsten concentration versus nitrogen puff [140].	69
7.4	Simulated tungsten flux versus ion divertor temperature.	69
7.5	Experimental W density flux versus electron divertor temperature [140]. . .	69
7.6	Electron temperature (top) and density (bottom) profiles from HRTS diagnostic at different time and from COREDIV simulations, as function of the normalized minor radius for shots #82031(left), #83179(middle) and #83570(right).	71
7.7	Profile of the radiation at $t = 16s$ for shot #82031(left),at $t = 14s$ for shot #83179(middle) and at $t = 6.25s$ for shot #83570(right).	72

7.8	Experimental electron density (a) and electron temperature (b) profiles from HRTS diagnostic at different times and from COREDIV simulations, as function of the normalized minor radius for the JET shot #85441. For the same shot radiation profiles in the core from experiment and from simulations (c) [144].	73
7.9	Simulated radiation losses versus Z_{EFF} value for neon seeding together with experimental points for JET shots: #85438, #85439, #85441.	73
7.10	Experimental and COREDIV simulated (from top to bottom) total radiated power, ratio of radiated power in the divertor and the total one, electron temperature at the target plate as a function of the COREDIV Ne seeding rate.	74
7.11	Experimental and COREDIV simulated (from top to bottom) W concentration, power to the target plate and Z_{EFF} as a function of the COREDIV Ne seeding rate.	74
7.12	Comparison of W concentration obtained by using the SXR system and VUV spectrometer with the modeling one based on simulation with the COREDIV code for different plasma radii (especially in the plasma core and at mid-radius).	76
7.13	Comparison of Ni concentration obtained by using the VUV spectrometer with the modeling one based on simulation with the COREDIV code for the plasma region $r/a = 0.3-0.4$	77
7.14	Comparison of simulated Ni radiation for two discharges with different Ne seeding rates.	77
7.15	Time traces of main plasma parameters of discharge #87194.	79
7.16	Temperatures (left) and density (right) profiles by simulation and experiment for shot 87194 at the time $t = 14s$	79
7.17	Main plasma parameters versus impurity influx for different gasses (N, Ne, Ar and Kr): radiation fraction (f_{RAD}), power to the SOL (P_{SOL}) and to plate (P_{PLATE}), electron temperature at the plate (T_e^{PLATE}), SOL radiation (R^{SOL}) and effective charge Z_{EFF} [148].	80
7.18	Main plasma parameters for different impurity puff: N, Ne, Ar and Kr level: total (R^{CORE}), W (R_W^{CORE}) and by seeding impurity (R_{IMP}^{CORE}) radiation in the core, average ion temperature ($\langle T_i \rangle$), W (C_W) and impurity (C_{IMP}) concentration.	81
7.19	Transport coefficient C_E for different impurity puff: N, Ne, Ar and Kr level.	82
7.20	Radiation profiles: total, W and seeded impurity in the core. The dotted line shows the pedestal position.	83
8.1	JET shot #81856. Experimental time traces of auxiliary heating power, radiative losses and line-averaged effective charge.	85
8.2	Comparison of experimental profiles of electron density and temperature for ICRH (blue) and NBI (red) heating phases in discharge#81856 [121].	86

8.3	ETS input (left): total density of Ni in discharge #81856 obtained with the SPRED diagnostic (blue crosses) and assumed in ETS simulations (red stars). ETS output (right): benchmark of radiation (red stars) from Ni obtained with ETS to the one computed from experimental data using the UTC code (blue crosses).	86
8.4	Comparison of simulated steady state profiles of radiative power density with experimentally measured ones: black curves total profiles, red curves W contribution to the total; blue curves Ni contribution to the total; green curves Be contribution to the total.	87
8.5	Comparison of simulated steady state profiles of effective charge with experimentally measured ones: black curves total profiles, red curves W contribution to the total; blue curves Ni contribution to the total; green curves Be contribution to the total.	87
8.6	JET shot #81856. Simulated steady state profiles of radiative power density and Z_{EFF} : The reference case (blue curves) corresponds to the NBI phase (time t_2). The effects of ICRH (time t_1) are simulated by either increasing the Be and W source (red curves) or increasing the inward Be and W pinch (green curves). Dashed curves total Be contribution; dash-dot curves total W contribution to radiative loss.	88
8.7	Experimental time slices for shot # 92437.	90
8.8	Experimental time slices for shot # 92442.	90
8.9	The experimental data for W concentration based on soft X-ray for # 92437 (full symbol) and # 92442 (open symbol) for three different position at the normalized radius ($r/a = 0; 0.3; 0.45$).	91
8.10	Time evolution on the Ni concentration for # 92437 (open symbol) and # 92442 (full symbol) for position at the normalized radius ($r/a = 0.5 \div 0.6$).	91
8.11	Comparison of two discharges.	91
8.12	Tungsten emission in inner divertor.	91
8.13	COREDIV cooling rates for nickel(Ni) and tungsten(W) in corona equilibrium.	92
8.14	The electron density (top), temperature (bottom) profile from HRTS diagnostic at time $t = 13.9s$ for # 92437 with different auxiliary heating.	92
8.15	Profile of the core radiation at $t = 13.9s$	93
8.16	Tomographic reconstruction of the radiated power density for shot # 92347 at time $t = 13.9s$	93
8.17	Profile of the core radiation at $t = 14.26s$	94
8.18	Tomographic reconstruction of the radiated power density for shot #92347 at time $t = 14.25s$	94
8.19	Plasma parameters versus nitrogen puff level for plasma density $\langle n_e \rangle = 7 \times 10^{19} m^{-3}$ and auxiliary heating powers $P_{aux} = 13 \div 30 MW$: a) radiation fraction, b) core radiation, c) SOL radiation and d) ratio between SOL and core radiations	95
8.20	Temperature on the plate versus nitrogen puff level for plasma density $\langle n_e \rangle = 7 \times 10^{19} m^{-3}$ and auxiliary heating powers $P_{aux} = 13 \div 30 MW$	95

8.21	Plasma parameters versus neon concentration for $H_{98} = 1.2$: (a) radiation fraction (f_{RAD}), (b) power to the target plates, (c) core radiation, (d) SOL radiation, (e) Z_{EFF} , (f) transport multiplication factor.	96
8.22	Experimental and simulated electron density (left) and electron temperature profiles (central) and electron and ion temperature (right) for #92398 at time $t \sim 7.5$ s.	97
9.1	The normalized separatrix density, n_e^{sep}/n_{GW} , versus the normalized line average density, n_e^{av}/n_{GW}	99
9.2	Experimental (HRTS) and reconstructed T_e and n_e profiles at $t = 14.48$ s with difference density on the separatrix (n_e^{sep}).	101
9.3	Tomographic reconstruction of the radiated power density for shot #92347 at time $t = 14.25$ s.	102
9.4	Hybrid regime: plasma parameters versus nitrogen gas puff for three different electron density on the separatrix electron density is $n_e^{sep} = 3.0 \times 10^{19} \text{m}^{-3}$ (black line), $n_e^{sep} = 3.5 \times 10^{19} \text{m}^{-3}$ (red line) $n_e^{sep} = 3.75 \times 10^{19} \text{m}^{-3}$ (green line): total (circle symbols), core (square symbol) and SOL (triangle) radiation (a), electron temperature at the plate (b), radiation SOL/CORE (c), W and Be concentration (d), radial fraction (e), power to plate (f).	102
10.1	Plasma parameters for different radial diffusion coefficient in SOL (D_{perp}^{SOL}).	104
10.2	Plasma parameters versus nitrogen puff level for different edge densities, $n_e^{sep} = 3.06 \times 10^{19} \text{m}^{-3}$, $n_e^{sep} = 3.5 \times 10^{19} \text{m}^{-3}$ and different radial diffusion coefficients in the SOL, $D_{perp}^{SOL} = 0.5 \text{m}^2/\text{s}$, $D_{perp}^{SOL} = 1 \text{m}^2/\text{s}$ a) total radiation losses, b) core radiation, c) SOL radiation.	105
10.3	Experimental time traces of the four pulses examined. The seven time slices of the simulated shot points are shown.	106
10.4	Comparison experiment-simulation for the seven "shot points" here considered.	107
11.1	Plasma parameters versus plasma current: (a) Power to target plates, (b) f_{RAD} , (c) W concentration.	112
11.2	Radial profiles of electron temperature and plasma radiation for the highest plasma current ($I=4.5$ MA).	112
11.3	Radial profiles of electron temperature and plasma radiation for the highest plasma current ($I=4.5$ MA).	113

Bibliography

- [1] T. Putterich. Investigations on spectroscopic diagnostic of high-Z elements in fusion plasmas. *Technical Report IPP 10/29, Max-Planck Institut for Plasma Physics, Garching, Germany*, April 2006.
- [2] J. Wesson. *Tokamaks*, volume 1. Clarendon Press, Oxford, England, 2004.
- [3] R. Dux. Impurity transport in tokamak plasmas. *IPP report 10/27, Max-Planck Institut for Plasma Physics, Garching, Germany*, 2004.
- [4] T. Putterich and et.al. Determination of the tolerable impurity concentrations in a fusion reactor using a consistent set of cooling factors. *Nucl. Fusion*, 59:056013, 2019.
- [5] E. I. Moses. Ignition on the National Ignition Facility: a path towards inertial fusion energy. *Nucl. Fusion*, 49(10):104022, 2009.
- [6] R. Balescu. *Transport processes in plasmas - classical transport theory*, volume 1. Elsevier Science Technology, Amsterdam, 1988.
- [7] D. D. Ryutov and et al. The physics of fast Z pinches. *Rev. Mod. Phys.*, 72(1):167, 2000.
- [8] T. R. Jarboe. Review of spheromak research. *Plasma Phys. Control. Fusion*, 36:945, 1994.
- [9] P. Helander and et al. Stellarator and tokamak plasmas: a comparison. *Plasma Phys. Control. Fusion*, 54(12):124009, 2012.
- [10] <https://www.anthropoceneinstitute.com/science/generation/fusion/>.
- [11] F. Wagner. A quarter-century of H-mode studies. *Plasma Phys. Control. Fusion*, 49(12B):B1, 2007.
- [12] V. V. Parail. Energy and particle transport in plasmas with transport barriers. *Plasma Phys. Control. Fusion*, 44(5A):A63, 2002.
- [13] D.C. McDonald and et al. Recent progress on the development and analysis of the ITPA global H-mode confinement database. *Nucl. Fusion*, 47(3):147, 2007.
- [14] Y R Martin and et al. Power requirement for accessing the H-mode in ITER. *Journal of Physics: Conference Series*, 123(1):012033, 2008.

- [15] E. Righi and et al. Isotope scaling of the H mode power threshold on JET. *Nucl. Fusion*, 39(3):309, 1999.
- [16] J W Connor. Edge-localized modes - physics and theory. *Plasma Phys. Control. Fusion*, 40(5):531, 1998.
- [17] H. Zohm. The physics of edge localized modes (ELMs) and their role in power and particle exhaust. *Plasma Phys. Control. Fusion*, 38(8):1213, 1996.
- [18] M. Shimada and et al. Chapter 1: Overview and summary. *Nucl. Fusion*, 47(6):S1, 2007.
- [19] J. Linke and et al. Performance of different tungsten grades under transient thermal loads. *Nucl. Fusion*, 51(7):073017, 2011.
- [20] H. Zohm and et al. On the physics guidelines for a tokamak DEMO. *Nucl. Fusion*, 53(7):073019, 2013.
- [21] A. Kallenbach and et al. Partial detachment of high power discharges in ASDEX Upgrade. *Nucl. Fusion*, 55(5):053026, 2015.
- [22] A Kallenbach and et al. Impurity seeding for tokamak power exhaust: from present devices via ITER to DEMO. *Plasma Phys. Control. Fusion*, 55(12):124041, 2013.
- [23] W. Wischmeier. Impurity seeding for tokamak power exhaust: from present devices via ITER to DEMO. *J. Nucl. Mater.*, 463:22, 2015.
- [24] O. Kardaun and et al. Next step tokamak physics: confinement-oriented global database analysis. In IAEA, editor, *Proc. 18th Int. Conf. on Fusion Energy*, Sorrento, Italy, 4 - 10 October 2000.
- [25] M. Keilhacker and et al. High fusion performance from deuterium-tritium plasmas in JET. *Nucl. Fusion*, 39(2):209, 1999.
- [26] J. Roth and et al. Tritium inventory in ITER plasma-facing materials and tritium removal procedures. *Plasma Phys. Control. Fusion*, 50(10):103001, 2008.
- [27] T. Hirai and et al. R and D on full tungsten divertor and beryllium wall for JET ITER-like wall project. Fusion Engineering and Design. *Fusion Eng. Des.*, 53(8):1842, 2007.
- [28] S. Brezinsek and et al. Fuel retention studies with the ITER-Like Wall in JET. *Nucl. Fusion*, 53(8):083023, 2013.
- [29] J. C. Flanagan et al. Characterising dust in JET with the new ITER-like wall. *Plasma Phys. Control. Fusion*, 57:014037, 2015.
- [30] D. Naujoks. *Plasma-material interaction*. Springer, Berlin, Heidelberg, 2006.

- [31] W. Eckstein. *Computer Simulation of Ion-Solid Interaction*, volume 10. Springer-Verlag Berlin Heidelberg, 1991.
- [32] J. Bohdansky and J. Roth. An analytical formula and important parameters for low energy ion sputtering. *J. Appl. Phys.*, 51(5):2861, 1985.
- [33] W. Eckstein and et al. Sputtering data. Technical Report IPP 9/82, Max-Planck-Institut für Plasmaphysik, 1992.
- [34] Y. Yamamura and J. Bohdansky. New collisions approach for threshold sputtering. *Vacuum*, 35(12):561, 1985.
- [35] W. Eckstein. Calculated sputtering, reflection and range values. Technical Report IPP 9/132, Max-Planck-Institut für Plasmaphysik, 2002.
- [36] J. Roth. Sputtering of limiter and divertor materials. *J. Nucl. Mater.*, 176-177:132, 1990.
- [37] J.W. Davis and A.A. Haasz. Impurity release from low-Z materials under light particle bombardment. *J. Nucl. Mater.*, 241-243:37, 1997.
- [38] J. Roth. Chemical erosion of carbon based materials in fusion devices. *J. Nucl. Mater.*, 266-269:51, 1999.
- [39] W. Eckstein and et al. Particle induced erosion of Be, C and W in fusion plasmas. Part B: Physical sputtering and radiation-enhanced sublimation. *Atomic and Plasma-Material Interaction Data for Fusion*, 7(Part B):9, 2001.
- [40] J. Roth. Status of knowledge of chemical erosion of carbon and critical issues for extrapolation to ITER. *Phys. Scr.*, 2006(T124):37, 2006.
- [41] P.C. Stangeby. *The plasma boundary of magnetic fusion device*. Institute of Physics Pub., Bristol, Philadelphia, 2000.
- [42] A. Sestero. Formation and evolution of a wall protective plasma shield in a hard disruption. *Nucl. Fusion*, 35(8):919, 1995.
- [43] E.J. Doyle and et al. Modifications in turbulence and edge electric fields at the LH transition in the DIII-D tokamak. *Phys. Fluids B*, 3(8):2300, 1991.
- [44] P. Gohil and et al. Study of giant Edge-Localized Modes in DIII-D and comparison with ballooning theory. *Phys. Rev. Lett.*, 61:1603, 1988.
- [45] T. Ozeki and et al. Plasma shaping, edge ballooning stability and ELM behaviour in DIII-D. *Nucl. Fusion*, 30(8):1425, 1990.
- [46] H. Zohm and et al. ELM studies on DIII-D and a comparison with ASDEX results. *Nucl. Fusion*, 35(5):543, 1995.
- [47] T. Eich and et al. ELM divertor peak energy fluence scaling to ITER with data from JET, MAST and ASDEX upgrade. *Nucl. Mat. Energy*, 12:84, 2017.

- [48] J. Roth and et al. Recent analysis of key plasma wall interactions issues for ITER. *J. Nucl. Mater.*, page 1, 2006.
- [49] T. Eich and et al. Empirical scaling of inter-ELM power widths in ASDEX Upgrade and JET. *J. Nucl. Mater.*, 438:S72, 2013.
- [50] G. Federici and et al. Plasmatomaterial interactions in current tokamaks and their implications for next step fusion reactors. *Nucl. Fusion*, 41(12R):2001, 2006.
- [51] D. Naujoks and et al. Tungsten as target material in fusion devices. *Nucl. Fusion*, 36(6):671, 1996.
- [52] G. Fussmann and et al. High-Z elements as target materials in fusion devices. In IAEA, editor, *Proc.15th Conf. on Plasma Physics and Controlled Nuclear Fusion Research*, volume 2, page 143, Seville, Sapain, 26 September - 1 October 1994.
- [53] R. Dux and et al. Main chamber sources and edge transport of tungsten in H-mode plasmas at ASDEX Upgrade. *Nucl. Fusion*, 51(5):053002, 2011.
- [54] R.Zagórski and et al. Main chamber sources and edge transport of tungsten in H-mode plasmas at ASDEX Upgrade. *Fusion Eng. Des.*, 109-111:37, 2016.
- [55] D. Tskhakaya. Modelling of tungsten re-deposition coefficient. *J. Nucl. Mat.*, 463:624, 2015.
- [56] A. V. Chankin, D. P. Coster, and R. Dux. Monte Carlo simulations of tungsten redeposition at the divertor target. *Plasma Phys. Control. Fusion*, 56(2):025003, 2014.
- [57] E.A. Lazarus and et al. Confinement in beam-heated plasmas: the effects of low-Z impurities. *Nucl. Fusion*, 25(2):135, 1985.
- [58] K. McCormick and et al. Edge density measurements with a fast Li beam probe in tokamak and stellarator experiments. *Fusion Eng. Des.*, 33-35:125, 1997.
- [59] D. Pasini and et al. Impurity transport in JET using laser injected impurities in Ohmic and radiofrequency heated plasmas. *Nucl. Fusion*, 30(10):2049, 1990.
- [60] S. Jachmich and et al. Power and particle fluxes to plasma-facing components in mitigated-ELM H-mode discharges on JET. *J. Nucl. Mater.*, 415(1, Supplement):S894 – S900, 2011. Proceedings of the 19th International Conference on Plasma-Surface Interactions in Controlled Fusion.
- [61] H.-K. Chung. Atomic processes Modeling in plasmas. Modeling Spectroscopy observables from plasmas. In ICTP, editor, *Joint ICTP-IAEA Workshop on Fusion Plasma Modelling using Atomic and Molecular Data*, Trieste, Italy, 23-27 January 2000.
- [62] P. G. Carolon and V. A. Piotrowicz. The behaviour of impurities out of coronal equilibrium. *Plasma Physics*, 25(10):1065, 1983.

- [63] S.I.Braginskii. *Reviews in Plasma Physics*, volume 1. New York: Consultants Bureau, 1965.
- [64] R. Zagorski and et al. Simulations with the COREDIV code of DEMO discharges. *Nucl. Fusion*, 53:073030, 2013.
- [65] Yu.L. Igitkhanov and et al. Description of an arbitrary level impurities in the scrape-off tokamak plasma. In *Proc.14th EPS Conference*, volume 2, page 3933, Mafrid, Spain, 26 September - 1 October 1988.
- [66] R. Zagórski. Numerical modelling of the edge plasma in tokamaks. *J. Techn. Phys.*, 37(1):7, 1996.
- [67] Y. Yamamura and et al. Angular Dependence of Sputtering Yields of Monoatomic solids. Technical Report Rep. IPPJ-Am 26, Inst. of Plasma Physics, Nagoya Univ., 1983.
- [68] S.P.Hirshman and D.J. Sigmar. Review paper: neoclassical transport on impurities in tokamak plasmas. *Nucl. Fusion*, 21(9):1079, 1981.
- [69] D.J. Sigmar K.W. Wenzel. Neoclassical analysis of impurity transport following transition to improved particle confinement. *Nucl. Fusion*, 30(6):1117, 1990.
- [70] ITER Physics Expert Group. Chapter 2: Plasma confinement and transport. *Nucl. Fusion*, 39(12):2175, 1999.
- [71] X. Garbet and et al. Physics of transport in tokamaks. *Plasma Phys. Control. Fusion*, 46:B557, 2004.
- [72] H.Nordman and et al. Simulation of toroidal drift mode turbulence driven by temperature gradients and electron trapping. *Nucl. Fusion*, 30:983, 1990.
- [73] R.E. Waltz and et al. A gyro-Landau-fluid transport model. *Phys. Plasmas*, 4:2482, 1997.
- [74] R.E. Waltz and R. L. Miller. Ion temperature gradient turbulence simulations and plasma flux surface shape. *Physics of Plasmas*, 6(11):4265, 1999.
- [75] G.M.Staebler and J. E. Kinsey. Electron collisions in the trapped gyro-Landau fluid transport model. *Plasma Phys. Control. Fusion*, 35(7):843, 1995.
- [76] I. Voitsekhovitch and et al. Modelling of JET hybrid scenarios with GLF23 transport model: E x B shear stabilization of anomalous transport. *Nucl. Fusion*, 54:093006, 2014.
- [77] J.Citrin and et al. Predictive analysis of q-profile influence on transport in JET and ASDEX Upgrade hybrid scenarios. *Plasma Phys. Control. Fusion*, 54:065008, 2012.

- [78] E. A. Belli and J. Candy. Kinetic calculation of neoclassical transport including self-consistent electron and impurity dynamics. *Plasma Phys. Control. Fusion*, 50:095010, 2008.
- [79] J. Mandrekas and W. M. Stacey. An impurity seeded radiative mantle for ITER. *Nucl. Fusion*, 50:095010, 2008.
- [80] H. Maister and et al. Zeff from spectroscopic bremsstrahlung measurements at ASDEX Upgrade and JET. *Rev. Sci. Instrum.*, 75(10):4097, 2004.
- [81] P. D. Morgan and et al. Spectroscopic measurements on the Joint European Torus using optical fibers to relay visible radiation. *Rev. Sci. Instrum.*, 56(5):862, 1985.
- [82] H. Weisen and et al. Measurement of light impurity densities and Zeff in JET using x-ray tomography. *Rev. Sci. Instrum.*, 62(6):1531, 1991.
- [83] R.J.Fonck and et al. Multichannel grazing-incidence spectrometer for plasma impurity diagnosis: Spred. *Applied Optics*, 21(12):2115, 1982.
- [84] A. Czarnecka and et al. Analysis of metallic impurity content by means of VUV and SXR diagnostics in hybrid discharges with hot-spots on the JET-ITER like wall poloidal limiter. *Plasma Phys. Control. Fusion*, 61:085004, 2019.
- [85] C. Giroud and et al. Impact of calibration technique on measurement accuracy for the JET core charge-exchange systema. *Rev. Sci. Instrum.*, 79:10F625, 2008.
- [86] D.L.Hillis and et al. Enhanced core charge exchange recombination spectroscopy-system on Joint European Torus. *Rev. Sci. Instrum.*, 77:10F102, 2006.
- [87] D.L.Hillis and et al. A high throughput spectrometer system for helium ash detection on JET. *Rev. Sci. Instrum.*, 75(10):3449, 2004.
- [88] A. Czarnecka and et al. Determination of metal impurity density, ΔZ_{eff} and dilution on JET by VUV emission spectroscopy. *Plasma Phys. Control. Fusion*, 53:035009, 2011.
- [89] J.L. Schwob and et al. High-resolution duo-multichannel soft x-ray spectrometer for tokamak plasma diagnostics. *Rev. Sci. Instrum.*, 58:1601, 1987.
- [90] T. Pütterich and et al. Tungsten Screening and Impurity Control in JET. In *Proc.24th IAEA Fusion Energy Conference (FEC2012)*, San Diego, USA, 8 - 13 October 2012.
- [91] Simonini and et al. Models and Numerics in the Multi-Fluid 2-D Edge Plasma Code EDGE2D/U. *Contrib. Plasma Phys.*, 34:364, 1994.
- [92] D. Reiter. Progress in two-dimensional plasma edge modelling. *J. Nucl. Mat.*, 196-198:80, 1992.

- [93] M. Groth and et al. Impact of carbon and tungsten as divertor materials on the scrape-off layer conditions in JET. *Nucl. Fusion*, 53:093016 (11pp), 2013.
- [94] C. Guillemaut and et al. Influence of atomic physics on EDGE2D-EIRENE simulations of JET divertor detachment with carbon and beryllium/tungsten plasma-facing components. *Nucl. Fusion*, 54:093012 (25pp), 2014.
- [95] M. Groth and et al. Divertor plasma conditions and neutral dynamics in horizontal and vertical divertor configurations in JET-ILW low confinement mode plasmas. *J. Nucl. Mat.*, 463:471, 2015.
- [96] A.E. Jaervinen and et al. Interpretation of radiative divertor studies with impurity seeding in type-I ELMy H-mode plasmas in JET-ILW using EDGE2D-EIRENE. *J. Nucl. Mater.*, 463:135, 2015.
- [97] A.E. Jaervinen and et al. Comparison of H-mode plasmas in JET ILW and JET-C with and without nitrogen seeding. *Nucl. Fusion*, 56:093012 (25pp), 2016.
- [98] B. Viola and et al. EDGE2D-EIRENE simulations of the impact of poloidal flux expansion on the radiative divertor performance in JET. *Nuclear Materials and Energy*, 12:786, 2017.
- [99] A. V. Chankin and et al. EDGE2D-EIRENE modelling of near SOL Er: possible impact on the H-mode power threshold. *Plasma Phys. Control. Fusion*, 59:045012 (9pp), 2019.
- [100] H. Bufferand and et al. Near wall plasma simulation using penalization technique with the transport code SOLEDGE2D-EIRENE. *J. Nucl. Mat.*, 438:S445, 2013.
- [101] P. Tamain and et al. Investigation of the influence of divertor recycling on global plasma confinement in JET ITER-like wall. *J. Nucl. Mat.*, 463:450, 2015.
- [102] R. Schneider and et al. Plasma Edge Physics with B2-Eirene. *Contrib. Plasma Phys.*, 46(1-2):3, 2006.
- [103] L. Aho-Mantila and et al. L-mode radiative plasma edge studies for model validation in ASDEX Upgrade and JET. *J. Nucl. Mat.*, 438:S321, 2013.
- [104] L. Aho-Mantila and et al. Model-based radiation scalings for the ITER-like divertors of JET and ASDEX Upgrade. *J. Nucl. Mat.*, 463:546, 2015.
- [105] G. Cenacchi and A. Taroni. JETTO: A free-boundary plasma transport code (basic version. *JET Report JET-IR(88)03 JET Joint Undertaking*, 1988.
- [106] M. Erba and et al. Development of a non-local model for tokamak heat transport in L-mode, H-mode and transient regimes. *Plasma Phys. Control. Fusion*, 39:261, 1997.
- [107] W. A. Houlberg and et al. Bootstrap current and neoclassical transport in tokamaks of arbitrary collisionality and aspect ratio. *Phys. Plasmas*, 4:3230, 1997.

- [108] S.Tamor. ANTIC: A code for calculation of neutral transport in cylindrical plasmas. *J. Comp. Phys.*, 40(1):104, 1981.
- [109] L. Lauro Taroniad et al. Impurity transport of high performance discharges in JET. In *21st EPS Conf. on Controlled Fusion and Plasma Physics*, volume 1, page 102, Montpellier, France, 27 June-1 July 1994.
- [110] H.P. Summers and et al. Atomic data for modelling fusion and astrophysical plasmas. *Plasma Phys. Control. Fusion*, 44(B):323, 2002.
- [111] C. Angioni and et al. Tungsten transport in JET H-mode plasmas in hybrid scenario, experimental observations and modelling. *Nucl. Fusion*, 54:083028 (26pp), 2014.
- [112] G. Pereverzev and P.N. Yushmanov. ASTRA Automated System for TRansport Analysis in a tokamak. Technical Report IPP 5/98, Max-Planck-Institut für Plasmaphysik, 2002.
- [113] O. Sauter and et al. Neoclassical conductivity and bootstrap current formulas for general axisymmetric equilibria and arbitrary collisionality regime. *Phys. Plasmas*, 6:2834, 1999.
- [114] E. Fable and et al. Novel free-boundary equilibrium and transport solver with theory-based models and its validation against ASDEX Upgrade current ramp scenarios. *Plasma Phys. Control. Fusion*, 55:124028 (9pp), 2013.
- [115] S. Glögler and et al. Study of the impact of high neon radiation on pedestal and divertor in JET experiments. In European Physical Society, editor, *Proc. 45th EPS Conference on Plasma Physics*, Prague, 2 - 6 July 2018.
- [116] S. Glögler and et al. Characterisation of highly radiating neon seeded plasmas in JET-ILW. *Nucl. Fusion*, 59:126032(18pp), 2019.
- [117] R. J. Hawryluk. An empirical approach to tokamak transport. *Physics of Plasmas Close to Thermonuclear Conditions*, 1:19, 1980.
- [118] H.-T. Kim et al. Comparative analysis of core heat transport of JET high density H-mode plasmas in carbon wall and ITER-like wall. *Plasma Phys. Control. Fusion*, 57:065002, 2013.
- [119] D. Kalupin et al. Construction of the European Transport Solver under the European Integrated Tokamak modelling task force. In *Proc. 35th EPS Conf. Plasma Phys.*, page 1883, Crete, Greece, 9-13 June 2008 2008.
- [120] I. Imbeaux and et al. A generic data structure for integrated modelling of tokamak physics and subsystems. *Comput. Phys. Commun.*, 181(6):987, 2010.
- [121] D. Kalupin et al. Numerical analysis of JET discharges with the European Transport Simulator. *Nucl. Fusion*, 53:123007 (8pp), 2013.

- [122] JET TEAM presented by A. Taroni. Energy and particle transport modelling with a time dependent combined core and edge transport code. In *Proc.16th IAEA Fusion Energy Conference*, volume 2, page 493, Montreal, CANADA, 7 - 11 October 1996.
- [123] G.T.A. Huysmans and et al. Izoparametric bicubic Hermite elements for solution of the Grad Shafranov equation. *Int. J. Mod. Phys. C*, 2(1):371, 1991.
- [124] A.B. Mikhailovskii and et al. Optimization of computational MHD normal-mode analysis for tokamaks. *Plasma Physics Reports*, 23(10):844, 1997.
- [125] F. Romanelli and et al. JINTRAC: A System of codes for integrated simulation of tokamak scenarios. *Plasma and Fusion Research*, 9:3403023, 2014.
- [126] S. Wiesen and et al. Integrated modelling of a JET type-I ELMy H-mode pulse and predictions for ITER-like wall scenarios. *Plasma Phys. Control. Fusion*, 53:124039 (12pp), 2011.
- [127] S. Wiesen and et al. Effect of PFC recycling conditions on JET pedestal density. *Contrib. Plasma Phys.*, 56(6-8):754, 2015.
- [128] F. Koelchl and et al. W transport and accumulation control in the termination phase of JET H-mode discharges and implications for ITER. *Plasma Phys. Control. Fusion*, 60:074008 (21pp), 2018.
- [129] M. Oberkofler and et al. First nitrogen-seeding experiments in JET with the ITER-like Wall. *J. Nucl. Mater.*, 438:S258, 2013.
- [130] R. Zagorski and R. Stankiewicz. Effect of core-edge coupling on operation regimes of ITER-like reactor. *J. Nucl. Mater.*, 313-316:899, 2003.
- [131] R. Stankiewicz and R. Zagorski. Influence of coreedge coupling and impurities on the operation regimes of a fusion reactor. *J. Nucl. Mater.*, 337-339:191, 2005.
- [132] M.Leigheb and et al. SOL parameters and local transport in the FTU tokamak. *J. Nucl. Mater.*, 241-243:914, 1997.
- [133] H. Gerhauser and et al. Numerical modelling of pump limiter biasing on TEXTOR-94 and Tore Supra. *Nucl. Fusion*, 42:805, 2002.
- [134] R. Zagorski and H. Gerhauser. Numerical modelling of Marfe phenomena in TEXTOR tokamak. *Physica Scripta*, 70:173, 2004.
- [135] V. Pericoli-Ridolfini and et al. Edge properties with the liquid lithium limiter in FTUexperiment and transport modelling. *Plasma Phys. Control. Fusion*, 49:S123, 2007.
- [136] R. Zagorski and et al. Numerical investigations of edge plasma flows in the Tore Supra tokamak. *Plasma Phys. Control. Fusion*, 49:S97, 2007.

- [137] R. Zagorski and et al. Self-consistent modeling of impurity seeded JET advanced tokamak scenarios. *J. Nucl. Mater.*, 390-391:404, 2009.
- [138] Yu. F. Baranov and et al. Interplay between confinement, impurities and MHD in JET Hybrid pulses with ITER like wall. In *Proc.40th EPS conference on Plasma Physics*, page pp.P5.142, Espoo, Finland, 1 - 5 July 2013.
- [139] G. Telesca and et al. Simulation with the corediv code of jet discharges with the iter-like wall. *J. Nucl. Mater.*, 438:S567, 2013.
- [140] G.J. van Rooij and et al. Tungsten divertor erosion in all metal devices: Lessons from the ITER like wall of JET. *J. Nucl. Mater.*, 438:S42, 2013.
- [141] R. Zagorski and et al. Modelling of JET DT experiments in ILW configurations like wall of JET. *Contrib. Plasma Phys.*, 56(6-8):766, 2016.
- [142] I. Ivanova-Stanik and et al. COREDIV and SOLPS numerical simulations of the nitrogen seeded JET ILW L-mode discharges. *Contrib. Plasma Phys*, 56(6-8):760, 2016.
- [143] I. Ivanova-Stanik and et.al. Integrated Modelling of Nitrogen Seeded JET ILW Discharges for H-mode and Hybrid Scenarios. *Contrib. Plasma Phys.*, 54(4-6):442, 2014.
- [144] R. Zagorski and et al. Influence of seeding and SOL transport on plasma parameters in JET ITER-like wall H-mode discharges. *J. Nucl. Mater.*, 463:649, 2015.
- [145] G. Telesca and et al. Core-SOL Modelling of Neon Seeded JET Discharges with the ITER-like Wall. *Contrib. Plasma Phys*, 56(6-8):748, 2016.
- [146] N. Krawczyk. Application of the vuv and the soft x-ray systems on jet for the study of intrinsic impurity behavior in neon seeded hybrid discharges. *Rev. Sci. Instrum.*, 89:10D131, 2018.
- [147] M. Wischmeier. High density operation for reactor-relevant power exhaust. *J. Nuc. Mater.*, 463:404, 2015.
- [148] I. Ivanova-Stanik and R. Zagorski. COREDIV modeling of JET ILW discharges with different impurity seeding: nitrogen, neon, argon and krypton. *Nukleonika*, 62(2):3, 2017.
- [149] C. Giroud et al. Towards baseline operation integrating ITER-relevant core and edge plasma within the constraint of the ITER-like wall at JET. In *Proc. 25th IAEA Fusion Energy Conference*, St Petersburg, Russian Federation, 13th - 18nd October 2014.
- [150] A. Huber et al. Impact of strong impurity seeding on the radiation losses in JET with ITER-like Wall. In *Proc. 41th EPS Conference*, page P1.031, Berlin, Germany, 23 - 27 June 2014.

- [151] P. Jacquet and et.al. ICRF heating in JET during initial operations with the ITER-like wall. *AIP Conference Proceedings*, 1580:65, 2014.
- [152] D.E. Post and et al. Steady-state radiative cooling rates for low-density, high-temperature plasmas. *Atomic Data and Nuclear Data Tables*, 20(5):397, 1997.
- [153] P.C. de Vries and et.al. Survey of disruption causes at JET. *Nucl. fusion*, 51:053018 (12pp), 2011.
- [154] J. P. S. Bizarro and et.al. Modelling the Ohmic L-mode ramp-down phase of JET hybrid pulses using JETTO with Bohmgyro-Bohm transport. *Plasma Phys. Control. Fusion*, 58:105010 (19pp), 2016.
- [155] E. Joffrin et al. Disruption study advances in the JET metallic wall. In *Proc. 26th IAEA Fusion Energy Conference*, Kyoto, Japan, 17th - 22nd October 2016.
- [156] G.M.D. Hogeweyj and et.al. Impact of W on scenario simulations for ITER. *Nucl. Fusion*, 55:063031 (11pp, 2015).
- [157] F. Koechl and et.al. Modelling of transitions between L- and H-mode in JET high plasma current plasmas and application to ITER scenarios including tungsten behaviour. *Nucl. Fusion*, 57:086023 (32pp), 2017.
- [158] R. Neu and et.al. First operation with the JET International Thermonuclear Experimental Reactor-like wall . *Phys. Plasmas*, 20:056111, 2013.
- [159] R. Dux and et.al. The interplay of controlling the power exhaust and the tungsten content in ITER. *Phys. Plasmas*, 12:28, 2017.
- [160] E. de la Luna et al. Impact of ELM control in JET experiments on H-mode terminations with/without current ramp-down and implications for ITER. In *Proc. 27th IAEA Fusion Energy Conference*, Ahmedabad, India, 22-27 October 2018.
- [161] R. Zagórski et al. Modelling of JET DT experiments in ILW configurations. *Contrib. Plasma Phys.*, 58:739, 2018.
- [162] A. Kallenbach and et.al. Parameter dependences of the separatrix density in nitrogen seeded ASDEX Upgrade H-mode discharges. *Plasma Phys. Control. Fusion*, 60:045006 (8pp), 2018.
- [163] S.J. Davies and et.al. Behaviour of upstream separatrix density in JET H-mode plasmas. *J. Nucl. Mater.*, 266-269:1028, 1999.
- [164] R.J. Goldston and et.al. A new scaling for divertor detachment. *Plasma Phys. Control. Fusion*, 59:055015 (7pp), 2017.
- [165] T. Eich and et.al. Correlation of the tokamak H-mode density limit with ballooning stability at the separatrix. *Nucl. Fusion*, 58:034001 (5pp), 2018.

- [166] A. Huber and et.al. Density limit of H-mode plasmas on JET-ILW. *J. Nucl. Mater.*, 463:445, 2015.
- [167] B. LaBombard and et.al. Cross-field plasma transport and main-chamber recycling in diverted plasmas on Alcator C-Mod. *Nucl. Fusion*, 40:2041, 2000.
- [168] N. Den Harder and et.al. ELM-resolved divertor erosion in the JET ITER-Like Wall. *Nucl. Fusion*, 56:026014 (9pp), 2016.
- [169] G. Telesca and et.al. High power neon seeded JET discharges: experiments and simulations. *Nuclear Materials and Energy*, 12:882, 2017.
- [170] JET Team. Fusion energy production from a deuterium-tritium plasma in the JET tokamak. *Nucl. Fusion*, 32(2):187, 1992.
- [171] M. Keilhacker and et.al. High fusion performance from deuterium-tritium plasmas in JET. *Nucl. Fusion*, 39(2):209, 1999.
- [172] J.Pamela and et.al. The JET programme in support of ITER. *Fusion Eng. and Design*, 82:590, 2007.
- [173] E. Joffrin and et.al. Overview of the JET preparation for deuteriumtritium operation with the ITER like-wall. *Nucl. Fusion*, 59:112021 (25pp), 2019.
- [174] M.N.A. Beurskens and et.al. The effect of a metal wall on confinement in JET and ASDEX Upgrade. *Plasma Phys. Control. Fusion*, 55:124043 (13pp), 2013.
- [175] S.A. Silburn and et.al. Mitigation of divertor heat loads by strike point sweeping in high power JET discharges. *Phys. Scr.*, T170:014040 (9pp), 2017.
- [176] C.D.Challis et al. Impact of neon seeding on fusion performance in JET ILW hybrid plasmas. In *Proc. 44th EPS Conference on Plasma Physics*, Belfast, Ireland, 26 - 30 June 2017.
- [177] X. Litaudon and et.al. Overview of the JET results in support to ITER. *Phys. Scr.*, 57(10):102001 (41pp), 2017.
- [178] M. Wischmeier. The physics basis for a solution to the power and particle exhaust problem of a next step device. In *Proc. 27th IAEA Fusion Energy Conference*, Ahmedabad, India, 22 - 27 October 2018.